Microstructural and geochemical study of Praid salt rocks (Transylvanian Basin)

M.Sc. Thesis

by

Orsolya GELENCSÉR

M.Sc. student of Geology

Mineralogy, petrology, geochemistry, mineral resources and archaeometry specialization

Supervisors:

Csaba SZABÓ Ph.D.

Lithosphere Fluid Research Lab

Department of Petrology and Geochemistry

György FALUS Ph.D.

Geology and Geoinformatics Division, Mining and Geological Survey of Hungary

Consultant:

Márta BERKESI Ph.D.

Lithosphere Fluid Research Lab

Department of Petrology and Geochemistry

LITHOSPHERE FLUID RESEARCH LAB
DEPARTMENT OF PETROLOGY AND GEOCHEMISTRY
INSTITUTE OF GEOGRAPHY AND EARTH SCIENCES
FACULTY OF SCIENCE
EÖTVÖS LORÁND UNIVERSITY

Budapest
2020

Table of Contents

List of Figures *4*

List of Tables *7*

1. Introduction *8*

2. Geologic background *11*

2.1. Evolution of the Transylvanian Basin **11**

2.2. The Badenian Salinity Crisis in the Transylvanian Basin **14**

3. Samples and analytical methods *17*

3.1. Sampling and sample preparation **17**

3.2. Petrography with polarized light microscopy **23**

3.3. Microthermometry **23**

3.4. Raman microspectrometry **24**

3.5. Stable isotope studies **25**

3.6. Electron Backscatter Diffraction **28**

3.7. Gamma-irradiation **28**

4. Results *30*

4.1. Results of petrography **30**

4.1.1. Fluid inclusion petrography 35

4.2. Results of microthermometry **39**

4.3. Results of Raman spectroscopy **40**

4.3.1 Identification of solid phases 40

4.3.2. Vapor-bearing fluid inclusions 42

4.3.3. Raman spectroscopy coupled with microthermometry 44

4.4. Stable isotope studies **47**

4.4.1. S and O stable isotopes in anhydrite 47

4.4.2. C and O stable isotopes in dolomite 48

4.4.3. O and H stable isotopes in primary (P-type) fluid inclusions 48

4.5. Results of electron backscatter diffraction (EBSD) mapping 50

4.6. Gamma irradiated measurements....52

5. Discussion.... 54

5.1. Petrographic evidences for primary features 54

5.1.1. Genetic interpretation of macroscopic- and microscopic features of the salt rocks 54

5.1.2. Primary fluid inclusions 55

5.2. Indications of primary features by Raman spectroscopy 57

5.2.1. Cryogenic measurements of primary fluid inclusions 57

5.2.2. Bioactivity in the paleo environment 59

5.2.3. The role of secondary fluid inclusions 60

5.3. Evidences of salt tectonics 62

5.3.1. Generalities in salt tectonics 62

5.3.2. Deformation mechanisms inferred micropetrographic study of the Praid samples 64

5.3.3. Differential stress and strain rate estimation 67

5.3.4. Interpretation of secondary displacements 69

5.4. Stable isotopic characteristic of minerals and fluid inclusions 72

5.4.1. Isotopic characteristic of sulfates 72

5.4.2. Isotopic characteristic of carbonates 75

5.4.3. Isotope geochemistry of fluid inclusions in halite 77

5.5. Addition to the Badenian Salinity Crisis 83

6. Conclusions.... 85

7. Summary.... 86

8. Abstract (in Hungarian) 88

9. Acknowledgement.... 90

10. Bibliography 92

List of Figures

Figure 1. Topographical map completed with Middle Miocene evaporite occurrences of the Carpathian-Pannonian region. The study area (Praid) is located at the Eastern part of the Transylvanian Basin. 1: gypsum 2: halite accompanied with anhydrite/gypsum (map redrawn after Popov et al. (2004); Peryt (2006); Horváth et al. (2006); Báldi et al. (2017)) . 11
Figure 2. Geologic map of the study area. Pyroclastic rock and Pannonian sediments dominated the area. Badenian evaporites exposed at Sovata and Praid suiting in the line of Eastern Diapir Alignment with NW-SE direction. Map scale: 1:200 000. Modified after Dumitrescu et al. (1970) 13
Figure 3. Seismic interpretation of a W-E section of the Transylvanian Basin. Black body represents the highly plastic salt layer. The Middle Miocene evaporite forms diapir alignments along the basin margin (Profile modified after Krézsek and Bally (2006). 14
Figure 4. Simplified paleogeographic reconstruction of Mediterranean-Paratethys connection during Badenian Salinity Crisis interval (both modified after (de Leeuw et al., 2018). Red closed circle marks the location of studied area. 15
Figure 5. A schematic profile through the Praid salt dome. The salt (blue color) brakes through the younger rocks (Buglovian is a locally used substage referring to late Badenian). A thin (couple of meters) young regolith layer covers and prevents the salt dome from dissolution and erosion. The mine is situated in the upper 400 m of the salt body. B: Layered type salt in the Praid Salt Mine (Visitor Level) showing folded structure. C: Massive type of salt from the Telegdy mine. Photo courtesy on behalf of the Praid Salt Mine for picture A. 20
Figure 6. Characteristic samples from Praid Salt Mine. A: massive type salt rock sample (PAT19-5) B: layered type salt rock sample (PA40-PH). 21
Figure 7. Map of the applied analytical methods. 22
Figure 8. Ongoing preparation process in the ICER Laboratory Institute for Nuclear Research, Debrecen. A: Copper tube, containing halite grains is connected to the vacuum system. In the pre-heating part of the procedure the glass capillary vial cannot trap any molecules. B: Glass vial in liquid nitrogen is serving as a trap. The liberated water from fluid inclusions freezes on the wall of the vial. 26
Figure 9. Representative photomicrographs on the two salt rock types and the drawn grain boundaries visualized by image editor software. A: Elongated halite crystals are placed in a submillimeter sized crystal mash in massive type salt. Large halite grains have fluid inclusion rich cores (red circle). Sample: PAT17-4, transmitted light, 1N. B: Grainsize distribution is more consistent in layered type salt rock, compared to the massive. ~ 120° joints are common indicating mosaic structure. Lack of primary fluid inclusions is characteristic for this type of salt rock. Sample: PAE17-3, transmitted light, 1N. 31
Figure 10. Surface of the irradiated salt rock sample. A: Subgrain-rich grain is consumed by subgrain free grain as indicated by white arrows. Subgrain structure is outlined. Sample: PA40-PH, reflected light. B: Subgrain-rich grain (on the left) in contact with three subgrain-free grains. The network of subgrains is partially outlined. Sample: PAT17-3, reflected light. 32
Figure 11. Accessories of the Praid salt rock from both types. A: Typical appearance of anhydrite and gypsum in halite. Gypsum occurs as needle shaped crystals. Sample: PAT17-3, transmitted light 1N. B: Part of A. Note, along anhydrite grain boundaries, abundant organic matter and capillaries filled by fluids can be observed. C: Rhombohedral dolomite, having dark, organic rich core. Cleavage planes could be also seen. Sample: PAT17-3, transmitted light, 1N. D: Idiomorphic quartz containing silicate melt inclusions. Sample: PA40-PH, transmitted light, 1N. E: Clay minerals as filled materials along grain boundaries of halite. Sample: PAT17-4, transmitted light, 1N. F: Metamorphic rock fragment containing quartz and garnet. Euhedral dolomite (such as C, precipitated to the edge of the

aggregate. Sample: PAE17-5, transmitted light, +N. Abbreviations: Anh: Anhydrite, Gp: Gypsum, Dol: Dolomite, OM: Organic matter, MI: Melt inclusion, Q: Quartz, GR: Garnet. 34

Figure 12. Photomicrographs are showing the primary fluid inclusion petrographic characteristics of the Praid salt rocks. A: Primary fluid inclusions in halite showing negative crystal shape and (only) liquid phase at room temperature. Sample: PAT17-4, transmitted light, 1N. B: Part of A. C: P2-type fluid inclusions in halite having irregular shape. Additionally, they contain dark, organic matter Sample: PAT17-2, transmitted light, 1N D: P2-type fluid inclusions containing organic material resulting irregular size and shape. Sample: PAT17-4 , transmitted light, 1N. L: liquid phase, OM: organic material. 36

Figure 13. Photomicrographs are showing the S-type fluid inclusion petrographic characteristics of the Praid salt rocks. A: Fluid inclusion captured tabular anhydrite crystal (S) at a primary FIA. Sample: PAT17-4, transmitted light, 1N. B: Gaseous dark secondary fluid inclusion array in the vicinity of a primary FIA. Sample: PAT17-4, transmitted light, 1N. C: Fluid film at a grain boundary. Sample: PAT17-2, transmitted light, 1N. D: Amoebae-like secondary fluid inclusions forming a net. Sample: PAE17-3, transmitted light, 1N. E: S1 type irregular shaped, two-phase fluid inclusions. Sample: PAT17-2, transmitted light, 1N F: Rounded cubic shaped, gas bearing fluid inclusion trail in halite. Sample: PAT17-1, transmitted light, 1N. Abbreviations: FI: fluid inclusion, S: solid, OM: organic matter, L: liquid V: vapor phases. 38

Figure 14. Histogram of the homogenization temperature values on the measured primary fluid inclusions from Praid. X and Y axis represent the temperature (°C) and frequency of homogenizations Th (L+V) →L, (°C), respectively. 40

Figure 15. Characteristic Raman spectra of common accessory minerals of Praid salt rocks. 41

Figure 16. On the left characteristic Raman spectra of β-carotene can be seen. On the right, a mineral aggregate can be seen. Orange color carotene is attached to the aggregate. Photo was taken under stereomicroscope (Sample: PAE17-3). 42

Figure 17. Representative Raman spectra of phases within studied secondary vapor phase fluid inclusion (photomicrograph at the right top) at room temperature. The peak of N_2 at 2329 cm^{-1} having of atmospheric origin, in contrast to the peak at 2330 cm^{-1}. Abbreviations: FI: fluid inclusion V: vapor phase fluid inclusion. 43

Figure 18. Measured $\delta^{18}O$ and $\delta^{2}H$ values from fluid inclusion plotted with Global Meteoric Waterline (black). The equation of the line is: y=1.18*x-68.561 50

Figure 19. Electron backscattered diffraction mapping of massive-type salt rock from Praid. The corresponding inverse pole Figures (IPFs) inferred from the EBSD maps (each map has its IPF below). Different colors indicate different crystallographic orientation. Shades of the colors indicate internal misorientation in the grain itself. Small colorful patches (e.g. in PAT17-4_021) are cracks on the surface, which were indexed incorrectly. 51

Figure 20. Results of microthermometry of Badenian Salinity Crisis halite primary fluid inclusions. Temperatures for comparison are from E-Slovakian Basin (Galamay et al., 2004), western diapir alignment of TB (Pintea, 2008) and from Praid (Kátai, 2017). The T_h is matching well, while the T_e shows difference between the two diapir alignments of the Transylvanian Basin in chemical composition of the FI. The other microtherometry study on Praid salt rocks (Kátai, 2017) is in a good agreement with this study. Abbreviations: T_h: homogenization temperature, T_e: eutectic temperature, T_m^{ice}: last melting temperature..... 56

Figure 21. Characteristic Raman spectra of primary-type fluid inclusions on -190 °C after first (black line) and second (red line) freezing in the stretching regions of structural H_2O. Besides, photomicrograph of such primary type fluid inclusion is shown, taken at -190 °C. 58

Figure 22. Composition of gas-bearing secondary fluid inclusions from Praid (in mol%). Blue rectangle represents massive type salt samples, whereas green triangle represents gas composition of layered type salt samples. Purple diamonds show data of Kátai (2017). 61

Figure 23. Schematic cartoon of the three microstructural processes that are known in rock salt at temperatures in the range 20-200 °C. Different shades of green mean different crystal orientations (Urai et al., 2008). 64
Figure 24. Microstructural observations with reflected light microscope and on an EBSD map. A: Photomicrograph of irradiated, etched thick section under reflected light showing halite grain boundary (black irregular thick lines) and subgrain boundaries (hairlines). White arrows show propagation of grain boundaries towards to the subgrain rich samples, causing concave grain boundaries. Black spots at the grain boundaries and inside of the substructured grain are fluid inclusions, which opened during sample preparation. Sample: PA40-PH, reflected light. B: EBSD map shows grains with different crystallographic orientation. Black arrows show the direction of the growing subgrain free grains consuming the green, subgrain rich crystal. Sample: PAT19-7..... 66
Figure 25. Strain rates – temperature plots at given differential stress calculated from the Praid samples. The strain rate paths depend on the calculated differential stress and grain size. Blue line represents strain rate of dislocation creep whereas red line shows strain rate of solution precipitation creep in the studied samples. Note that at lower temperatures, the predominant strain rate always the solution precipitation creep. The highest impact of dislocation creep manifested in the porphyroclast rich massive salt, where dislocation creep could be dominant until ~ 110 °C. 71
Figure 26. Water activity – temperature plot draws gypsum and anhydrite stability fields. Purple field indicates the temperature and water activity conditions, in saturated water, at which anhydrite crystallization is dominating. Measurements of Hardie (1967) were made under laboratory conditions. Diagram modified after Jowett et al. (1993). 73
Figure 27. Isotopic variation of S and O of anhydrite from the Badenian Salinity Crisis, Messinian Salinity Crisis and the modern ocean for comparison. Blue diamond indicates data of this study. Badenian Salinity Crisis: Claypool et al. 1980; Halas & Krouse 1982; Kasprzyk 1997; Peryt et al. 2002; Cendón et al. 2004; Messinian Salinity Crisis: Evans et al. 2015; García-Veigas et al. 2018; Longinelli 1979, modern ocean: Claypool et al. 1980..... 74
Figure 28. Effects of evaporation from freshwater sources or seawater, using two examples: Rio Grande in the USA and Mexico (G) and the river Darling in Australia (D). As crystallization process accelerates in the saturated seawater, the direction of the evaporation line will tend to curve to opposite direction: this happens when fractionation from precipitation of minerals overtakes fractionation from evaporation.(Alexandre, 2020) 79
Figure 29. Variation of δ^2H and $\delta^{18}O$ of fluid inclusions, dolomites and anhydrites occurring in massive salt rock type. Data of previous studies are shown for comparison: Badenian Salinity Crisis: Halas and Krouse (1982); Kasprzyk and Jasińska (1998). Messinian Salinity Crisis: Rigaudier et al. (2011); Evans et al. (2015). Michigan Basin brines: Wilson and Long (1993). Permian intramountain basin: Li et al. (2017). Searles Lake: Horita (1990). 81
Figure 30. Schematic map of water input and isotopic mixing in the Middle Miocene Transylvanian Basin. The water loss was compensated by western part (Pannonian Basin) seawater inflow and by the meteoric waters at the eastern part, falling and descending from the uprising Carpathian arc..... 84

List of Tables

Table 1. List of the collected samples from Praid Salt Mine. Ster: stereomicroscope, Pol: polarized light microscopy, TS: thin section, RS: Raman spectroscopy, MTM: microthermometry EBSD: electron backscatter diffraction, GI: gamma irradiation, SI: stable isotope analyses 17
Table 2. Microthermometry results of Praid salt rocks. Th = homogenization temperature, Te = eutectic temperature, T_m^{ice} = last/ice melting temperature 40
Table 3. Composition of S2-type, vapor phase fluid inclusions expressed in mol%. Calculation is based on (Dubessy et al., 1989). 44
Table 4. Raman peak positions of solid state primary fluid inclusions of Praid salt rocks expressed in relative wavenumbers ($\Delta\nu$= cm^{-1}). 46
Table 5. Isotopic composition of sulfate in anhydrite from Praid massive salt rock. 47
Table 6. Isotopic composition of carbonate in dolomites from Praid massive salt rock..... 48
Table 7. Isotopic composition of H_2O in fluid inclusions in halite from Praid massive salt rock. 49
Table 8. Quantitative analyses of microstructures performed on halite crystal subgrains..... 52
Table 9. Average subgrain size diameter of Praid salt rocks based on calculations on gamma irradiated samples. The diagram shows that the subgrain size measurement obtained from the two techniques are overlap. 53
Table 10. References of Raman peak positions, in relative wavenumbers ($\Delta\nu$ = cm-1) of the various salt hydrates spectra. 58
Table 11. Grain size statistics based on the EBSD and gamma irradiation measurements. The diagram shows that the subgrain size measurements obtained from the two techniques are overlap. The mean subgrain size of layered and massive salt is about 113 µm and 81 µm, respectively. 67
Table 12. Selected rock salt deposits of different geological settings with examined halite grain sizes and differential stress. Salt fountain shows smaller grain size and higher differential stress compared to the domal salt examples, such as Praid..... 68
Table 13. Calculated differential stress and strain rates obtained from A and B equations. The higher strain rate belongs to the solution precipitation creep. 69
Table 14. S and O isotopic composition of the Badenian Salinity Crisis evaporite and the two best known (Messinian and Permian Zechstein) salt giants. 75
Table 15. Results of stable isotopic study on primary fluid inclusion of Praid massive type salt rock. O and H isotopic composition of various evaporites are listed for comparison. 82

1. Introduction

As it is known salt rocks are very important raw materials. They have been used since the beginning of human history. For example, in the Hungarian Kingdom, in the XIII. Century the salt mines provided the same share in the royal income as the gold (Draskóczy, 2014). Evaporite deposits (including halite, anhydrite, gypsum, etc.) are the sources of many chemical products (Warren, 2006a). Due to the low permeability of halite, it can be not only an excellent caprock of carbo-hydrates but also a safe site for radioactive waste repository and hydrogen capturing (Reading and Collinson, 1996; Aquilano et al., 2016; Tarkowski, 2017). The evaluation of evaporite deposits for the above-mentioned applications usually starts with distinct scientific observations. Geochemistry and microstructural investigations are essential in the modern utilization of these evaporites. Present day challenges, related to the safe deposition of nuclear wastes and hydrogen, need cutting-edge technologies in order to make responsible decisions.

According to the definition of Warren (2010) evaporites are salt rocks precipitated from a saturated brine and preserve crystallographic evidences of their depositional process (e.g. bottom nucleation, mechanically reworking by bottom currents). This definition covers a wide range of sedimentary environments, from surface to the deep water.

This study is focusing on a Badenian evaporite deposit located in the Transylvanian Basin (TB), Romania. The studied deposit was formed during the so-called „Badenian Salinity Crisis" (BSC). The formation of BSC evaporites took place in the Paratethys realm, but its exact extension is not determined yet. The central part of Paratethys had a very complex history. Opening and closure events resulted in the appearance of endemic fauna and the formation of special sedimentary rocks (Rögl, 1998). Evaporites, as peculiar sediments of the Paratethys, occur in many areas along the Carpathian Foredeep, in the East-Slovakian Basin, and the Transylvanian Basin (Peryt, 2006). Recent studies have shown that they are also found in the Vienna Basin (Harzhauser et al., 2018) and the Pannonian Basin (Báldi et al., 2017). Several regional geological studies focusing on the basin succession are available. Remarkable micropaleontologic (e.g. Kováčvá et al., 2009; Peryt and Peryt, 2009; Mandic et al., 2019) and stratigraphic (Krézsek et al., 2010) studies were published on the BSC rocks, but there is a lack of geochemical studies on the salt deposit of the Transylvanian Basin. Geochemical data can provide significant information on the formation environment and post salt formation history, as a few studies demonstrated (for instance, the master thesis of Kátai (2017)). Moreover, studies on the fabric of Middle Miocene

salt bodies, are almost missing in the scientific literature, although evaporites play a key role in controlling the dynamical evolution of many sedimentary basins (e.g. Urai et al., 1986). The microstructural investigation provide knowledge about the deformation mechanisms affecting the salt rock, hence the TB evolution can be more understandable in this way. Thanking to several microstructural studies on salt rocks, carried out on synthetic and natural samples around the world (Guillope and Poirier, 1979; Jackson and Talbot, 1986; Urai et al., 1986; Zulauf et al., 2010), physical relations and database are available to learn the mechanical properties of BSC salt deposit.

The study location, is Praid (Parajd), located in an area in Eastern Transylvania traditionally called as "Sóvidék" (saltland), where there is a salt stem with salt mine. The salt body, with its 1.2 - 1.4 km diameter and 2.7 km height, is one of the largest salt occurrences in Europe (Horváth, 2019). The Praid Salt Mine, in its recent status, is excavated to several kms in depth ensuring a representative sampling of a whole vertical profile in the salt body. Classic and new methods were introduced in investigation for gaining a better understanding on the formation and evolution of the Middle Miocene salt of the Transylvanian Basin. This study is based mostly on the investigation of samples, collected from the Praid salt deposit.

The goals of the thesis are as follows:

1) Detailed petrographic study, in order to determine syn- and postdepositional features in the salt rock fabric. Fluid inclusion petrography has a particular role in this study because primary fluid inclusions are one of the most significant proxies of the paleo seawater. In turn, the secondary fluid inclusions can provide useful information about deformation history of the salt rock because they are witnesses of post salt deposition events and movements (e.g. fluid migration, diapirism).
2) Detailed geochemical study on the salt rocks to determine their isotopic composition. Furthermore, this thesis aimed to increase the geochemical data base of the BSC salt deposits.
3) The application of the gamma irradiation and electron backscatter diffraction methods were the first and successful attempts to visualize the dominant microstructure of the Transylvanian salt rocks. The results are expected to be applicable for quantification of the stress parameters and estimation of the strain rates dominating in the salt body.

4) Carrying on the first stable isotopic measurements on minerals and fluid inclusions of the Transylvanian evaporites to gain better understanding of the paleo environment of the salt generation, developing a new technique for stable isotope analysis on fluid inclusions.

5) Making a synthesis from the results of petrographic and geochemical studies.

2. Geologic background

2.1. Evolution of the Transylvanian Basin

The Transylvanian Basin (TB), is located in the Eastern part of the Carpathian-Pannonian region (CPR), surrounded by the Apuseni Mountains (Erdélyi-szigethegység), Eastern- and Southern Carpathians (Fig. 1).

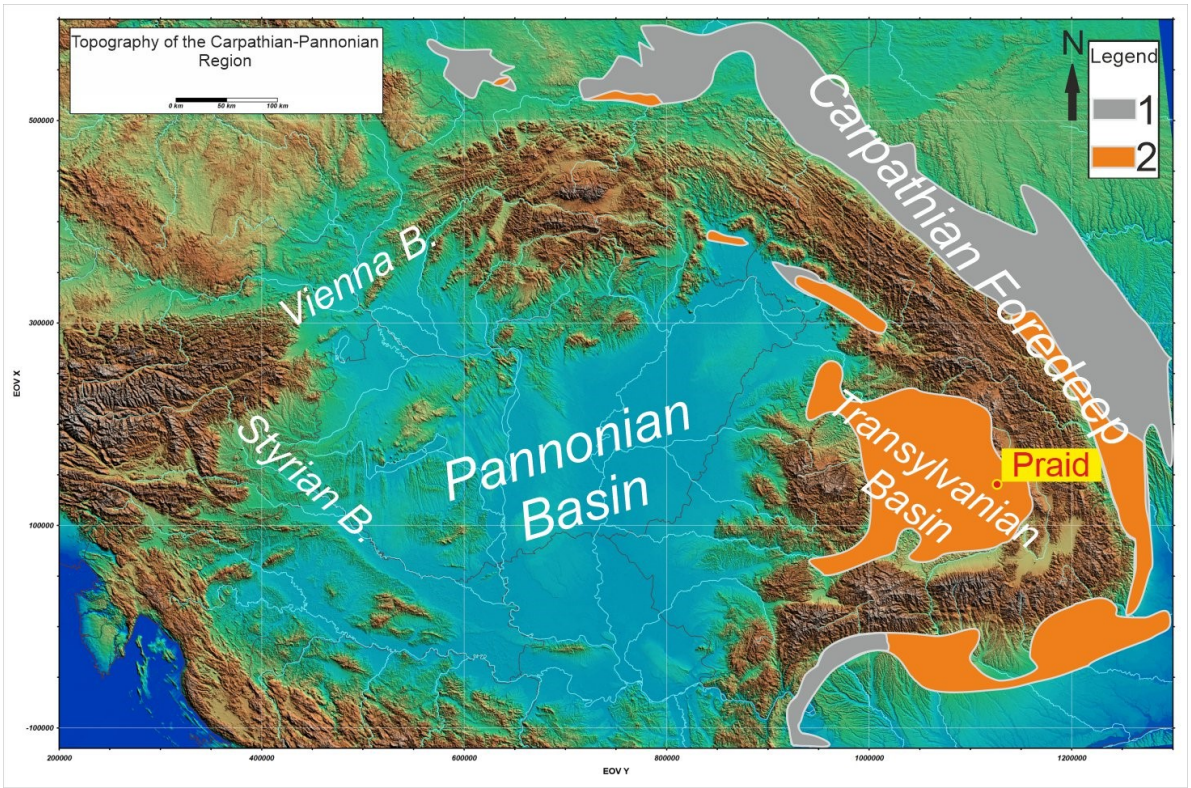

Figure 1. Topographical map completed with Middle Miocene evaporite occurrences of the Carpathian-Pannonian region. The study area (Praid) is located at the Eastern part of the Transylvanian Basin. 1: gypsum 2: halite accompanied with anhydrite/gypsum (map redrawn after Popov et al. (2004); Peryt (2006); Horváth et al. (2006); Báldi et al. (2017)***)***

The main geodynamic processes, determining the landscape of the CPR, are related to the closure of Neotethys (Horváth, 1993; Schmid et al., 2008). The basement of the TB is formed by the Tisza and Dacia tectonic blocks sutured during the Cretaceous (Csontos et al., 1992). The TB is a circular shaped Intra-Carpathian sedimentary basin that started to fill up from the Late Cretaceous (Krézsek and Filipescu, 2005). There are some similarities in the evolution of the TB and the neighboring Pannonian Basin but major differences also occur (Huismans et al., 1997). Both basins developed in a back-arc type tectonic setting (e.g Balintoni et al., 1997). The most

significant differences are the followings: the higher thickness of the continental lithosphere (Szafián et al., 1999), the lower heat flux (45 mW/m^2) (Lenkey et al., 2001), and the lack of extensional structures starting from the Miocene (Krézsek and Filipescu, 2005; Krézsek and Bally, 2006; Tiliță et al., 2018) in the TB.

Most of our knowledge about the pre-Miocene stratigraphy of the TB is based on seismic and borehole data, but occasionally, due to the folding structures, some older (Mesozoic) formations crop out at the edge of the basin to study.

The basement of the TB consists of Permian – Jurassic carbonates (dolomites, limestones) and large sheets of supra-subduction ophiolites (Schmid et al., 2008; Tiliță et al., 2018). Upper Jurassic granitoid intrusions and calc-alkaline volcanics are also intercepted in boreholes (e.g. Ionescu et al., 2009). The Upper Cretaceous sediment succession (conglomerates, sandstone, carbonaceous marls and rudist limestone), sealing the basement nappes, has variable thickness (100 to 1000 m) (Krézsek and Bally, 2006). These sediments are exposed at the footage of the Apuseni Mts. and in the Carpathians (Willingshofer et al., 1999; Schuller, 2004).

Initially, in the Paleocene, compressional stress field dominated the area of TB (Fodor et al., 1999) similar to the Transdanubian Paleogene Basin (Kercsmár et al., 2006). In the TB, the early basinfill terrigenous sediments (e.g. Jibou Fm.) are sandstones, with evaporitic episodes and shales with a thickness of 500 m (Proust and Hosu, 1996). Both shallow marine (~100 m) and deeper marine (~500-1000 m) deposits were described earlier by Paraschiv (1979).

In the Lower Miocene the Tisza-Dacia microplate was in the synrift phase and moved towards the European Platform. The ALCAPA (ALpine CArpathian PAnnonian) microplate thrusted to the Tisza-Dacia resulting a forearc basin in the northern part of the TB (Csontos and Nagymarosy, 1998). Foredeep wedge sediments were recorded in response to the thrusting of ALCAPA. The end of Paleogene is characterized by a large amount of erosion until the offset of the sub-sequent Miocene deposition cycle (Paraschiv, 1997; Tiliță et al., 2018). The local stage, Badenian (Middle Miocene) started with marine transgression (Filipescu and Gîrbacea, 1997).

The transgression was followed by gradual basin deepening, and locally important tuff-like sediments were deposited in a submarine environment (Szakács et al., 2012). The layered, graded complex of volcanoclastic deposits, called Dej Tuff is overlain by the evaporites, which are the subject of this thesis (Fig. 2). The halite–gypsum association is deposited basin-wide with a minor amount of massive, nodular and fibrous gypsum. The average thickness of the evaporite could be

around 300 m (Krézsek et al., 2010). Since deposition, the salt was affected by large-scale diapirism, resulting in km thick salt diapir alignments (Fig. 2-3). In the Sarmatian, the salt rock was covered by deep marine marls (Krézsek and Bally, 2006; Krézsek et al., 2010).

Beside marine sediments, more than one km thick sediments deposited over the salt layer including product of the subsequent Miocene-Pliocene volcanism (Szakács and Krézsek, 2006).

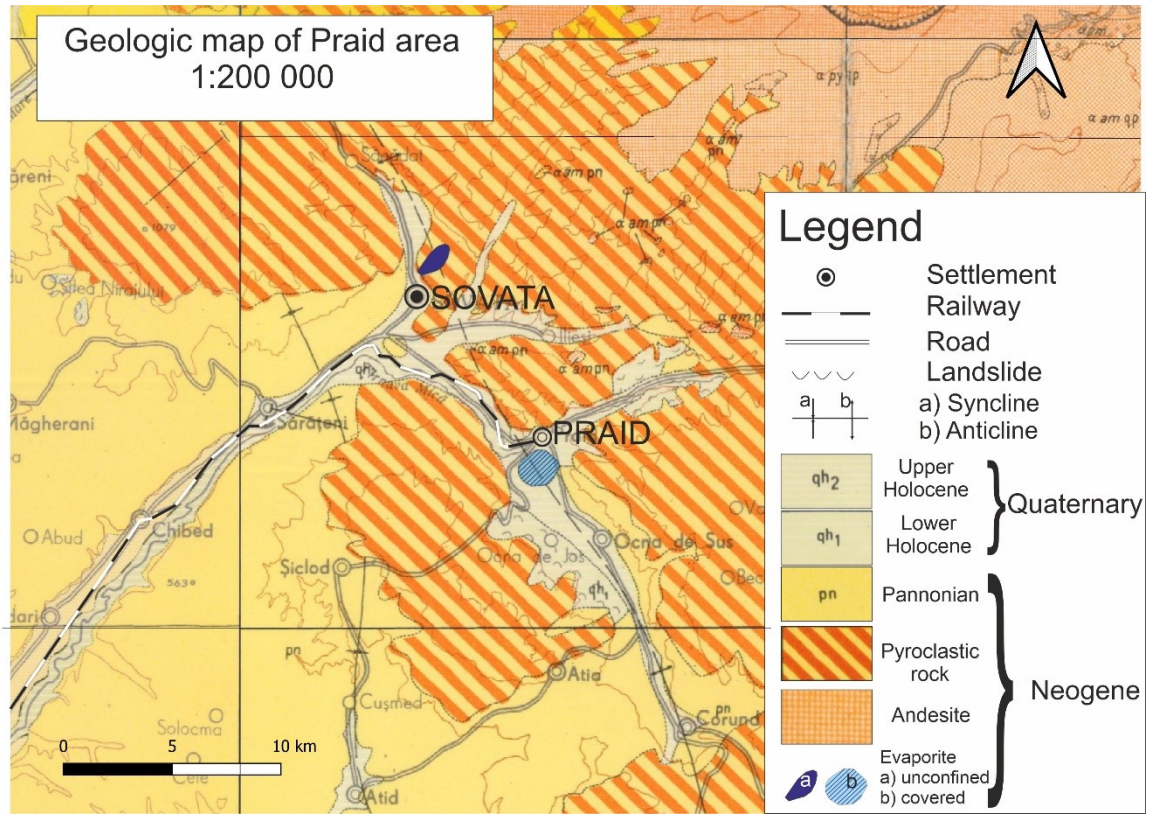

Figure 2. Geologic map of the study area. Pyroclastic rock and Pannonian sediments dominated the area. Badenian evaporites exposed at Sovata and Praid suiting in the line of Eastern Diapir Alignment with NW-SE direction. Map scale: 1:200 000. Modified after Dumitrescu et al. (1970)

The initiation of the volcanism could be related to the descent of the Vrancea slab (Sperner et al., 2004; Pécskay et al., 2006). From the Late Miocene to the Quaternary there were several intensive periods of volcanism resulting in the Eastern Carpathian volcanic chain (Calimani/Kelemen-Gurghiu/Görgényi Mts., Harghita/Hargita Mts., Persani/Persány Mts.) with different petrologic compositions (basaltic, andesitic, and dacitic) (Szakács and Seghedi, 1995; Pécskay et al., 2006; Szakács and Krézsek, 2006).

The post-evaporite strata are often affected by evaporite-related tectonic events. Seismic profiles of these halokinetic structures are illustrated by (Krézsek and Bally (2006). The salt

structures of the basin generally trend NW to SE, and form two diapiric alignments near the eastern and western edges of the TB (Fig. 3).

In the Pannonian, the TB has become a lake, filled up by sediments carried by rivers coming from the surrounded mountains (Carpathians, Apuseni Mts.). During this time, the tectonic regime changed to basin inversion which resulted in general uplift of the TB (Krézsek and Bally, 2006; Tilita et al., 2015) and enormous movements of the rheologically weak sediments, namely the salt.

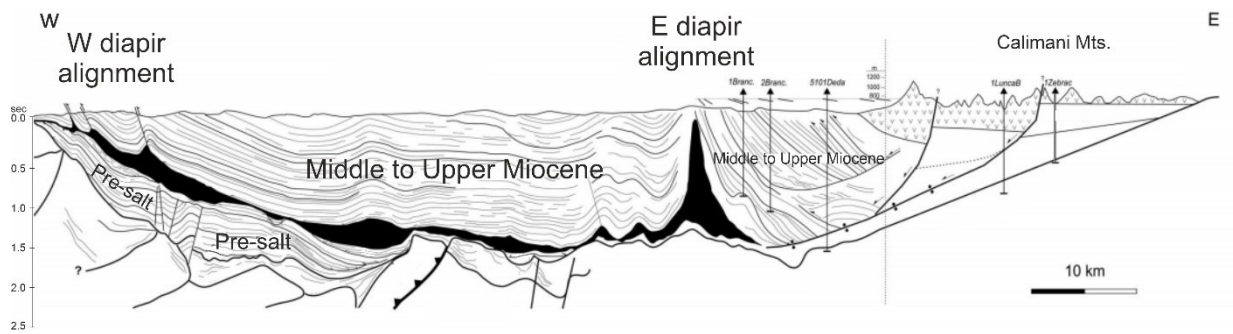

Figure 3. Seismic interpretation of a W-E section of the Transylvanian Basin. Black body represents the highly plastic salt layer. The Middle Miocene evaporite forms diapir alignments along the basin margin (Profile modified after Krézsek and Bally (2006)***.***

The further uplift of the Carpathians led to the formation of Lake Pannon, because of the continental collision, which completely cut off the Intra-Carpathian realm from the rest of the Paratethys to the end of Late Miocene (Magyar et al., 1999). The lacustrine environment turned to continental setting in the Pleistocene, causing significant erosion (Sztanó et al., 2005) in the CPR, at least 500 m sediment could have been eroded (Sanders et al., 2001) in the TB.

2.2. The Badenian Salinity Crisis in the Transylvanian Basin

The two major conditions of marine evaporite formation are 1) a restricted flow system cutting off a basin from the open ocean (anti-estuarine circulation) and 2) a warm climate, both necessary to form hypersaline waters (Warren, 2006b; De Leeuw et al., 2010). During the Cenozoic era there was a sea, which expanded from Western Europe to the Indian Ocean called Paratethys (Báldi, 1980; Rögl, 1998).

The Paratethys is divided to Western, Central and Eastern parts. In the Middle Miocene, the Central Paratethys, which cover the CPR, was closed from the Eastern-Paratethys and had a

restricted inflow from the Mediterranean Sea (Báldi et al., 2017), which was an indirect contact with the Atlantic Ocean (Fig. 4).

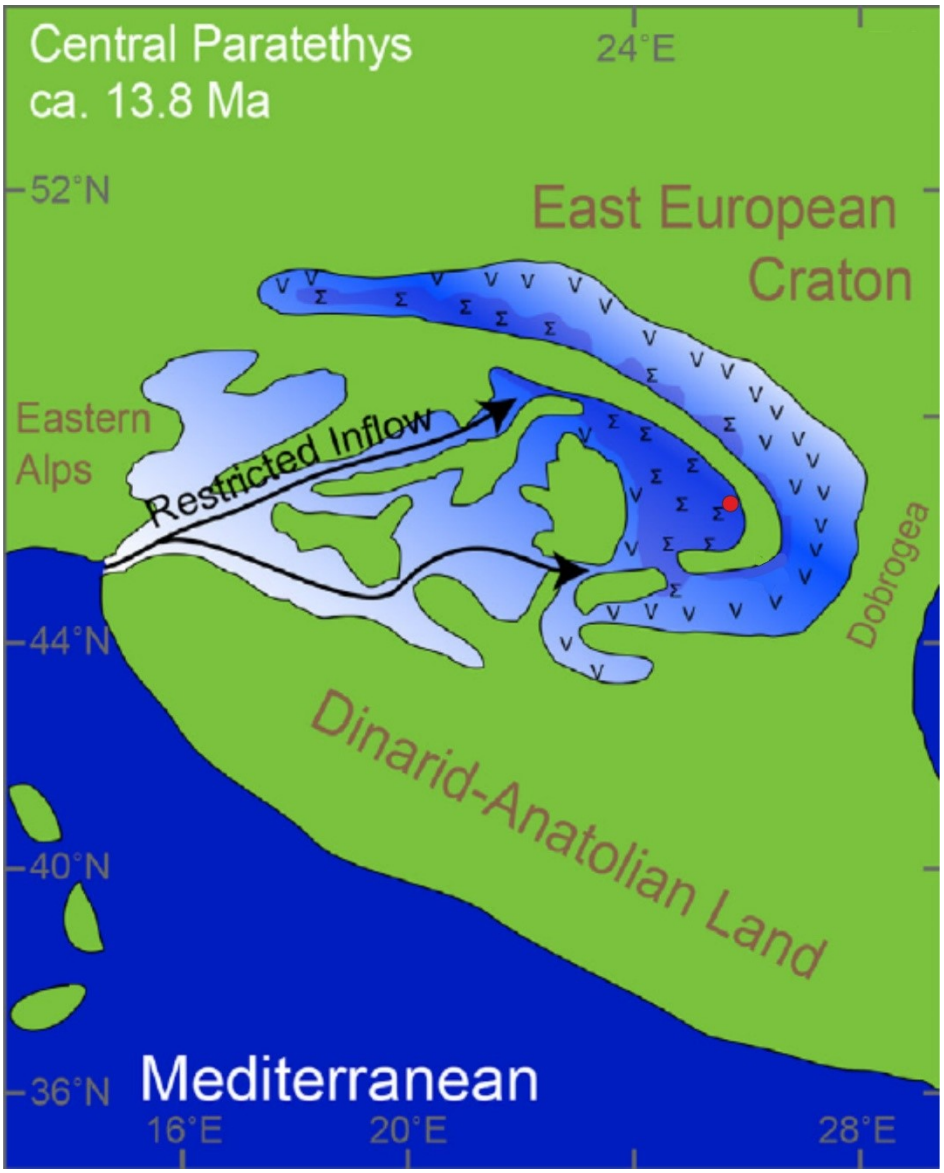

Figure 4. Simplified paleogeographic reconstruction of Mediterranean-Paratethys connection during Badenian Salinity Crisis interval (both modified after (de Leeuw et al., 2018)***. Red closed circle marks the location of studied area.***

The most accurate value for the oldest age of the salt resulting from Ar-Ar radiometric age dating technique (De Leeuw et al., 2010) applied to salt enclosed Dej Tuff fragments found at Praid 13.8 ± 0.08 Ma. However, Szakács et al. (2012) dated the Dej Tuff complex at ca 15 Ma. The age of a volcanic ash layer interlayered in marl sequence overlying the salt formations suggests that the Badenian Salinity Crisis (BSC) ended before 13.32 ± 0.07 Ma (de Leeuw et al., 2018).

The real conditions (temperature, water depth) of the salt formation in the TB is still a matter of debate. Controversial conclusions were drawn in the lack of sufficient information. Based on stratigraphic, seismic and borehole data, Krézsek & Bally (2006) suggested a deep marine origin of the salt, which is supported by Tilita et al. (2015). Furthermore, Unger and Leclair (2018) provide another idea, which is based on deep marine colloidal processes, due to the membrane polarization and reverse osmosis, which generates the Deep Hypersaline Anoxic Basins/Lakes with intensive microbial hotspot i.e. methane generation bacteria. Due to Middle Miocene isolation of the Central – Paratethys (Palcu et al., 2017; Harzhauser et al., 2018), the blockage of the deep saline outflow had driven to brine formation and later halite precipitation and accumulation. Meanwhile, the evaporites of the Outer Carpathians are determined as of shallow marine origin and mechanically reworked sediments (Cendón et al., 2004; Peryt and Peryt, 2009).

Although, there was no previously found sign of evaporite deposition in the western part of the Central-Paratethys (Pannonian Basin, Vienna Basin), recent studies had demonstrated that the BSC extended to the Pannonian Basin, too (Palotai and Csontos, 2012; Báldi et al., 2017). These new results urge a review of the temporal geological evolution and their mechanisms of the Badenian in the TB.

3. Samples and analytical methods

3.1. Sampling and sample preparation

In some places the diapirs in the TB attain more than 2 000 meters height such as the Praid diapir located at the western peripheries of the Gurghiu Mountains. Hand specimens were collected from the Praid Salt Mine (boundary pillars and chamber walls) (Table 1). Mining operations excavated a mine in the upper 400 m of the diapir where salt was, and still is, extracted for centuries (Fig. 5). Several levels of the mine were sampled in four field campaigns in the last three years. The observed salt rocks can be classified into at least two occurrence types, according to their color and structure (Fig. 5/B-C). One is named as **layered type**, because white and grey salt layers alternate in it. This type of salt shows large scale (tens of meters) folds visible in the mine walls (Fig. 5/B, Fig 6/B). The other observed salt from, named **massive type**, does not show any visible structure (Fig. 5/C, Fig. 6/A), except some single vertical cracks filled in with clear white salt contrasting with the light grey color of the host salt (Table 1). This massive salt rock type has several shades of grey color suggesting the presence of variable amounts of clay besides halite. The massive salt rock type is classified as 'road salt' according to the Mining company technical wording. The contact of the two types of salt is not exposed in the mine.

Table 1. List of the collected samples from Praid Salt Mine. Ster: stereomicroscope, Pol: polarized light microscopy, TS: thin section, RS: Raman spectroscopy, MTM: microthermometry EBSD: electron backscatter diffraction, GI: gamma irradiation, SI: stable isotope analyses

Salt rock type	Sampling site	Code	Description	Applied techniques	Remark
Layered	Chamber 40	PA40-1	greyish, translucent, coarse-grained massive salt rock	**Ster**, **SI**	
Layered	Chamber 40	PA40-2	greyish, translucent, coarse-grained massive salt rock	**TS**, **Pol**, **Ster**, **SI**	
Layered	Chamber 40	PA40-3	clear white, translucent massive halite	**Ster**	
Layered	Chamber 40	PA40-4	clear white, translucent massive halite	**TS**, **Pol**, **Ster**, **RS**, **GI**	
Layered	Chamber 40	PA40-5	layered coarse grained salt rock, with alteration of grey and white layers	**Ster**	
Layered	Chamber 40	PA40-6	layered salt rock, with alteration of grey and white layers	**Ster**	

Layered	Chamber 40	PA40-7	layered salt rock, with alteration of grey and white layers	**TS, Pol, Ster**	
Layered	Chamber 40	PA40-8	Layered salt rock, with alteration of grey and white layers	**Ster**	
Layered	Chamber 40	PA40-9	layered salt rock, with alteration of grey and white layers	**Ster**	
Layered	Chamber 40	PA40-10	layered salt rock, with alteration of grey and white layers (4-5 cm	**TS, Pol, Ster**	
Layered	Chamber 40	PA40-11	layered salt rock, with alteration of grey and white layers	**Ster**	
Layered	Chamber 40	PA40-12	layered salt rock, with alteration of grey and white layers	**Ster**	
Layered	Chamber 40	PA40-PH	layered salt rock, with alteration of grey (5-8 cm) and white layers (2-5) cm	**TS, Pol, Ster, MTM, RS, GI, EBSD, SI**	oriented sampling
Undefined	Visitor Level	PAE17-1	white bladed habit mineral (5-10 cm) embedded in grayish brown clay	**TS, Pol, Ster**	collected from a huge clay block
Undefined	Visitor Level	PAE17-2	white vein (~5 cm) embedded in brownish clay	**TS, Pol, Ster**	collected from a huge clay block
Layered	Visitor Level	PAE17-3	greyish-brownish, translucent, coarse-grained salt rock	**TS, Pol, Ster, RS, MTM, SI**	core sample
Undefined	Visitor Level	PAE17-4	white anhydrite vein (5-10 cm) in grayish brown clay	**Ster**	
Undefined	Gallery to the Visitor Level	PAE17-5	greyish coarse-grained salt rock with fiber-like orange patch	**Ster, RS, SI**	
Massive	Telegdy Mine	PAT17-1	greyish, translucent, coarse-grained massive salt rock with deformational fabric	**Ster, SI**	
Massive	Telegdy Mine	PAT17-2	greyish, translucent, coarse-grained massive salt rock	**TS, Pol,Ster, SI, GI**	
Massive	Telegdy Mine	PAT17-3	greyish, clayey, coarse-grained massive salt rock	**TS, Pol, Ster, RS, GI**	

Massive	Telegdy Mine	PAT17-4	greyish, translucent, coarse-grained massive salt rock	**TS**, **Pol**, **Ster**, **RS**, **MTM**, **EBSD**, **SI**	several elongated, > 1 cm grains
Massive	Telegdy Mine	PAT17-5	greyish, translucent, coarse-grained massive salt rock	**Ster**	
Massive	Telegdy Mine	PAT19-1	greyish, translucent, coarse-grained massive salt rock	**Ster**, **SI**	collected from the ground
Massive	Telegdy Mine	PAT19-2	greyish, translucent, coarse-grained massive salt rock	**TS**, **Pol**, **Ster**, **SI**	
Massive	Telegdy Mine	PAT19-3	greyish, translucent, coarse-grained massive salt rock	**TS**, **Pol**, **Ster**, **SI**	core sample
Massive	Telegdy Mine	PAT19-4	greyish, translucent, coarse-grained massive salt rock	**Ster**, **SI**	
Massive	Telegdy Mine	PAT19-5	bright grey massive salt rock with large (> 1 cm) elongated grains	**TS**, **Pol**, **Ster**, **SI**, **GI**	
Massive	Telegdy Mine	PAT19-6	greyish, translucent, coarse-grained massive salt rock	**TS**, **Pol**, **Ster**, **SI**	
Massive	Telegdy Mine	PAT19-7	greyish, translucent, coarse-grained massive salt rock	**TS**, **Pol**, **Ster**, **RS**, **EBSD**	white vein
Massive	Telegdy Mine	PAT19-8	dark greyish massive salt rock	**Ster**, **SI**	
Massive	Telegdy Mine	PAT19-9	alternation of clear white and greyish massive salt rock	**Ster**, **SI**	

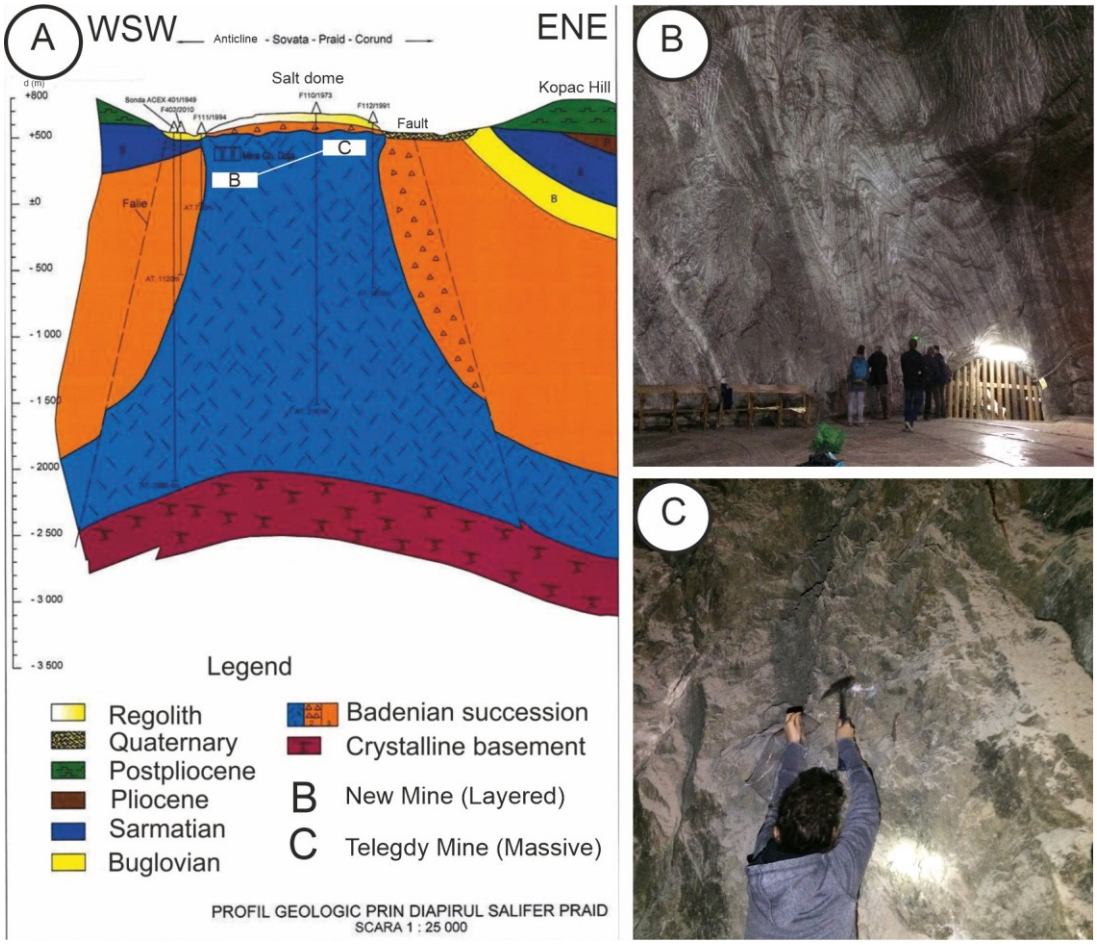

Figure 5. A schematic profile through the Praid salt dome. The salt (blue color) brakes through the younger rocks (Buglovian is a locally used substage referring to late Badenian). A thin (couple of meters) young regolith layer covers and prevents the salt dome from dissolution and erosion. The mine is situated in the upper 400 m of the salt body. B: Layered type salt in the Praid Salt Mine (Visitor Level) showing folded structure. C: Massive type of salt from the Telegdy mine. Photo courtesy on behalf of the Praid Salt Mine for picture A.

The collected hand specimens (Fig. 6) were subjected to different sample preparation procedures as required for the applied (microstructural and geochemical) analytical techniques in this thesis (Fig. 7).

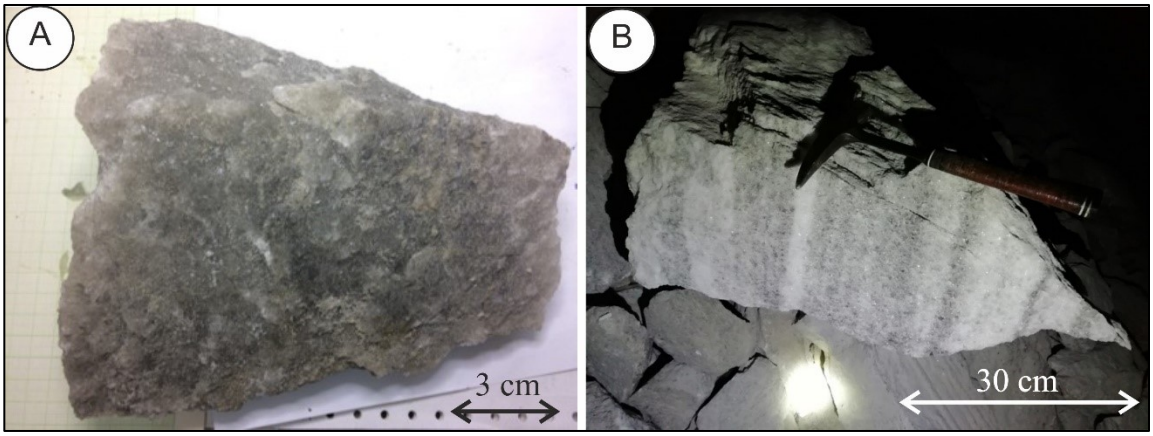

Figure 6. Characteristic samples from Praid Salt Mine. A: massive type salt rock sample (PAT19-5) B: layered type salt rock sample (PA40-PH).

Cutting and polishing of the samples were made in totally dry conditions at the Lithosphere Fluid Research Lab operated at Department of Petrology and Geochemistry, Eötvös Loránd University, Budapest using a Buehler Isomet low-speed saw. Samples were grinded and polished with P800 and P1000 Buehler discs. Thin and thick sections were made for petrographic studies and textural characterization. Furthermore, detailed fluid inclusion (FI) study had been carried out on selected samples which required double polished thick sections and grains.

Besides the thin sections, single grains were also polished for microthermometry, Raman spectroscopic and stable isotope studies. All the samples had been stored in a dried exsiccator to minimalize the effect of air moisture. Selected salt rock samples were dissolved to obtain insoluble mineral constituents, from which anhydrite and dolomite grains were collected by hand pick up for isotopic study. The separates were cleaned in an ultrasonic water bath.

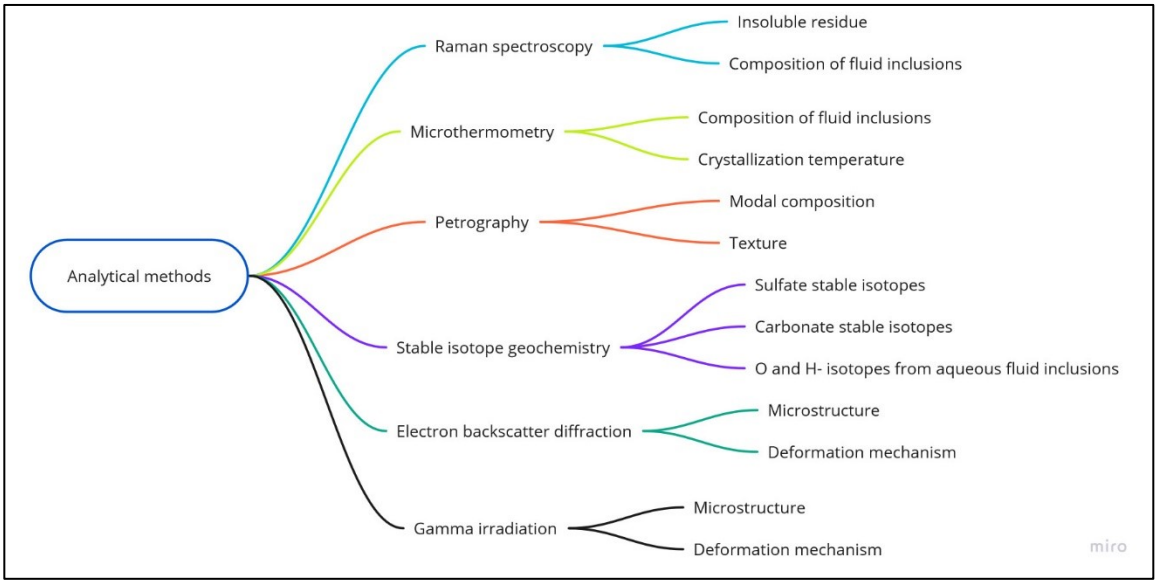

Figure 7. Map of the applied analytical methods.

3.2. Petrography with polarized light microscopy

Petrography was carried out on representative polished thick and thin sections at the Lithosphere Fluid Research Lab using a Nikon Eclipse E600POL polarized light microscope. Photomicrographs were taken with a Nikon DS Fi1 camera operating with NIS Elements AR 2.20 image editor software.

Fluid inclusion petrography was based on Roedder (1984). The **primary (P-type) fluid inclusions** representing the mother solute of the mineral, assuming that the composition of inclusion has been remained unchanged since the entrapment.

The other group of fluid inclusions includes the **secondary (S-type) fluid inclusions**, which are a collection of inclusions formed after the host halite crystallization. The main difference between the two type is the timing of entrapment. P-type FIs are synsedimentary in origin, whereas S-type FIs definitely formed after the host mineral crystallization and they are occurring along microfractures as a result of several geological processes.

Fluid inclusion assemblages (FIA) defined by Roedder (1984) were distinguished in the study as the most finely discriminated, petrographically associated, group of inclusions. They are, in my thesis, distinguished accordingly.

The microstructural characterization of salt rocks was based on Trouw and Passchier (2005).

3.3. Microthermometry

Microthermometry is termed as the determination of temperatures of phase changes within fluid inclusions during heating and cooling of samples (Goldstein and Reynolds, 1994). The technique was followed Goldstein (2001) and Speranza et al., (2013), specified to halite hosted primary brine inclusions.

Microthermometry measurements were carried out using a Linkam THMS600 type heating-cooling stage of the Lithosphere Fluid Research Lab. The stage was calibrated with synthetic fluid inclusions of CO_2 (triple point at -56.6 °C). The analytical error of the measurements is about 0.2 °C. The stage is adapted to a Nikon ECLIPSE LV100 POL transmitted-light microscope, equipped with long working distance objectives (10X, 50X) and camera. Homogenization (T_h) and eutectic (T_e) temperatures were measured.

During T_h measurement, one has to record the temperature when the gas phase bubble homogenizes into the liquid phase. Noteworthy to mention is that the P-type fluid inclusions of

Praid are in metastable phase, showing only liquid phase at room temperature instead of having both liquid and vapor in the inclusions. To force bubble nucleation, then to obtain the (T_h), the FIs were first cooled to – 20 °C. The freezing of these fluid inclusions, due to their H_2O content, could lead to volume increase within the inclusion cavity and thus it might to decrepitate. At this temperature the FIs could overcome the metastable barrier and still any solid phase could occur, because of the presence of NaCl (phase transition from liquid to solid phase in a NaCl-solution is expected under -21 °C). In this way the leakage and erroneous measurement of the fluid inclusions can be avoided.

The following step was another cooling interval down to -100 °C to get the FIs in solid phase.

Then, they were slowly (5 °C/min) heated until the first visible phase transition (solid -> liquid) was observed at certain temperature, which is the eutectic temperature (T_e).

3.4. Raman microspectrometry

Identification of solid, liquid, and gas species was performed with a confocal HORIBA Labram HR (high resolution) 800 spectrometer of the Research and Instrument Core Facility of the Faculty of Science, Eötvös Loránd University. The instrument was operating with a Nd:YAG laser (l = 532 nm) excitation, 600 and 1800 grooves/mm optical grating, 50 µm confocal hole, 2–120 s acquisition time. An Olympus petrographic microscope with 50x and 100x objectives was used to focus the laser on the selected inclusions. Raman spectra of salt hydrates at low temperatures were recorded by the combination of the Linkam heating-freezing stage and the Raman microspectrometer. Generally, 50x magnification was used with the stage, with long working distance objective. In the case of freezing measurements on fluid inclusions 100 µm confocal hole was used. The laser power was 130 mW at the source and ~40 mW on the surface. The spectral resolution was 0.7 cm^{-1} at 1398.5 cm^{-1} and 0.6 cm^{-1} at 2331 cm^{-1}). LabSpec software was used for data processing. The identification of and liquid and vapor phases based on Frezzotti et al. (2012). The identification of the solid phases in cryogenic measurement is based on the databases of, Baumgartner and Bakker (2010), Dubessy et al (1982) and Vítek et al. (2009). The second freezing method, applied by Ni et al. (2006) and Samson and Walker (2000), was used to collect the spectrum. The solid salt hydrates have characteristic Raman spectra, therefore it is able to determine the major ion composition of FIs qualitatively. Saturated water inclusions have variable freezing behaviors, reflecting highly metastable phase assemblages (Baumgartner and Bakker,

2009). Molar fractions cannot be calculated, since natural inclusion is a complex system and the distribution is heterogenous as well as the orientation of the crystallites (in solid phase), thus the relative intensities of different shifts on FIs have only a limited significance.

3.5. Stable isotope studies

All the stable isotopic measurements were completed in the ICER Laboratory (Isotope Climatology and Environmental Research Centre), Institute for Nuclear Research, in Debrecen, Hungary. Sample preparation of primary fluid inclusions (FIs) trapped in halite was carried out in a self-developed way. Pre-selection (polishing of halite grains then observing under the microscope whether they contain primary FIs and choosing the appropriate ones) of halite grains, anhydrite and dolomite separation was made in Lithosphere Fluid Research Lab. The further preparation procedure of fluid inclusions for stable isotopic measurement was developed together with experts from the ICER Laboratory. The process belongs to the off-line methods (Hoefs, 2009) and contains the following steps:

1) Selected primary fluid inclusion rich halite samples (200-300 mg/ tube) were introduced into stainless-steel tubes with a stainless-steel ball (Fig. 8/A.).

2) The upper end of the tubes was connected to vacuum system which also has a U-shape glass capillary (vial).

3) The stainless-steel tube was heated to near 300 °C under vacuum for 30 minutes to get rid of atmospheric oxygen and hydrogen (absorbed on the sample and the tube wall) from the system.

4) After pre-heating, liquid N_2 was placed under the U-shape capillary vial. In this way the vial functioned as a trap of the liberating H_2O (Fig. 8/B).

5) The H_2O was extracted by crushing the halite in the stainless-steel tube. Moving the steel ball with a magnet, halite chips could be crushed, thus the fluid inclusions of the halite grains could break up and release their fluids under the vacuum.

7) After thoroughgoing crushing of the halite chips, the tube was heated up to 300 °C for 30 sec to move all of the water molecules from the tube to the cold trap, thereby H_2O was gathered in the cooled vial.

8) With a propane-butane gas torch, the vial was welded at both ends. Then, the sample holder vials were shortened by further welding in order to size them to the instrument inlet.

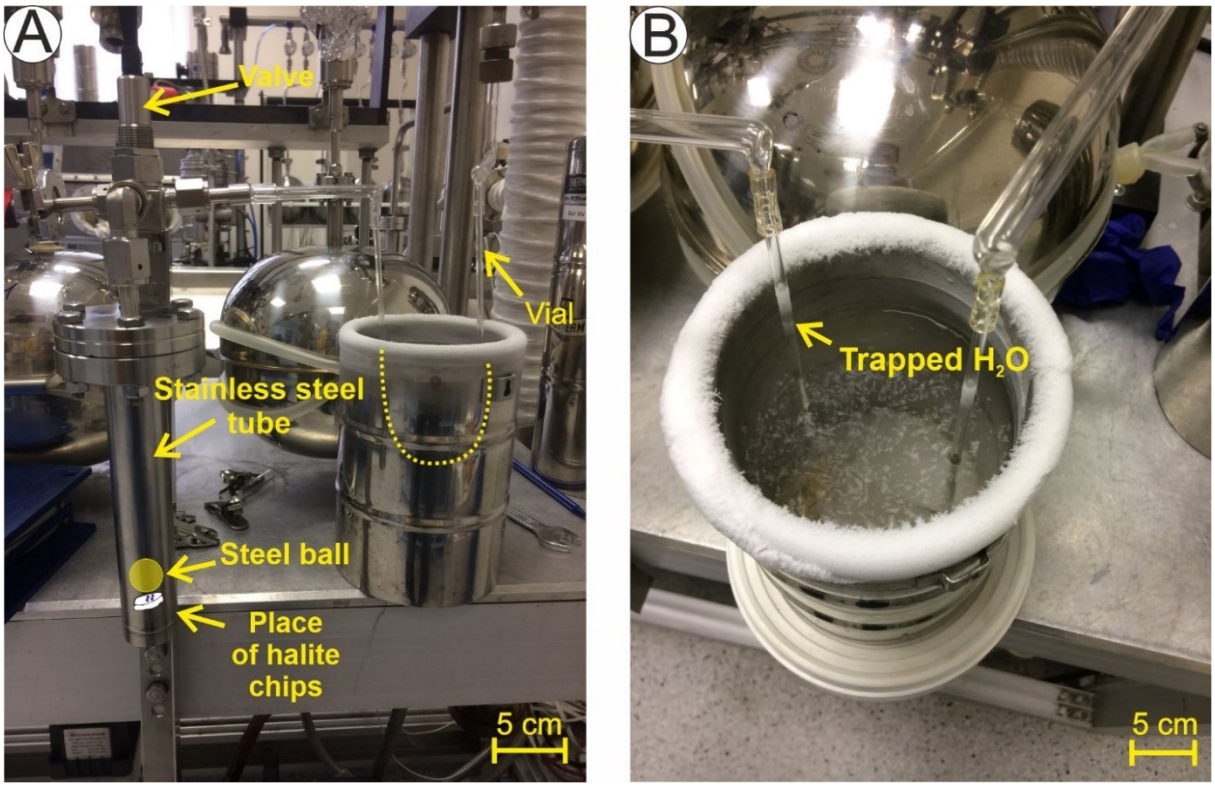

Figure 8. Ongoing preparation process in the ICER Laboratory Institute for Nuclear Research, Debrecen. A: Copper tube, containing halite grains is connected to the vacuum system. In the pre-heating part of the procedure the glass capillary vial cannot trap any molecules. B: Glass vial in liquid nitrogen is serving as a trap. The liberated water from fluid inclusions freezes on the wall of the vial.

Aqueous FI isotopic study was carried out with a Los Gatos T-LWIA-45-EP cavity ringdown spectroscope. Water of inclusions was analyzed and then expressed as δ^2H, $\delta^{18}O$ relative to V-SMOW (Vienna Standard Mean Ocean Water) international standard. Water blanks had very low amount of water, showing minor role in the total amount of water extracted from the samples. The total volume of extracted fluids ranges between 1-2 µl per samples on average.

The dolomite crystals from Praid salt rock were hand-picked from the washed and dried residues. Then the carbonate minerals were prepared with orthophosphoric acid treatment (at 70 °C for 24 hours) to extract the CO_2.

The anhydrite crystals from Praid salt rock were hand-picked from the washed and dried residues. Samples were pyrolyzed with Temperature Conversion Element Analyzer (TC/EA) to obtain carbon-monoxide for $\delta^{18}O$ analysis. Samples were combusted at 1030 °C in a Flash Element Analyzer (EA) for $\delta^{34}S$ analysis with a Thermo Finnigan Delta^{plus} XP. The delta values were calculated by the following equation: $\delta = (R_{sample}/R_{standard}-1)*1000$, where R is the $^2H/H$,

$^{18}O/^{16}O$, $^{34}S/^{32}S$ or $^{13}C/^{12}C$ ratio in the sample or in the international standard. The carbon isotopic ratio was expressed as $\delta^{13}C$, relative to V-PDB (Vienna Pee Dee Belemnite) standard. Values of $\delta^{34}S$ were expressed relative to V-CDT (Vienna Canon Diablo Troilite) reference. Values of $\delta^{18}O$ were expressed relative to V-SMOW. The precision of the measurements is better than ± 0.15 ‰ for $\delta^{18}O$, ± 2 ‰ for $\delta^{2}H$, ± 0.1 ‰ for $\delta^{13}C$ and ± 0,3 ‰ for $\delta^{34}S$.

3.6. Electron Backscatter Diffraction

Electron Backscatter Diffraction (EBSD) is a powerful tool to investigate the microstructure of a material. The EBSD method can demonstrate the possible deformation mechanisms which were active in the sample. For microstructural investigation of salt rocks as flat as possible sample surface had to be made. Raw samples were cut dry to obtain slabs (ca. 1 x 1 x 0,5 cm) with a precision diamond saw paying high attention to avoid micro-cracking and dissolution artefacts. Then the slab was polished (until 1 µm polishing cloth) and etched in a slightly undersaturated (~5.5 mol %) NaCl solution for 10 sec. Immediately after that, the sample was wiped with a microfiber cloth, then sprayed with n-hexane and finally dried with pressurized air. These steps were made following Urai et al. (1986) and advices of Jolien Linckens (personal communication).

The EBSD studies were performed on a FEI Quanta 3D scanning electron microscope of the Research and Instrument Core Facility of the Faculty of Science, Eötvös University, Budapest. The electron microscope is equipped with an EDAX Hikari camera and was operating with 4 nA probe current and 20 keV acceleration voltage. The sample stage was tilted to 70°. The step size (resolution) of the EBSD map was 15 µm. Data were acquired and evaluated with Orientation Imaging Microscopy (OIM) 7.0 software. The average EBSD image quality (IQ) was satisfying, 43000 in average and the maximum value was 66000, which shows that the majority of the measured points were successfully indexed. The maps were further processed to remove false indexed data (e.g. holes, cracks on the surface) to provide more coherent microstructure maps. The amount of removed points were very few (< 1.5 %).

Grain and subgrain size evaluation were performed with a python-script (https://github.com/tovask/EBSD/blob/master/filter_and_sum_misorientations.py)

3.7. Gamma-irradiation

Sample preparation of irradiated samples is very similar to that of the EBSD measurements. Salt samples were cut into slabs (1 x 1 x 0,5 cm). The microstructure of the salt samples was decorated by gamma-irradiation experiment which took place at the Radiation Chemistry Department of the Centre of Energy Research, Eötvös Loránd Research Network (ELKH) Budapest. The settings of irradiation operation were similar to Urai et al. (1986) and Schléder and Urai (2005). The radiating source was ^{60}Co isotope and the temperature was ~ 35 °C. One

irradiation was performed at dose rate between 1 kGy/h and 3 kGy/h to total dose of about 1,5 MGy. The other set was performed at 4kGy/h to 6 kGy/h and also to the total dose of 4 MGy. As a visible result, the salt sample slabs became brown colored heterogeneously. After irradiation, the slabs were polished and etched to remove scratches and provide a submicroscopic relief on surface. Subgrain structure were examined under reflected light microscopy. Quantitative analysis of microstructures was performed to further differential stress and flow law calculations. Grain and subgrain statistics of microstructures digitized in CorelDraw were made with a grain size calculator program (https://gitlab.com/wilzegers/particle-size-calculator) written in C++.

4. Results

4.1. Results of petrography

Since the two types of salt rock in the Praid mine can be readily differentiated macroscopically the laboratory observations, experiences and analyses were performed on both types.

Massive grey salt. Deformational fabric with moderate foliation was observed. Large (> 1 cm in size) elongated euhedral large grains are surrounded by sub-millimeter sized halite grain mélange. Relatively small (< 1 mm in size) grains without fluid inclusion and substructure compose the mélange (Fig. 9/A). The grainsize distribution is bimodal, the average grain size ranges between 1.3 and 1.5 mm. Halite grain boundaries are usually euhedral shaped and filled with minerals such as anhydrite, dolomite, and detrital minerals in the clay fraction. The bounding curves of halite grains sometimes have an irregular lobate morphology. The above-mentioned cm-size elongated grains defined as chevron-like grains usually contain primary fluid inclusions. The etched surfaces of the samples show polygonal shaped subgrains. Deformational fabric with moderate foliation was observed. Clay minerals are present in the grain boundaries in variable abundance. Where the clay mineral content is high, the grain size of halite is relatively smaller than in the clear halite. Some cm-size slightly greenish clay clusters are incorporated in the massive halite matrix, which are considered as weathered tuff. This type of salt rock has a slightly protomylonitic texture, similar to Paleogene Iranian rock salts defined by Schléder and Urai (2007).

The layered type salt rock is composed of alteration of grey, clay mineral-rich layers and white clay mineral-free halite layers. The layer boundaries are not sharp, transitional, the gray and white parts are intercalated. The texture of layered salt rock type differs from of the massive one in grain size (1-1.3 mm in average), and the grain size distribution is fairly consistent (mm in magnitude). Grains are typically subhedral, grain boundaries are usually straightened into polygonal shape. Most of the grain boundaries in this type of salt rock accommodate fluid inclusions. A typical feature is the 120° grain boundary triple junction (Fig. 9/B). The primary fabrics, such as chevron crystals are missing. This texture tends to have a polygonal mosaic structure defined by Hardie et al. (1985).

Both salt rocks types are monomineralic (halite > 90%) but the layered type contains relatively less clay mineral.

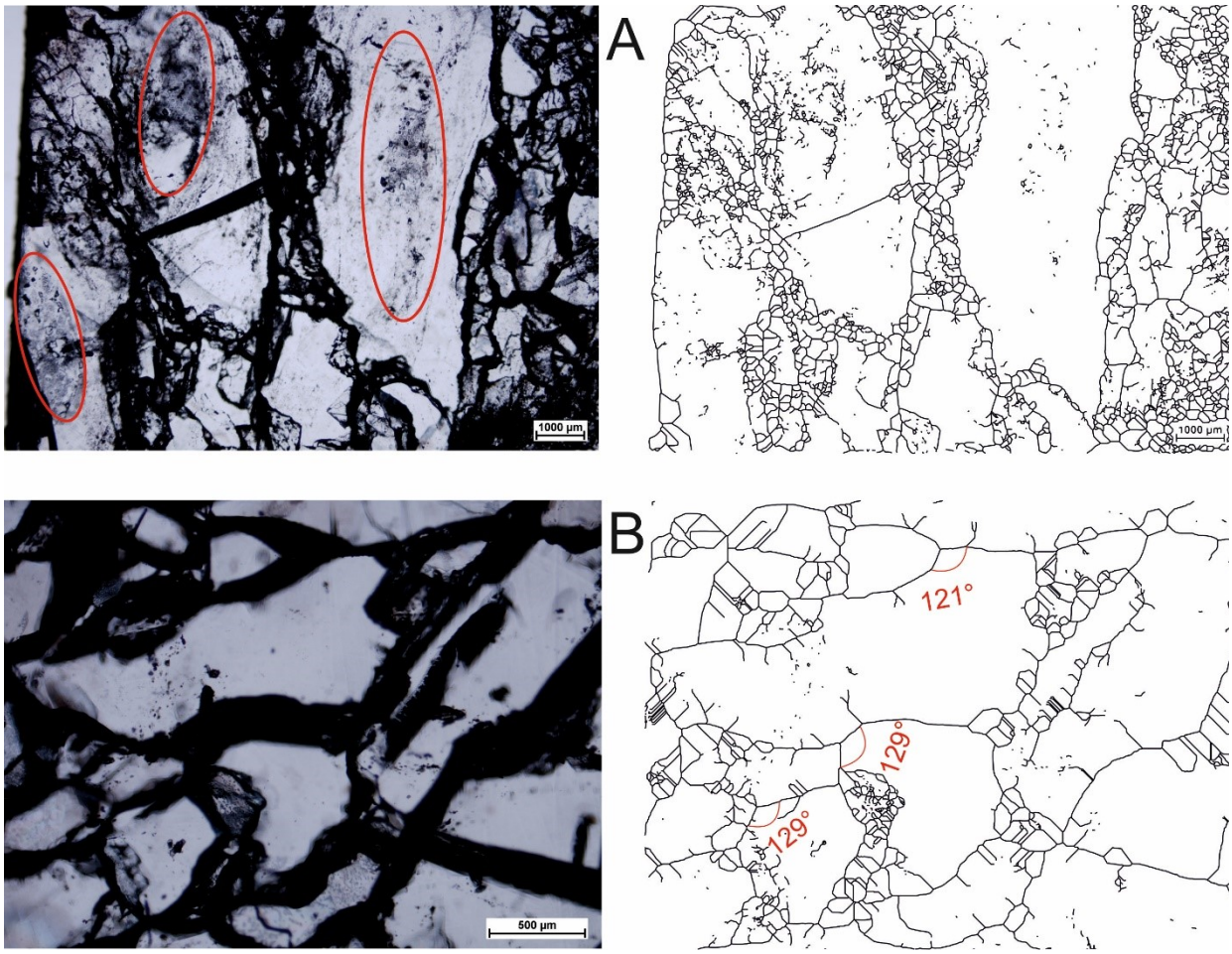

Figure 9. Representative photomicrographs on the two salt rock types and the drawn grain boundaries visualized by image editor software. A: Elongated halite crystals are placed in a submillimeter sized crystal mash in massive type salt. Large halite grains have fluid inclusion rich cores (red circle). Sample: PAT17-4, transmitted light, 1N. B: Grainsize distribution is more consistent in layered type salt rock, compared to the massive. ~ 120° joints are common indicating mosaic structure. Lack of primary fluid inclusions is characteristic for this type of salt rock. Sample: PAE17-3, transmitted light, 1N.

According to the microstructural observations, samples from the massive salt show fabric made of 1 mm large equigranular subhedral grains with notable amount of porphyroclasts (5 -10 mm). Large amount of subgrains are can be recognized in the porphyroclasts, which are also interlobated by grain boundaries. The bands are more clearly developed in grains that are adjacent to the large subgrain-rich grains. Porphyroclasts are surrounded by sub-euhedral grains (~ 1 mm), which are usually subgrain-poor or seldom subgrain-free. There is an exceptional sample (PAT17-4) from the massive-type salt rock which is high abundant in porphyroclasts comprising 10-15 mm sized grains. These grains, in turn are occasionally rich in primary fluid inclusions.

In the layered-type salt, there are less porphyroclasts, but subgrain rich grains and subgrain poor/free grains are also present. The fluids at the boundaries influence the outline of grain boundaries (Fig. 10).

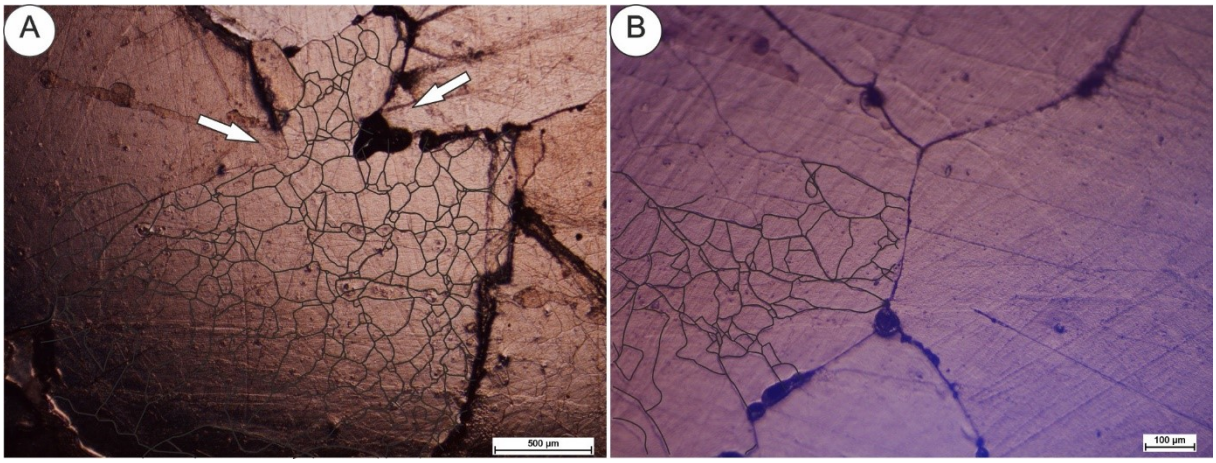

Figure 10. Surface of the irradiated salt rock sample. A: Subgrain-rich grain is consumed by subgrain free grain as indicated by white arrows. Subgrain structure is outlined. Sample: PA40-PH, reflected light. B: Subgrain-rich grain (on the left) in contact with three subgrain-free grains. The network of subgrains is partially outlined. Sample: PAT17-3, reflected light.

Besides halite, many mineral species can be observed as accessories. The second most abundant mineral of the salt rock is the anisotropic, tabular **anhydrite**. The size of the anhydrite crystals is usually between 100-500 µm and they occur as rectangular, tabular plates (Fig. 11/A-B) or rarely has so called "axe-like" forms. Capillaries, perpendicular to the longer edges, are typical features of the anhydrites and presumably filled with fluids. However, due to the small diameter (< 1 µm) capillaries could not be identified with Raman spectroscopy. Usually the anhydrite crystals are contaminated by dark brownish material or with opaque spots which are supposing tiny pyrite crystals.

The second most frequent accessory mineral is the 50-100 µm sized rhombohedral **dolomite**. Crystal color ranges from translucent, white to slightly orange. The dolomites sometimes form aggregates dimension of 400-500 µm size. Dark, or opaque core and the presence of cleavage planes without roundness are typical characters of Praid dolomites (Fig. 11/C). Besides anhydrite, and dolomite, subordinate amount of transparent **gypsum** is also presented, appearing as acicular shaped crystals.

Pore and space filling minerals occur in wide range of size from submicron to 600 µm furthermore silicates form rock fragments. The most abundant detrital mineral is **quartz**, which

is usually rounded, having of fluid inclusions. Besides this type, there are euhedral quartz grains/fragments containing silicate melt inclusions (Fig. 11/D). Large translucent **mica** flakes, supposing muscovites, are also present in part of the samples. Another silicate is the feldspar (100-200 µm), and some non-identified, probably weathered silicate minerals are also present among the accessories.

Clay mineral rich nodules are typically presented in both salt rock types showing various compositions (Fig. 11/E). Various other **rock fragments** and aggregates (Fig. 11/F) found in the Praid salt rocks consist of silicates phases: garnet, quartz and feldspar are common constituents of them in the massive salt type.

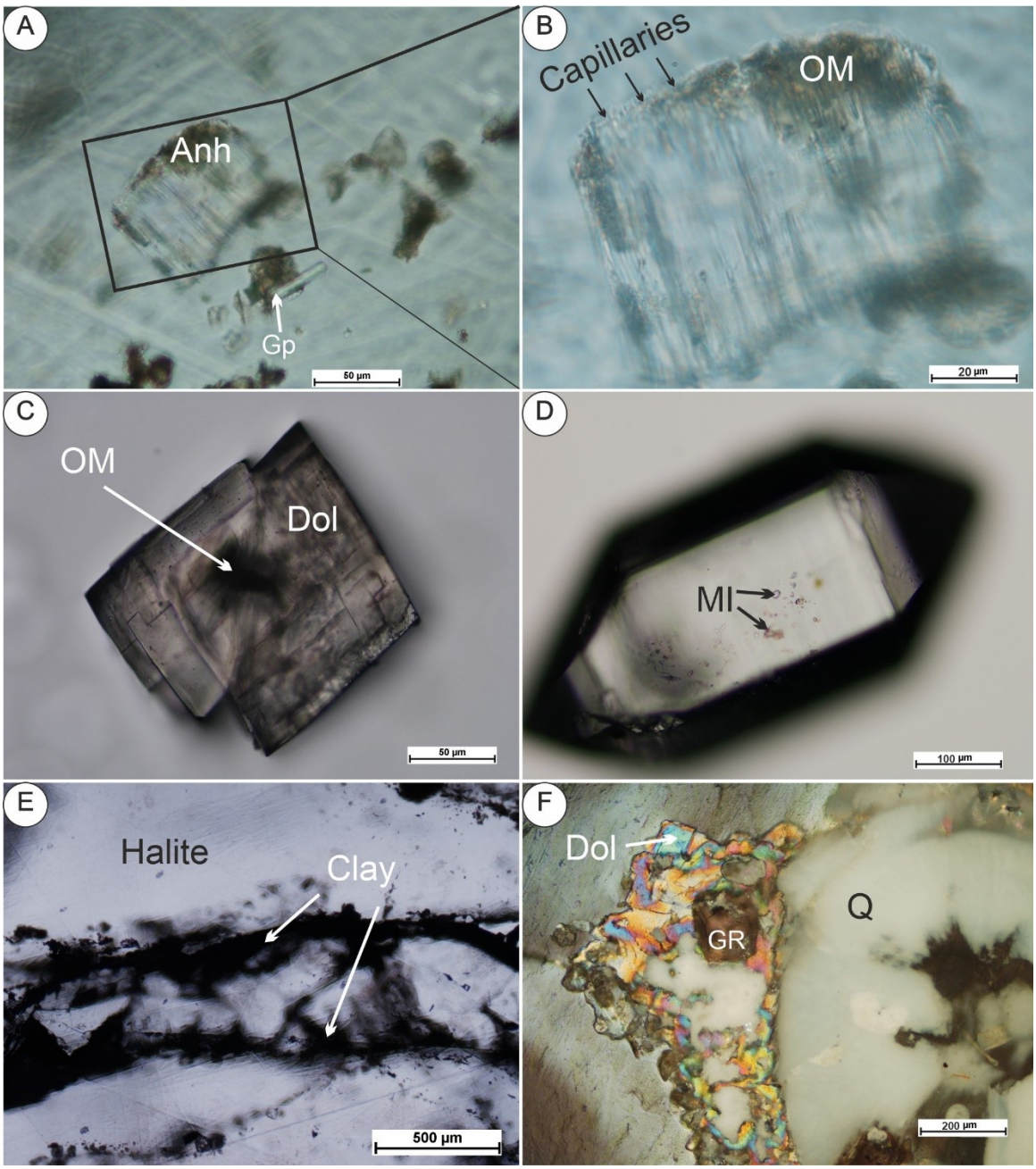

Figure 11. Accessories of the Praid salt rock from both types. A: Typical appearance of anhydrite and gypsum in halite. Gypsum occurs as needle shaped crystals. Sample: PAT17-3, transmitted light 1N. B: Part of A. Note, along anhydrite grain boundaries, abundant organic matter and capillaries filled by fluids can be observed. C: Rhombohedral dolomite, having dark, organic rich core. Cleavage planes could be also seen. Sample: PAT17-3, transmitted light, 1N. D: Idiomorphic quartz containing silicate melt inclusions. Sample: PA40-PH, transmitted light, 1N. E: Clay minerals as filled materials along grain boundaries of halite. Sample: PAT17-4, transmitted light, 1N. F: Metamorphic rock fragment containing quartz and garnet. Euhedral dolomite (such as C, precipitated to the edge of the aggregate. Sample: PAE17-5, transmitted light, +N. Abbreviations: Anh: Anhydrite, Gp: Gypsum, Dol: Dolomite, OM: Organic matter, MI: Melt inclusion, Q: Quartz, GR: Garnet.

4.1.1. Fluid inclusion petrography

The Praid salt rock is very abundant in fluid inclusions as it is usual in natural halites. Two types of fluid inclusions can be distinguished among the samples: P-type (primary) and S-type (secondary).

4.1.2.1. P-type fluid inclusions

Fluid inclusion assemblages, occurring along growth zones of halite crystals, having cubic (negative crystal) shape, containing only liquid phase in room temperature. The size of individual fluid inclusions ranges between 10-100 µm. Based on the classification of Roedder (1984) and (Kerkhof and Hein, 2001), these fluid inclusions are defined as primary (P-type) fluid inclusions (Fig. 12/A,B). Anhedral shape fluid inclusions can be observed in similar position (growth zones) which assemblage is composed of not only translucent liquid phase inclusions, but also dark organic material. Latter fluid inclusions can be regarded as organic compound-rich, P2-sub-type one. Typically, this P2 fluid inclusions are larger than the clear (organic-free) ones, their average size ranges between 2-300 µm (Fig. 12/C,D).

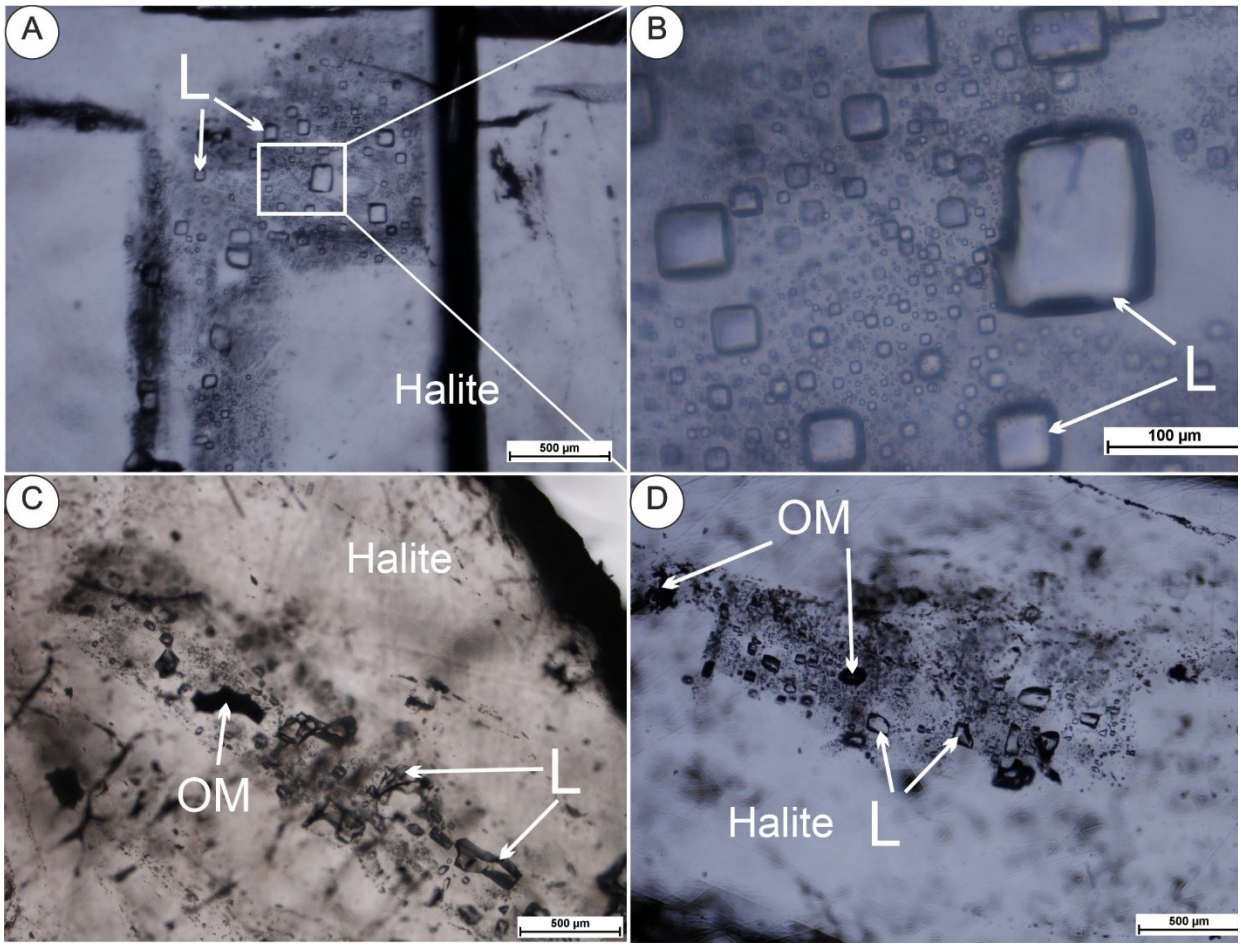

Figure 12. Photomicrographs are showing the primary fluid inclusion petrographic characteristics of the Praid salt rocks. A: Primary fluid inclusions in halite showing negative crystal shape and (only) liquid phase at room temperature. Sample: PAT17-4, transmitted light, 1N. B: Part of A. C: P2-type fluid inclusions in halite having irregular shape. Additionally, they contain dark, organic matter Sample: PAT17-2, transmitted light, 1N D: P2-type fluid inclusions containing organic material resulting irregular size and shape. Sample: PAT17-4 , transmitted light, 1N. L: liquid phase, OM: organic material.

4.1.2.2. S-type fluid inclusions

Secondary fluid inclusions (S-type) can usually be found in the salt rocks of various shapes and distribution. Four different S-type fluid inclusion can be distinguished. The common features shared by S-type FIs are the following: they show intergranular distribution, in both massive and layered types, cross the grain boundaries, fill the space between crystals . They are of various in shape, size, and number of phases at room temperature.

The fluid inclusions that consistently appear in cubic shape and only contain single vapor phase at room temperature are referred as **S1** type. This type of inclusions forms trails across grain

boundaries, and appears along healed fractures. The size of the S1-type fluid inclusions is varying between 10-40 μm. They are very common in both salt rock types (Fig. 13/F).

Fluid inclusion with irregular shape and two phases (vapor or vapor+liquid) occurring at cleavages face of halite are defined as **S2** type (Fig. 13/E). This type of inclusions displays very variable shape in their assemblages: from elongated to rounded ones. The size of the inclusions varies from 5 to 100 μm. The phase ratio (vapor/liquid) is variable, necking down and leakage are often observed.

Fluid inclusions having vermicular-, or amoebae-like shape, containing possibly gas phase are defined as **S3** type (Fig. 13/D). They are characterized by large length/width ratio (~20-30) and form a network so that, it is difficult to distinguish between the connected and the disconnected types of inclusions.

Dark elongated tubular shapes gas-bearing inclusions forming trails are treated as **S4** type secondary fluid inclusions. They occur in muddy halite nearby organic matter. The size of the S4-type fluid inclusions is varying between 10-60 μm (Fig. 13/B).

Beside the well-defined secondary inclusions, mentioned above, there are appearances of fluids at grain boundaries. The shapes of these inter-grain fluid inclusions are often spherical, or resemble thin capillaries. The size of them are smaller than 10 μm but they could even be in the submicron size range (Fig. 13/C).

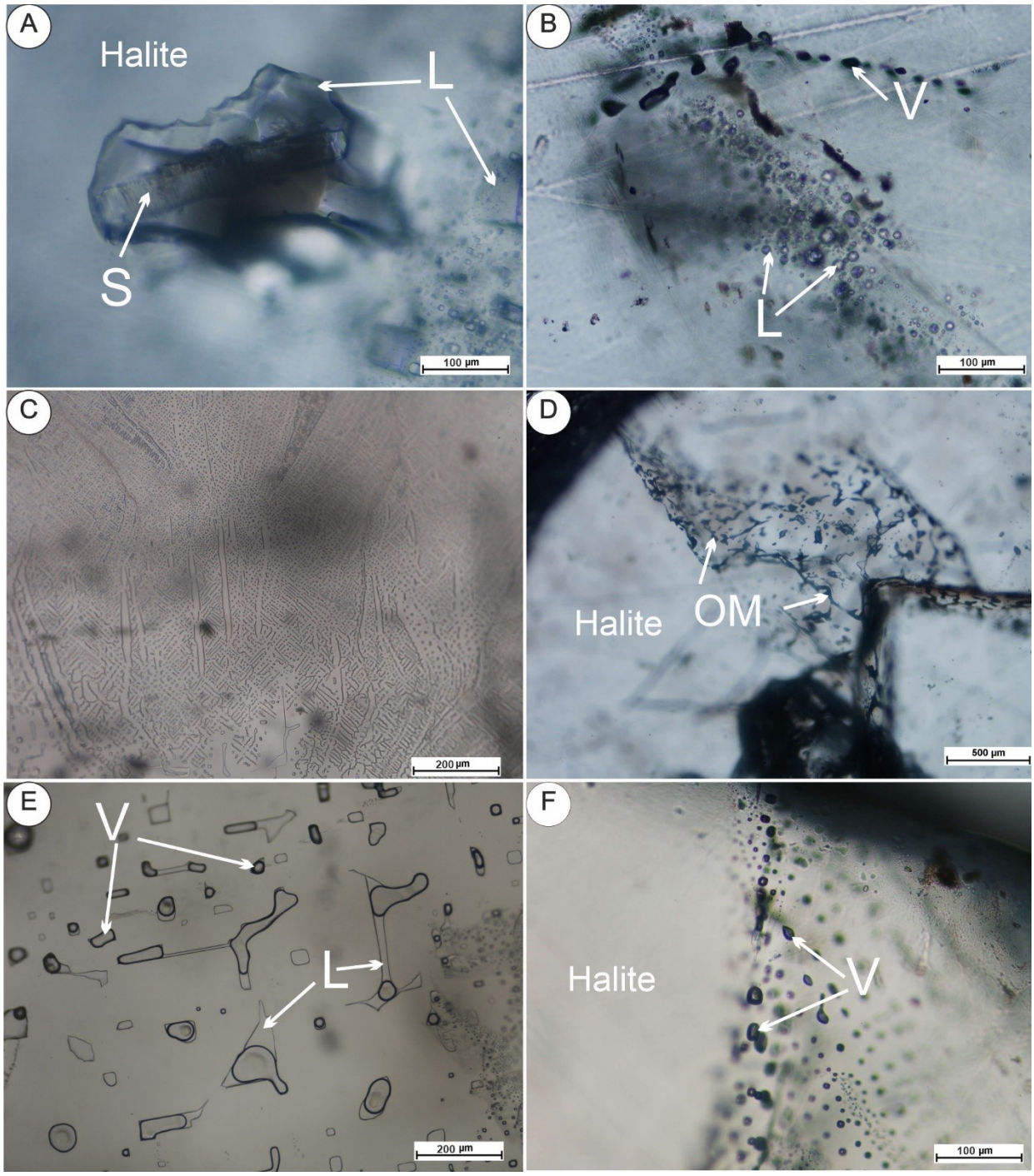

Figure 13. Photomicrographs are showing the S-type fluid inclusion petrographic characteristics of the Praid salt rocks. A: Fluid inclusion captured tabular anhydrite crystal (S) at a primary FIA. Sample: PAT17-4, transmitted light, 1N. B: Gaseous dark secondary fluid inclusion array in the vicinity of a primary FIA. Sample: PAT17-4, transmitted light, 1N. C: Fluid film at a grain boundary. Sample: PAT17-2, transmitted light, 1N. D: Amoebae-like secondary fluid inclusions forming a net. Sample: PAE17-3, transmitted light, 1N. E: S1 type irregular shaped, two-phase fluid inclusions. Sample: PAT17-2, transmitted light, 1N F: Rounded cubic shaped, gas bearing fluid inclusion trail in halite. Sample: PAT17-1, transmitted light, 1N. Abbreviations: FI: fluid inclusion, S: solid, OM: organic matter, L: liquid V: vapor phases.

4.2. Results of microthermometry

In the case of Praid salt rock, microthermometry studies were carried out to determine the eutectic (first melting - T_e) and homogenization temperatures (bubble nucleation - T_h) of the P-type fluid inclusions in halite.

Fluid inclusions, originated from seawater, are expected to have homogenization temperature near to the surface temperature (< 50 °C) (Roedder, 1984). The homogenization temperature of Praid samples ranges between 10 and 34°C (Fig. 14, Table 2). There was not any significant difference in T_h values between the two types massive and layered rock salt.

Metastable behavior was observed in lower temperature. At first freezing (to -100 °C), the frozen inclusions contain glassy tan-colored solids. During heating (to -50 °C), the solid FIs had started to darken to opaque. However, the smaller inclusions contain submicron size clear solid, these remained bright. After the second cooling (to – 100 °C) and heating, the T_e (eutectic temperature) were recorded and ranged from -56 to -43°C.

However, the salinity of seawater could be determined by the temperature of final melting of ice (T_m^{ice}), in the case of Praid samples, the temperatures of this last phase transition are covered a wide range and it was usually unclear. After the melting of the inclusions they were get distorted and lost their original, cubic shape. The results of microthermometry is summarized in Table 2 and Fig. 14.

Table 2. Microthermometry results of Praid salt rocks. Th = homogenization temperature, Te = eutectic temperature, T_m^{ice} = last/ice melting temperature

Samples	Th (°C)	Te (°C)	Tm^{ice} (°C)
N = 35	10 30	-55 -47	-10 -2

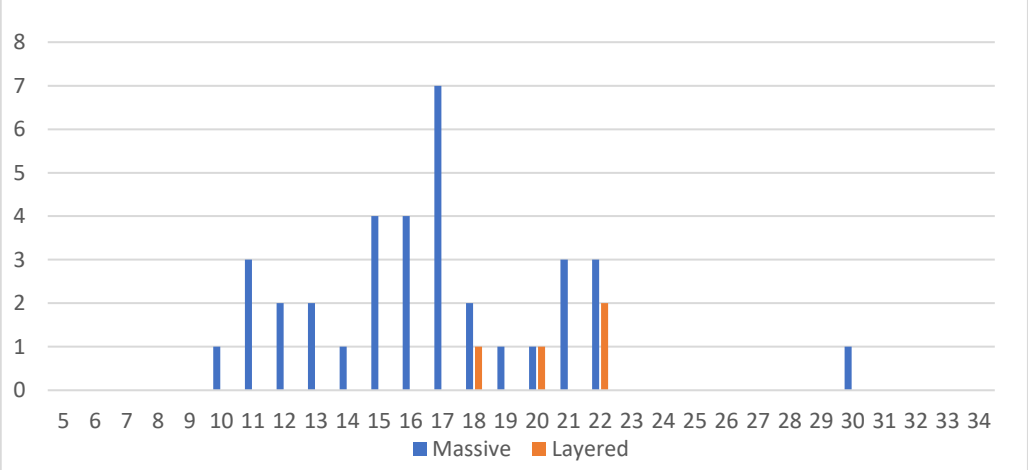

Figure 14. Histogram of the homogenization temperature values on the measured primary fluid inclusions from Praid. X and Y axis represent the temperature (°C) and frequency of homogenizations Th (L+V) →L, (°C), respectively.

4.3. Results of Raman spectroscopy

4.3.1 Identification of solid phases

Solid components of the insoluble residue obtained from both types of salt rocks were identified based on their characteristic Raman spectrum. Accordingly the following phases were identified: anhydrite (1018 cm^{-1}, 1130 cm^{-1}) (Fig. 15), dolomite (291 cm^{-1}, 725 cm^{-1}, 1096 cm^{-1}) (Fig. 15), quartz (128 cm^{-1}, 206 cm^{-1}, 355 cm^{-1}, 464 cm^{-1}) (Fig. 15), garnet (347 cm^{-1}, 499 cm^{-1}, 554 cm^{-1}, 913 cm^{-1}) and β-carotene (1157 cm^{-1}, 1522 cm^{-1}). This latter was identified from grains (mainly dolomite) which were orange in color.

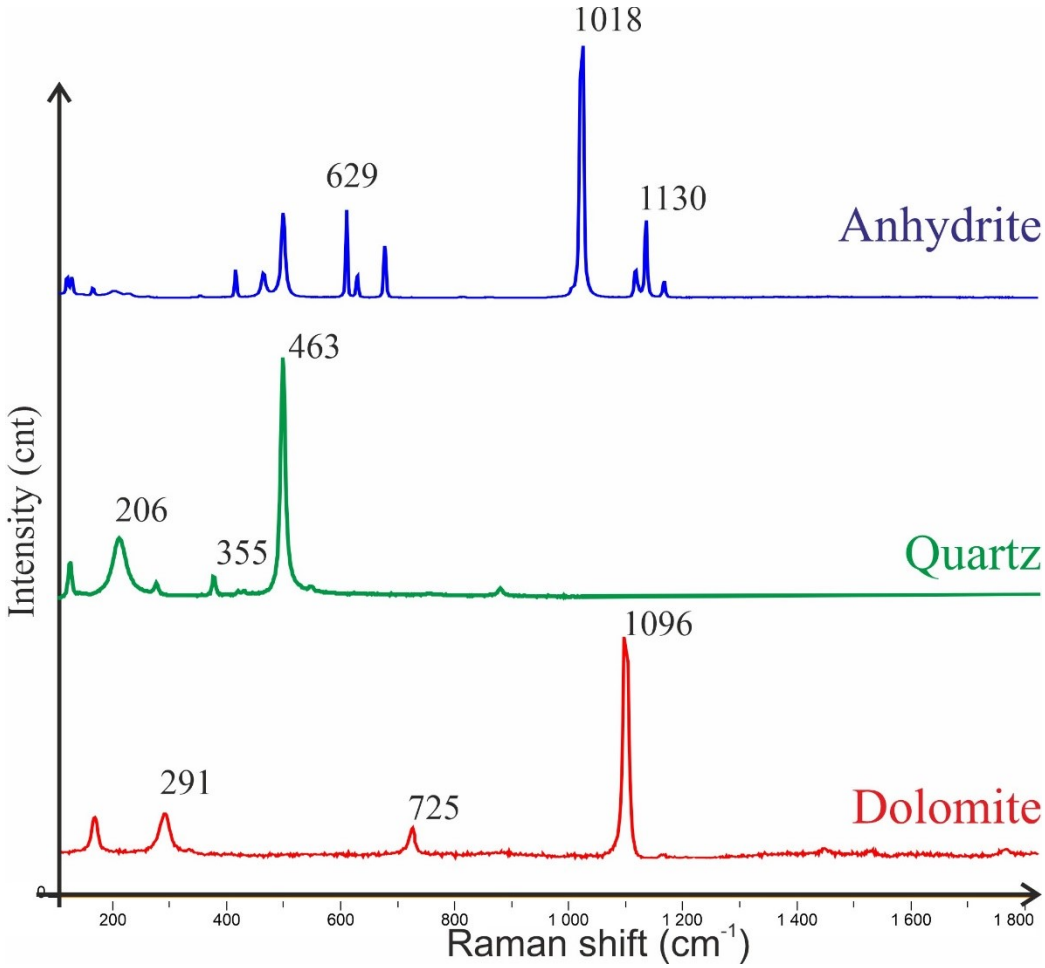

Figure 15. Characteristic Raman spectra of common accessory minerals of Praid salt rocks.

The β-carotene was adhered to the surface of washed minerals (Fig. 16).

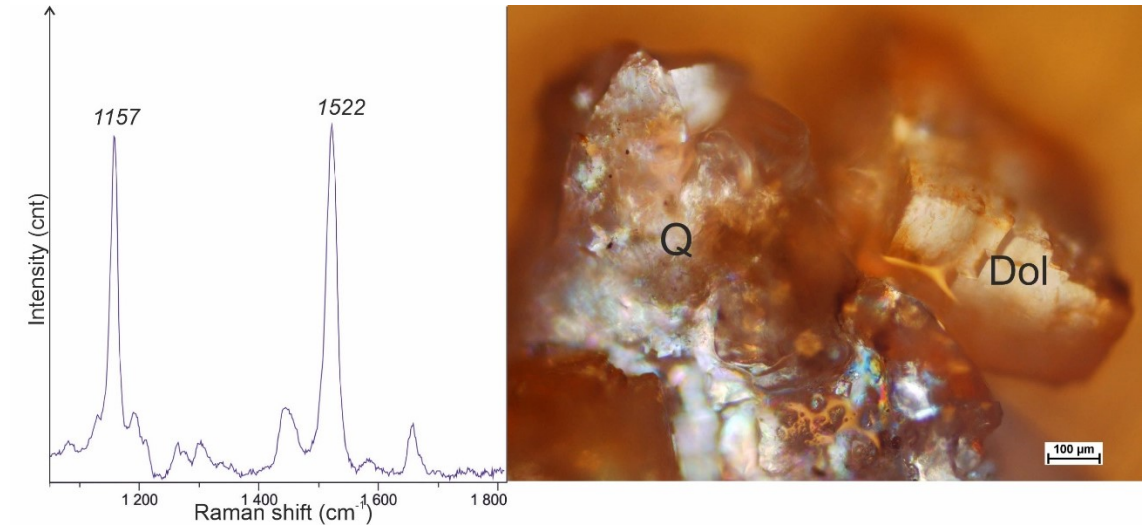

Figure 16. On the left characteristic Raman spectra of β-carotene can be seen. On the right, a mineral aggregate can be seen. Orange color carotene is attached to the aggregate. Photo was taken under stereomicroscope (Sample: PAE17-3).

4.3.2. Vapor-bearing fluid inclusions

Secondary fluid inclusions were measured by Raman spectroscopy from both types of salt rocks. Despite the long accumulation time of the Raman spectrum (60-180 sec), very weak signals were collected, therefore the spectra could only be characterized with small signal/noise ratio and the Raman bands had low intensity. In the case of S1-type FIs (Fig. 13/F), only the larger (> 30 µm) FIs provided valuable signals. In this FIA, N_2 (2333 cm^{-1}) and in sometimes CH_4 (2918 cm^{-1}) and CO_2 (1287, 1388 cm^{-1}) were identified (Fig. 17, Table 3). Nitrogen entrapped in the FIs could be distinguished from the air-contained N_2. The vapor phase in a two phase (liquid and vapor) FIs (Fig. 12/E) could not be measured because the bubble was moved away from the laser beam. Merely H_2O could be identified. Interpretable signal from the S3 type FIA (Fig. 13/D) was not possible to acquire.

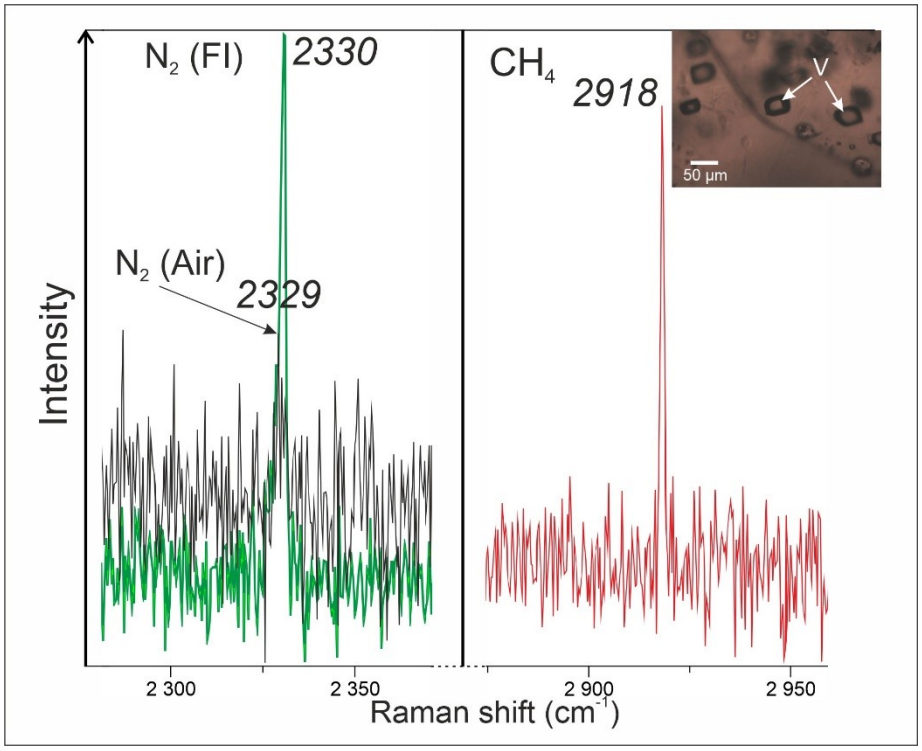

Figure 17. Representative Raman spectra of phases within studied secondary vapor phase fluid inclusion (photomicrograph at the right top) at room temperature. The peak of N_2 at 2329 cm^{-1} having of atmospheric origin, in contrast to the peak at 2330 cm^{-1}. Abbreviations: FI: fluid inclusion V: vapor phase fluid inclusion.

Table 3. Composition of S2-type, vapor phase fluid inclusions expressed in mol%. Calculation is based on (Dubessy et al., 1989).

Type	Code	CO_2 (mol%)	CH_4 (mol%)	N_2(mol%)
Layered	PA40-4-S1	0.0	0.0	100.0
	PA40-4-S2	0.0	0.0	100.0
	PA40-4-S3	0.0	3.2	96.8
	PA40-4-S4	0.0	2.1	97.9
	PA40-4-S5	0.0	0.0	100.0
	PA40-4-S6	0.0	23.4	76.6
	PA40-4-S7	1.0	1.2	97.7
	PAE17-3-S1	0.0	0.0	100.0
	PAE17-3-S4	0.0	1.1	98.9
Massive	PAT17-4-S1	0.0	0.0	100.0
	PAT17-4-S2	0.0	0.0	100.0
	PAT17-4-S3	12.2	1.5	86.3
	PAT19-7-S1	0.0	0.0	100.0
	PAT19-7-S2	0.0	0.0	100.0
	PAT19-7-S3	0.0	0.0	100.0
	PAT17-A-S2	1.4	5.7	92.9
	PAT17-A-S3	23.6	7.5	68.9
	PAT17-B-S1	0.0	0.0	100.0
	PAT17-B-S2	4.3	0.0	95.7
	PAT17-C-S1	0.0	0.0	100.0
	PAT17-4_1B	0.0	4.5	95.5

4.3.3. Raman spectroscopy coupled with microthermometry

The identification of phases in complex chloride brines, such as the topic of this thesis, is very difficult by using alone microthermometry, but the combination of Linkam stage with Raman spectroscopy is appropriate to identify salt hydrates (Dubessy et al., 1982; Baumgartner and Bakker, 2010; Uriarte et al., 2015). At room temperatures, H_2O has a broad peak from 2800 to 4000 cm^{-1}, which covers the hydrate peaks. At low temperature, the solid phase ice and hydrates have distinct spectra therefore a quantitative analysis of major components possible. Halite does not have any signal: in this case it is an excellent host. The results of the cryogenic Raman measurements are shown in Table 4. The Raman spectrum were obtained in the region of stretching frequencies (3000-3600 cm^{-1}). Peaks assigned to cubic ice (Ic) appear at 3092 cm^{-1} and 3536 cm^{-1}, respectively.

Besides the characteristic Raman bands of cubic ice (Ic) several salt hydrates phases were identified. Hydrohalite is ubiquitous in the fluid inclusions. Shoulders of the main bands of hydrohalite are located at 3404, 3433 cm^{-1} and 3538 cm^{-1}. To summarize the results, the presence of Na-Ca-Mg-hydrates was likely found. The collected spectra show homogeneity, except one deviation, the 3510 cm^{-1} peak, which is a strong indication for Mg-hydrate, was identified just in a few cases.

Table 4. Raman peak positions of solid state primary fluid inclusions of Praid salt rocks expressed in relative wavenumbers (Δv= cm^{-1}).

Type	Codes	T (°C)	H_2O-peaks (cm^{-1})	Peak positions related to bending modes (cm^{-1})	Peak positions related to stretching modes (cm^{-1})
Massive	PAT17-4_P1	-190	3084	1663	3210, 3322, 3354, 3403, 3422, 3537
	PAT17-4_P5	-190	3082	1639, 1667	3210, 3404, 3422, 3538,
	PAT17-4_P7	-190	3082		3207, 3404, 3422, 3434, 3538
	PAT17-4_B_P5	-190	3087	1660	3213, 3323, 3404, 3422, 3538
	PAT17-4_B_P6	-190	3087		3213, 3324, 3404, 3422, 3538
	PAT17-4_C_P1	-190	3082		3207, 3402, 3424, 3539
	PAT17-4_C_P6	-190	3086		3211, 3324, 3404, 3422, 3433, 3512, 3536
	PAT17-3_P1	-190	3089		3214, 3326, 3404, 3422, 3433, 3537
	PAT17_P2	-180	3090	1645, 1647, 1664, 1666	3405, 3422, 3436, 3538
	PAT17_P3	-180	-	1648.73, 1648.26, 1664, 1667	3405, 3422, 3436, 3537
	PAT17_P4	-180	3090	1645. 1649, 1665	3405.53, 3422, 3435, 3513, 3538.
	PAT17_P5	-180	3091	1646, 1647, 1664, 1667	3406, 3422, 3436, 3513, 3538
	PAT17_P6	-180	3091	1646, 1665, 1668	3323, 3405, 3422, 3436, 3513, 3538
	PAT17_P7	-180	3091	1645, 1649, 1664, 1667,	3405, 3422, 3437, 3538
	PAT17_P8	-180		1648, 1665, 1668	3405, 3422, 3435.4, 3538
Layered	PAE17-3_P1_i	-175	3096		3406, 3422. 3434, 3539
	PAE17-3_P1_j	-175	3091		3405, 3422, 3435, 3538
	PAE17-3_P1_k	-175	3094	1666	3406, 3422, 3436, 3539
	PAE17-3_P1_l	-175	3090		3406, 3422, 3435, 3538
	PAE17-3_P1_m	-175	3094		3405, 3422, 3434, 3538
	PAE17-3_P1_n	-175	3093		3405, 3423, 3436, 3539
	PA40-P1	-175	3091		3404.55, 3422, 3436, 3538

4.4. Stable isotope studies

Stable isotope studies were carried out only on the massive type salt rock samples, due to the vis major pandemic situation.

4.4.1. S and O stable isotopes in anhydrite

The isotopic composition of sulfates exhibits a narrow range both in $\delta^{34}S$ (from +20.4 ‰ to +22.4 ‰) and in $\delta^{18}O$ (from +12.9 ‰ to +14.5 ‰) (Table 5).

Table 5. Isotopic composition of sulfate in anhydrite from Praid massive salt rock.

Code	$\delta^{34}S$ Sample/VCDT	$\delta^{18}O$ sample/VSMOW
PAT17_4_E	**22.4**	**12.9**
PAT17_5_A	**20.8**	**13.4**
PAT17_5_B	**20.9**	**14.0**
PAT17_5_C	**20.4**	**14.5**
PAT17_5_D	**20.8**	**13.7**
PAT17_5_E	**20.4**	**13.7**
PAT17_3_A	**20.7**	**13.3**
PAT17_3_B	**21.1**	**13.1**

4.4.2. C and O stable isotopes in dolomite

The isotopic composition of CO_3 in dolomite is quite uniform. The determined of $\delta^{13}C$ assign an interval from -7.07 ‰ to -4.55 ‰, whereas the $\delta^{18}O$ values fall between -9 ‰ and -8.3 ‰ (Table 6).

Table 6. Isotopic composition of carbonate in dolomites from Praid massive salt rock.

Code	$\delta^{13}C$ sample/VPDB	$\delta^{18}O$ sample/VPDB
PAT19_5_A	**-5.40**	**-8.6**
PAT19_5_B	**-4.78**	**-8.8**
PAT19_5_C	**-5.21**	**-8.4**
PAT19_5_D	**-5.65**	**-8.9**
PAT19_5_E	**-4.73**	**-8.9**
PAT19_5_F	**-4.55**	**-9.0**
PAT19_5_G	**-5.68**	**-8.6**
PAT19_5_H	**-4.98**	**-8.9**
PAT17_1_A	**-5.15**	**-8.3**
PAT17_3_A	**-7.07**	**-9.0**

4.4.3. O and H stable isotopes in primary (P-type) fluid inclusions

Analyses of halite grains from massive-type salt rock yielded strongly negative values. The inclusion-hosted H_2O, extracted from the FIs, gives ranges from -10 to -7 ‰ for $\delta^{18}O$ and -70 to -65‰ for $\delta^{2}H$, respectively (Table 7). Compositions of evaporated waters are reported in a $\delta^{2}H$–$\delta^{18}O$ space along with the Global Meteoric Water Line (GMWL) (Craig, 1961) (Fig. 18).

Table 7. Isotopic composition of H_2O in fluid inclusions in halite from Praid massive salt rock.

Code	δ^2Hsample/V-SMOW	δ^{18}O sample/V-SMOW
PAT17-4_1	-74.17	-8.85
PAT17-4_2	-74.42	-7.88
PAT17-4_3	-80.47	-10.86
PAT17-4_4	-88.74	-13.85
PAT17-4_5b	-87.62	-13.97
PAT19-1_2	-78.87	-13.62
PAT19-1_3	-81.85	-14.79
PAT19-3_1	-82.02	-15.73
PAT19-3_2	-85.06	-16.67
PAT19-3_3	-85.94	-16.91
PAT19-3_4	-83.85	-13.63
PAT19-4_1	-87.08	-11.41
PAT19-4_2	-90.26	-13.65
PAT19-5_2	-85.01	-12.11
PAT19-5_3	-86.61	-10.80
PAT19-5_4	-91.5	-17.85
PAT19-5_5	-76.41	-8.38
PAT19-8_2	-81.37	-9.145
PAT19-8_3	-87.91	-14.77
PAT19-8_4	-89.06	-15.82

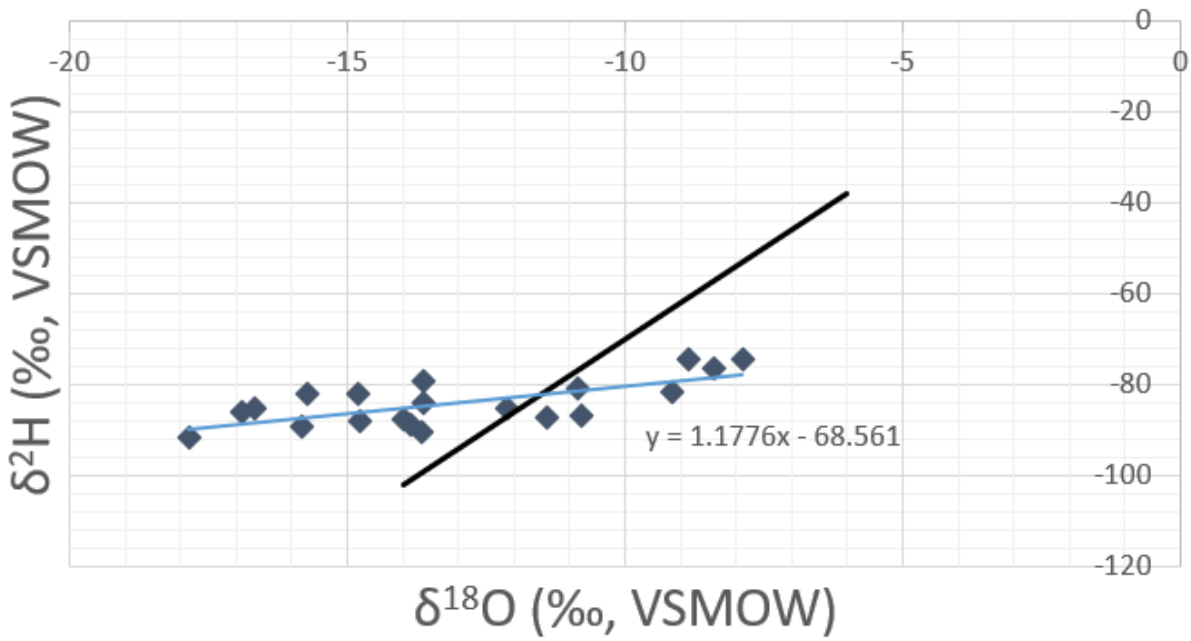

Figure 18. Measured $\delta^{18}O$ and $\delta^{2}H$ values from fluid inclusion plotted with Global Meteoric Waterline (black). The equation of the line is: y=1.18*x-68.561.

4.5. Results of electron backscatter diffraction (EBSD) mapping

EBSD mapping was performed both in massive and layered salt samples to shed light on the microstructure of the Praid salt rocks.

In the massive salt rock type (2 samples), in which the primary FIs are abundant, substructure rich porphyroclasts were observed. The porphyroclasts contain subgrains with dominant misorientation angle <2°, a few boundaries between 2° and 5°and, very rarely, with 5-10°.

In the case of layered salt (1 sample), the subgrain rich porphyroclasts were surrounded by subgrain-poor grains were shown. Only a few small (< 1 mm) grains display the lack of substructure.

The profiles, provided on the EBSD maps, of both types of salt rock samples (massive and layered) indicate that the degree of misorientation of subgrain boundaries increases from the core of the grain to the edge. The crystallographic preferred orientation (CPO) of the crystals is closely rare (Fig. 19).

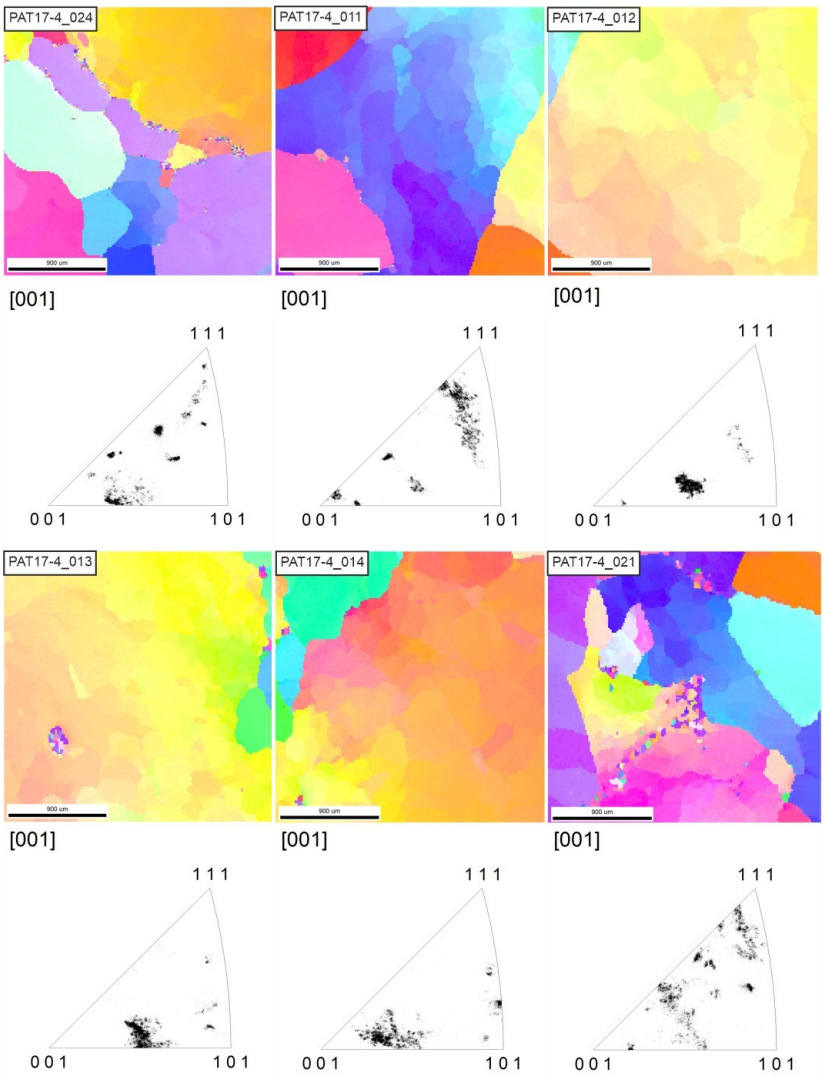

Figure 19. Electron backscattered diffraction mapping of massive-type salt rock from Praid. The corresponding inverse pole Figures (IPFs) inferred from the EBSD maps (each map has its IPF below). Different colors indicate different crystallographic orientation. Shades of the colors indicate internal misorientation in the grain itself. Small colorful patches (e.g. in PAT17-4_021) are cracks on the surface, which were indexed incorrectly.

The average subgrain size slightly differs in the two observed types of salt (Table 8). The massive salt is characterized by 80 µm subgrain size in average, whereas the layered type is characterized by 108 µm subgrain size in average, but with a larger variance. The largest subgrain size (124 µm) was observed in the massive type sample, which is rich in porphyroclasts containing primary fluid inclusions.

Table 8. Quantitative analyses of microstructures performed on halite crystal subgrains.

Type	Code	Average subgrain diameter (µm)
Layered salt	PA-40_001	143.21
	PA-40_002	132.64
	PA-40_003	172.77
	PA-40_004	100.14
	PA-40_005	48.26
	PA-40_006	92.09
	PA-40_007	66.95
Massive salt with its typical cm size, elongated chevron crystals	PAT17-4_011	125.70
	PAT17-4_012	135.39
	PAT17-4_013	106.81
	PAT17-4_014	119.99
	PAT17-4_021	101.27
	PAT17-4_022	159.15
	PAT17-4_023	125.41
Massive salt with single white layer	PAT19-7_001	99.03
	PAT19-7_002	67.07
	PAT19-7_003	81.56
	PAT19-7_004	83.28
	PAT19-7_005	76.79
	PAT19-7_006	93.97
	PAT19-7_007	70.52
	PAT19-7_008	77.54
	PAT19-7_009	70.81

4.6. Gamma irradiated measurements

Gamma irradiation was carried out to study microstructure of the salt rocks as complementary method EBSD mapping. Both set of irradiations, higher (4 MGy) and lower (1,5 MGy) dose

resulted in the same brownish color for the samples. The obtained subgrain size statistics is displayed in Table 9. The mean subgrain size of layered and massive salt are about 113 µm and 81 µm respectively.

Table 9. Average subgrain size diameter of Praid salt rocks based on calculations on gamma irradiated samples. The diagram shows that the subgrain size measurement obtained from the two techniques are overlap.

Type	Code	Average subgrain diameter (µm)
Layered salt	PA40_PH_1	129.61
	PA40_PH_2	134.44
	PA40_PH_3	125.82
	PA40_PH_4	128.99
	PA40_PH_5	122.88
Massive salt	PAT17-3_1	68.34
	PAT17-3_2	94.40
	PAT17-3_3	89.28

5. Discussion

5.1. Petrographic evidences for primary features

5.1.1. Genetic interpretation of macroscopic- and microscopic features of the salt rocks

Distinguishing syndepositional (primary) features from secondary features of a salt rock is a prerequisite step of any study on ancient evaporites (Hardie et al., 1985; Lowenstein and Hardie, 1985; Warren, 2013; Bąbel and Schreiber, 2014). The textural observations of Praid salt rocks resulted in recognition of at least two types of salt rocks (i.e. massive and layered, Fig. 5), which could have formed under different conditions or environment. From the criteria, established by Hardie et al. (1985), the Praid salt rock has syndepositional, postburial and also ambiguous features. Evidences of the primary texture are almost completely overprinted by the deformation structure related to diapirism (Ciupagea et al., 1970; Krézsek and Bally, 2006). The ultimate textural survivors are the remnants of aligned chevrons halite which are the most prevalent primary texture preserved in ancient halite (Warren, 2016). Chevron signature of the Praid salt rock is characterized by primary fluid inclusion rich cores, representing the paleo seawater in the core of the halite grains (Fig. 9, Fig. 12). This chevron halite may form on the bottom of a sea (Lowenstein and Hardie, 1985; Warren, 2006b). The various types of detrital minerals and relatively large (couple of millimeters) size rock fragments (Fig 11/F) identified in massive salt, also reveal near shore deposition environment. Thus, the chevron remnants of massive salt rock type, possibly formed at shallow water littoral conditions.

However, the chevrons are indicative of shallow depth, it cannot prove for the whole massive salt rock at Praid to formed at near surface conditions. Another possible explanation could be that the massive type salt represents an ancient accumulation of a crystal bed which was mechanically reworked by storm and wave-induced bottom currents or gravity movement in a slope of the sea (e.g. Hardie et al., 1985; Warren, 2016). This tended to happen on the bottoms of ancient perennial brines and lakes that were above wave base.

The layered salt, as opposed to the massive salt rock type, does not have evidence for syndepositional feature. However, halite grains with primary fluid inclusions sporadically can be found in this type of halite, the shape of the host mineral is not chevron-like, rather similar to the other common halite grains (Fig. 9/B). However, the layering structure suggests different depositional conditions from the massive type. The alternation of grey-colored clay rich and more

pure white layers is very striking feature (Fig. 5/B, Fig. 6/B), which is common in 'basinwide evaporite' sediments (Anderson and Dean, 1995; Warren, 2006a).

Considering that Praid is situated at a marginal area of the salt expansion of the BSC (Fig. 4), another assumption is that the massive salt type represents a shallower shoal environment discussed above. In contrast, the layered salt tends to have accumulated far from seashore where the cyclic detrital input became visible in the sedimentary record. Thus, the layered salt rock type could be the 'heteropic facies" of the shallower one. However, at the marginal area of western TB gypsum is also present (Ghergari et al., 1991), which evaporite mineral usually plays the coastal counterpart of the deeper halite facies (Warren, 2006a).

Both of the arguments had to be considered in the frame of wide-spread postsedimentation diapirism. Indeed, the effect of salt tectonic (detailed in point 5.3 below) can cause such a stirring and internal movement, which led to a secondary layered structure (Jackson and Talbot, 1986). This possibility cannot exclude in the lights of significant horizontal salt movements (Krézsek and Bally, 2006) (Fig. 3) in the TB. Unfortunately, the contact of the salt rock types (massive and layered halite) has not been observed, however, it would have been essential in the interpretation of their original relation both in space and time.

It is important to mention, that recently there is no marine-fed system on the Earth, where large amount of halite can form. The interpretations of ancient evaporite texture always originate from the present day evaporites, they are all continental salt pans. Widespread marine evaporites require particular tectonic and/or eustatic conditions to form that are not present on the Earth's Quaternary surface (Warren, 2006b).

5.1.2. Primary fluid inclusions

Detailed microthermometry studies are very rare on the BSC halite, however, some studies have been performed from the Transylvanian salt (Pintea, 2008; Kátai, 2017) and the East-Slovakian Basin (Galamay et al., 2004). The homogenization temperatures (T_h) in this study (both from the massive and the layered type of salt) (10 – 32 °C) fall in the range drawn by other studies from the area (Fig. 20). Notable to mention that the T_h of the Messinian halites (in the Mediterraneum) (Speranza et al., 2013) show also similar temperature values (17 18 °C). The highest T_h can be found in Praid locality, which could be related to the volume change of the primary fluid inclusions. If a fluid inclusion responds through permanent plastic deformation, its volume is increased to decrease the internal overpressure, producing a lower density leading higher

homogenization temperature (Goldstein, 2001). The large scale diapirism indicates strong deformation in the texture of the salt rock resulting in modification in volume of fluid inclusions. The variability of the T_h values suggests the plausibility of reequilibration process during the burial and halokinetic movements. Nevertheless, the T_h from BSC halite shows consistent low values (< 50 °C) and the observed metastability (only liquid phase in room temperature) reveals that the crystallization of halite has taken place in surface conditions.

Eutectic temperature (T_e) data available from Pintea (2008) are slightly differed from the results of this study. Halites from Praid show very low T_e values (-55 - -42 °C) - in accordance with Kátai (2017), - whereas Pintea (2008) from Ocna Dej shows -36 - -18 °C, which reveal significant spatial changes in evaporite geochemistry.

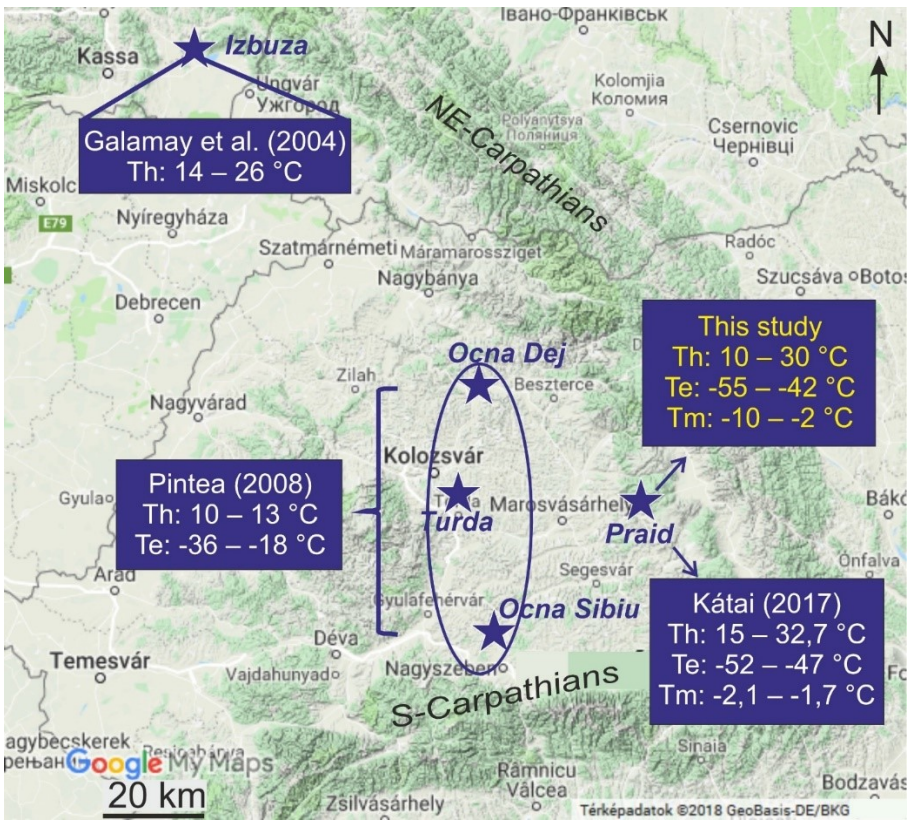

Figure 20. Results of microthermometry of Badenian Salinity Crisis halite primary fluid inclusions. Temperatures for comparison are from E-Slovakian Basin (Galamay et al., 2004), western diapir alignment of TB (Pintea, 2008) and from Praid (Kátai, 2017). The T_h is matching well, while the T_e shows difference between the two diapir alignments of the Transylvanian Basin in chemical composition of the FI. The other microtherometry study on Praid salt rocks (Kátai, 2017) is in a good agreement with this study. Abbreviations: T_h: homogenization temperature, T_e: eutectic temperature, T_m^{ice}: last melting temperature

5.2. Indications of primary features by Raman spectroscopy

5.2.1. Cryogenic measurements of primary fluid inclusions

Natural fluids often belong to the C-O-H-N-S and Na^+-K^+-Ca^{2+}-Mg^{2+}-Cl^- systems. Their composition is challenging to be constrained by microthermometric studies. The phase changes that can be observed in the temperature range -180° to +600 °C are too few and also cannot be interpreted quantitatively for lack of appropriate thermodynamic data (Dubessy et al., 1989). The cryogenic Raman spectroscopy is the most accessible and a very effective method to detect chemical components of a fluid inclusion especially in salt rock-hosted fluid inclusions (Dubessy et al., 1982). The examination of the primary fluid inclusions in solid state by Raman spectroscopy shows complex hydrate composition. The Raman spectra of the inclusions are quite uniform which could mean low variations in composition of mother solutions (Table 4, Fig. 21). This assumption is also supported by the observed narrow range of T_e and T_m^{ice} values during microthermometry (Table 2).

However, results from cryogenic Raman spectroscopy need to be considered with some limitations. The orientation of the hydrates in a single inclusion is disordered, and the intensity ratio of the peaks can change with the orientation (Baumgartner and Bakker, 2010). Other complication is the onlapping peaks of several hydrate species as these are close to the spectral resolution. Furthermore, a hydrate spectrum crystallized from complex brine inclusion can differ from the synthetic ones (Samson and Walker, 2000). Taking the above-mentioned limitations into account, the most reliable signal, besides ice, belongs to the hydrohalite ($NaCl \times 4H_2O$) (Fig. 21).

The Ca^{2+} presumably forms hydrates with different ionic ratio ($CaCl_2 \times 2/4/6\ H_2O$). For example, antarctictite $CaCl_2 \times 6\ H_2O$ or sinjarite which are represented by 1639, 3403-3405, 3414, 3432-3434 cm^{-1} shifts in the samples (Table 4). Though, the 3433 cm^{-1} band of antarctictite and the 3432 cm^{-1} band of hydrohalite can cause overlapping (Samson and Walker, 2000). In this study, the highest intensities belong to the 3422-3424 cm^{-1} band, which coincides with the characteristic peak of hydrohalite (although it is not the highest intensity for the hydrohalite). However, another hydrate can enhance the intensity of this peak position (Dubessy et al., 1982), like $MgCl_2 \times 12H_2O$ (which has a significant peak at 3422 cm^{-1}) and sinjarite ($CaCl_2 \times 2H_2O$) with 3422/23 cm^{-1}.

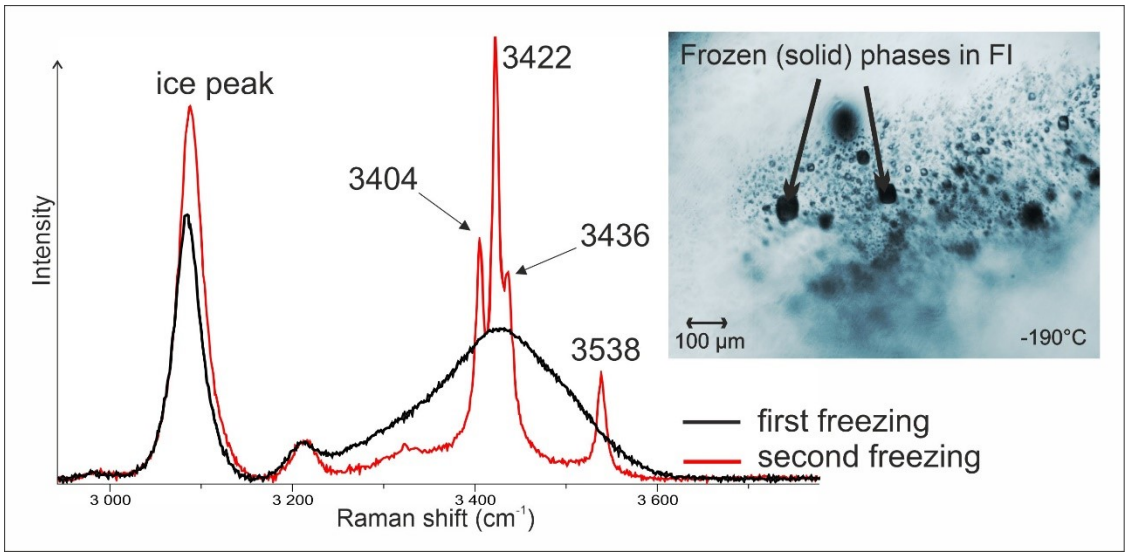

Figure 21. Characteristic Raman spectra of primary-type fluid inclusions on -190 °C after first (black line) and second (red line) freezing in the stretching regions of structural H_2O. Besides, photomicrograph of such primary type fluid inclusion is shown, taken at -190 °C.

Table 10. References of Raman peak positions, in relative wavenumbers (Δv = cm-1) of the various salt hydrates spectra.

References	T(°C)	Hydrohalite	Antarcticite	$CaCl_2$ x 4 H_2O	Sinjarite	$MgCl_2$ x 12 H_2O	$MgCl_2$ x 6 H_2O
		$NaCl_2$ x 4H_2O	$CaCl_2$ x 6 H_2O		$CaCl_2$ x 2 H_2O		
Dubessy et al. (1982)	-175	3432, 3411, 3431	1628, 1644, 1660, 3090, 3242, 3384, 3401, 3407, 3433, 3448, 3513	-	-	3091, 3110, 3328, 3401, 3426, 3462, 3483, 3511	3167, 3345, 3359, 3403, 3503, 3531
Baumgartner & Bakker (2010)	-190	3300, 3321, 3402, 3418/3419, 3432, 3536	3242, 3386, 3404/3405, 3410, 3430/3431	3196/3197, 3215/3217, 3362/3368, 3423/3424, 3444/3446, 3475	3190, 3242, 3318, 3352, 3376, 3403, 3423/3424, 3462/3471, 3557	3188/3189, 3250, 3322/3326, 3397, 3402, 3422, 3456/3458, 3479/3481, 3510/3511	-
Uriarte et al. (2014)	-172	-	1626, 1643, 1660, 1665, 3242, 3383, 3399, 3406, 3411, 3431	1627, 1643, 1662, 3384, 3399, 3406, 3411, 3431, 3452	3211, 3215, 3388, 3437, 3454, 3475, 3491	-	-

Compared to the other (Na^+, Ca^{2+}) hydrates, Mg-hydrates cannot be found in each inclusions, only in cases where 3510 (cm^{-1}) band can be found. Thus, variation in Mg-content can be possible. Sulfate SO_4^{2-} was also identified in the inclusions confirmed by a narrow band at 983 cm^{-1}. Since the ice peak is highly temperature dependent, the lowering temperature causes shifting in ice peak to lower values.

Shifting in the peak positions of the other components are negligible influenced by the temperature changes. Considering that the primary fluid inclusions formed from saturated seawater, KCl is expected in the solute of fluid inclusions, but due to lattice geometries, KCl has weak Raman scatter.

From the eight major seawater ions, Cl^-, SO_4^{2-}, HCO_3^-, Br^+, Na^+, Mg^{2+}, Ca^{2+}, and K^+ (Hay et al., 2006), comprising 99.76 % by weight of the dissolved salts, five were able to identify (Cl^-, SO_4^{2-}, Na^+, Mg^{2+}, Ca^{2+}) with the combination of Raman spectroscopy and microthermometry.

5.2.2. Bioactivity in the paleo environment

A surprising result was the identification of β-carotene by Raman spectroscopy in the matrix of solid components were washed out from the salt rock (Fig. 16). However, this biomarker is highlighted in evaporite studies. It is utilized as indicator of reductive environment (Brocks et al., 2005). The orange brine color is due to the carotenoids (organic pigments, including β-carotene used by microorganisms for protection from ultraviolet radiation) in halophilic microbial community (Teller, 1987; Pedrós-Alió et al., 2000; Oren and Rodríguez-Valera, 2001).

Knowing that organisms can have effect on halite precipitation (Cody and Cody, 1988; Gerdes et al., 2000), it is presumed that β-carotene in Praid salt rocks is originated from halobacteria, which are tolerant for hypersaline environment. The presence of life in a brine can grow the number and size of fluid inclusions in halite (Gerdes et al., 2000). Microorganisms also can be entrapped and preserved for tens of thousands of years in fluid inclusions (Lowenstein et al., 2011). Furthermore, β-carotene has key role in the searching for trace of life on the Mars (Vítek et al., 2009).

However, the fluid inclusion petrography shows only dark organic material (Fig. 12/C,D), but the presence of β-carotene or more complex microorganism cells cannot be proved in Praid fluid inclusions.

5.2.3. The role of secondary fluid inclusions

The secondary fluid inclusions significantly differ from the primary ones in time and reason of their entrapment. Secondary fluid inclusions form after crystal growth via healing of fluid filled microcracks and deformation features. Fluid inclusions situated in transgranular site are classified differently (Fig. 13/C). In halite, many secondary inclusions can occur that they form a trails with different orientation. Crystals are shot through with dozens of healed fractures (Goldstein, 2001), which represent former fractural deformation(s) in the salt rock. During fracturing, fluids can migrate along the cracks. For this purpose, usually chemical composition of S-type fluid inclusions differs from P-type.

Raman spectroscopic study on secondary vapor phase fluid inclusions raised up open questions (Fig.17, 22). Basically, three types of gas were identified in the samples in the following abundance: N_2, CH_4, CO_2. The prevailing species is the N_2, which is mostly occur as a sole component of fluid inclusions (Fig. 22). Only in some cases were able to identify carbon-dioxide and methane besides nitrogen.

The composition of S1-type fluid inclusions is varying in a wide range comparing the results of Kátai (2017). However, the most significant gas species is the N_2 in both studies. The N_2-dominance in gaseous fluid inclusions likely suggests paleo atmospheric origin. Therefore, fluid inclusions in the Praid salt rock, during their burial history from tectonic to halokinetic upheaval, could be contaminated by other ancient or modern atmospheric gases during exhumation like as Blamey and Brand (2019) reported. The source of CO_2 and CH_4-rich gases, could be indicated from numerous reasons. Underlayered organic rich formations (marls, shales) (Krézsek et al., 2010), or even a deeper source could be the deep lithosphere. Faults penetrated the lithosphere were the possible transport medium of CO_2, and CH_4 (Frezzotti and Touret, 2014) complemented with nitrogen.

Possible explanation could be that during burial and secondary diagenetic alteration of halite some external gases may exchange or get incorporated (Blamey and Brand, 2019) into secondary fluid inclusions. The gas diffusion may arise difficulties in determination of the original gas content (Bąbel and Schreiber, 2014), mainly in case of those rocks, like that of the Praid salts. Nevertheless, Zimmermann and Moretto (1996) investigated the rate of diffusion at different temperatures. Results revealed that the gas component, diffused at first, above 320 °C. It is

supposed that this establishment is not correct, for that reason the physical conditions of secondary fluid inclusion is not clear yet.

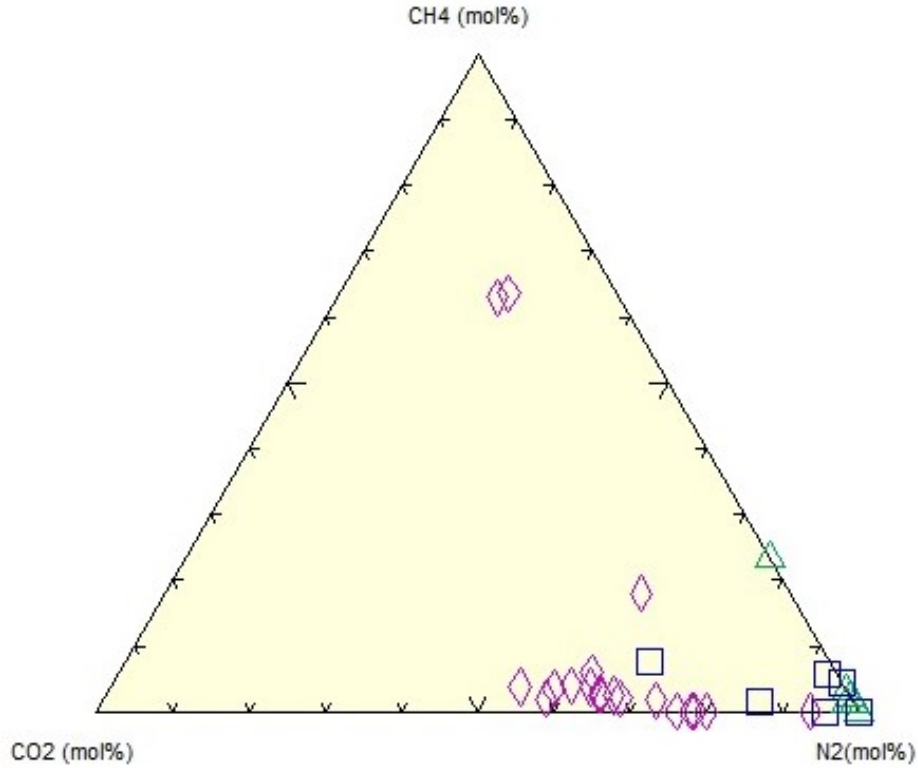

Figure 22. Composition of gas-bearing secondary fluid inclusions from Praid (in mol%). Blue rectangle represents massive type salt samples, whereas green triangle represents gas composition of layered type salt samples. Purple diamonds show data of Kátai (2017)***.***

Due to the maturation path of hydrocarbons, the oil (inclusions) are converted into solid bitumen, so releases gas (Schoenherr et al., 2007), thus it is possible that presalt organic material released its gas, which appeared and trapped finally in the secondary inclusions of Praid salt rock. However, origin of S-type fluid inclusions needs further investigation.

5.3. Evidences of salt tectonics

5.3.1. Generalities in salt tectonics

Salt tectonics includes all evaporites, but hereinafter the term is limited to halite which is the weakest rock even from the evaporite rocks. Halite salt rock typically has low creep strength, low elastic porosity, permeability and low density (Urai et al., 2008). These properties make salt resistive to hydrofracturing and enable its ductile deformation.

Already before its burial, rock salt forms a crystallized mass, having concrete compressive strength. In contrast, the siliciclastic sediments are usually unconsolidated, and they start to compact only later at near surface conditions. Confining pressure, at depth of 200-300 m under the covering layers, is increasing, the siliciclastic sediments become, resistant to pressure, but the salt rocks weaken by burial as temperature rises (Jackson and Hudec, 2017). Generally, the main driver of the tectonics is the differential loading. This is possible because of the highly weak and plastic properties of halite. Because of the inherent mechanical weakness salt, its body extrudes, as a glacier, or lifts up, as a diapir, easily (Warren, 2016).

The deformation mechanisms known to operate at temperatures relevant for natural halokinetic conditions (20-200 °C) are shown in Figure 23 (Urai et al., 2008). Developing of microstructures, at the grain scale depends mainly on the rock type: its mineralogy, impurities, intergranular fluid, grain size, fabrics, porosity and permeability. Besides rock properties, external parameters are equally important: i.e., temperature, lithostatic pressure, fluid pressure, differential stress and externally imposed strain rate (Trouw and Passchier, 2005; Jackson and Hudec, 2017). Experimental determination of the mechanical properties of salt rocks and extrapolation of these data to realistic geological conditions have provided a solid basis for understanding the rheology of the rock salt (e.g., Urai et al., 1986; Schoenherr et al., 2007). The detailed knowledge on petrography is a pillar, not only to understand the environment of the rock formation, but also to the salt tectonics. Identification of cracks, shape of boundaries, the occurrences and quantity of fluids in the salt rocks revealed by microscopic investigations plays significant role in microtectonic studies. This way one can find marks of various deformation mechanisms being active during the deformation of the studied salt body.

Microcracking and dilatancy occur at very low effective confining pressures (few MPa or less), and high differential stress (> 15 MPa) (Urai et al., 2008). Specific features break up grains, the inter and intra granular microcracking, grain rotations and intergranular slip, which are

important strain accumulating processes. At higher effective mean pressure and temperature (100-200 °C) **dislocation creep (DC)** is the dominant process leading halite deformation as crystals become more plastic. Dislocation density increases, then crystals start to cluster into diffuse bands and finally align into shape glide bands forming subgrains (Jackson and Hudec, 2017). This dynamic recovery process can occur even at confining pressure as low as 10 MPa. The presence of equiaxed subgrains is the typical features of halite grains (Pennock et al., 2005). Subgrains are defined as domains of homogenous crystallographic orientation separated by low angle (< 10°) misorientation boundaries (Thiemeyer et al., 2016). Third process is the **solution precipitation creep (SP)**, which can dominate if halite is fine-grained and contains considerable amount of fluids; for instance, in fluid inclusions, or as grain boundary films (Roedder, 1984). Fluids at grain boundaries can assist recrystallization, hence they could strongly influence the salt rock rheological properties (Urai et al., 1986). This fluid assisted process can reduce the dislocation density or remove dislocations along with their stored energy. In other words, the pressure solution can operate as effective mass transfer process around grain boundaries. Pressure solution is accompanied by intergranular sliding and rotation (grain rearrangement), may lead to compaction of porous salt (Spiers et al., 1990).

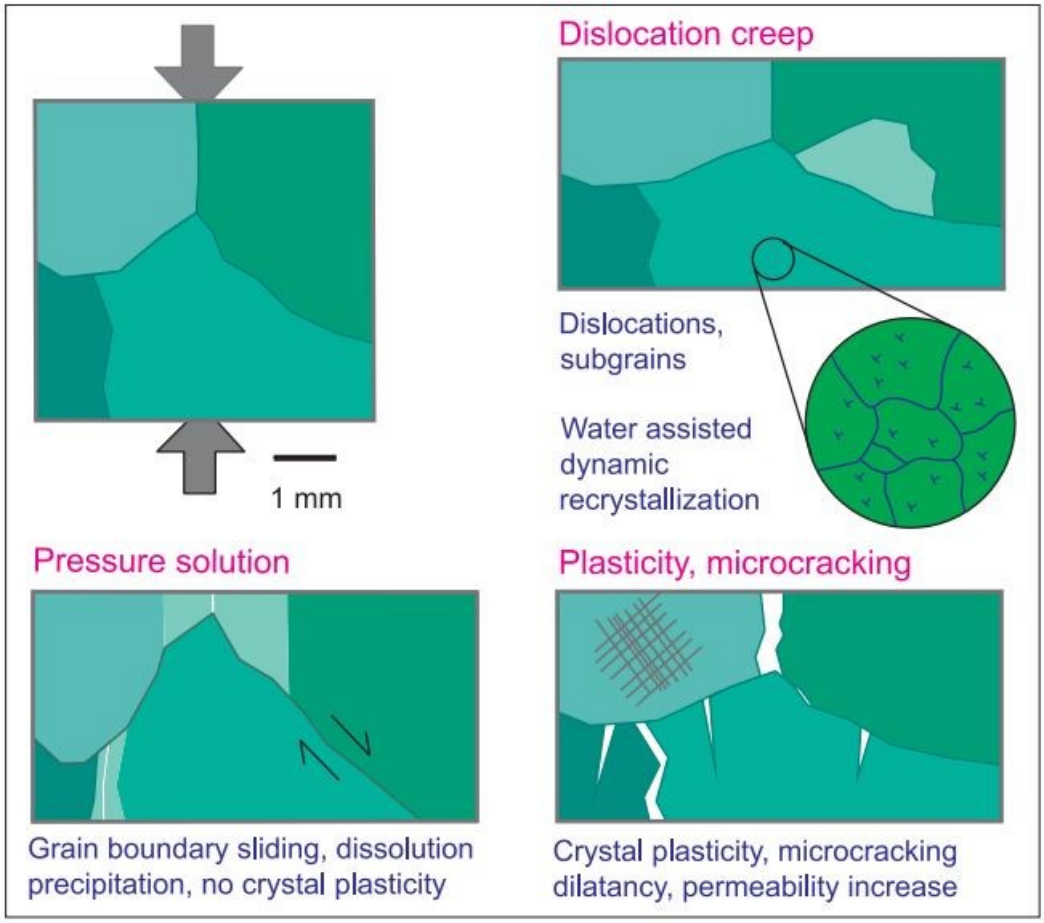

Figure 23. Schematic cartoon of the three microstructural processes that are known in rock salt at temperatures in the range 20-200 °C. Different shades of green mean different crystal orientations *(Urai et al., 2008)*.

5.3.2. Deformation mechanisms inferred micropetrographic study of the Praid samples

Salt rock microstructures provide information about the operating deformation mechanism(s) (Guillope and Poirier, 1979). Based on petrographic observations, the fabric of the Praid salt rocks is dominated by secondary features which is not surprising, being aware of its age and halokinetic history (Fig. 5). Deformation mechanism can be defined as change in shape or volume of the rock by inter- and intracrystalline processes (Jackson and Hudec, 2017).

The two types of salt rock, massive and layered show similarities in microstructural features (Table 9). Despite the macro (namely the development or the lack of contrasting layers, (Fig. 5) and petrographic differences (Fig. 9), only a few microstructural differences can be found. All the samples display only shape-preferred orientation. In all the studied samples the shape of subgrains is polygonal, suggesting deformation dominated by climb-controlled creep (Senseny et al., 1992; Schléder and Urai, 2005).

The massive salt sample (with code PAT17-4, Fig. 9/A), containing a large amount of chevron remnants is an exception. In this sample the majority of the grains are large (1-2 cm in size) and they contain subgrains, too. The other samples rather have much more subgrain-poor (or free) grains.

The subgrain-poor (or subgrain-free) grains, with their elongated shape provide clear evidence for strain energy driven GBM (Fig. 24). These grains, with their bulged boundaries, are interpreted to consume the subgrain-rich grains by GBM (Guillope and Poirier, 1979) in other words they replace the old grains. Typically, the subgrain-free halite grains are situated adjacent to subgrain-rich halite grains (Fig. 24). Observations made on both irradiated samples and in EBSD maps show the above-mentioned process. In many cases, the migrating grain boundaries consume old, milky, fluid inclusion rich parts of a grain (Fig. 10, 24) which can result in fluid "transport" to the grain boundaries from the inside of the grains (Schléder and Urai, 2005).

The local enrichment of insoluble and organic matter along anhydrite grain boundaries (Fig. 11/A-B) proves that solution precipitation creep was an active deformation mechanism in the studied salt rock (Zulauf et al., 2010; Thiemeyer et al., 2016).

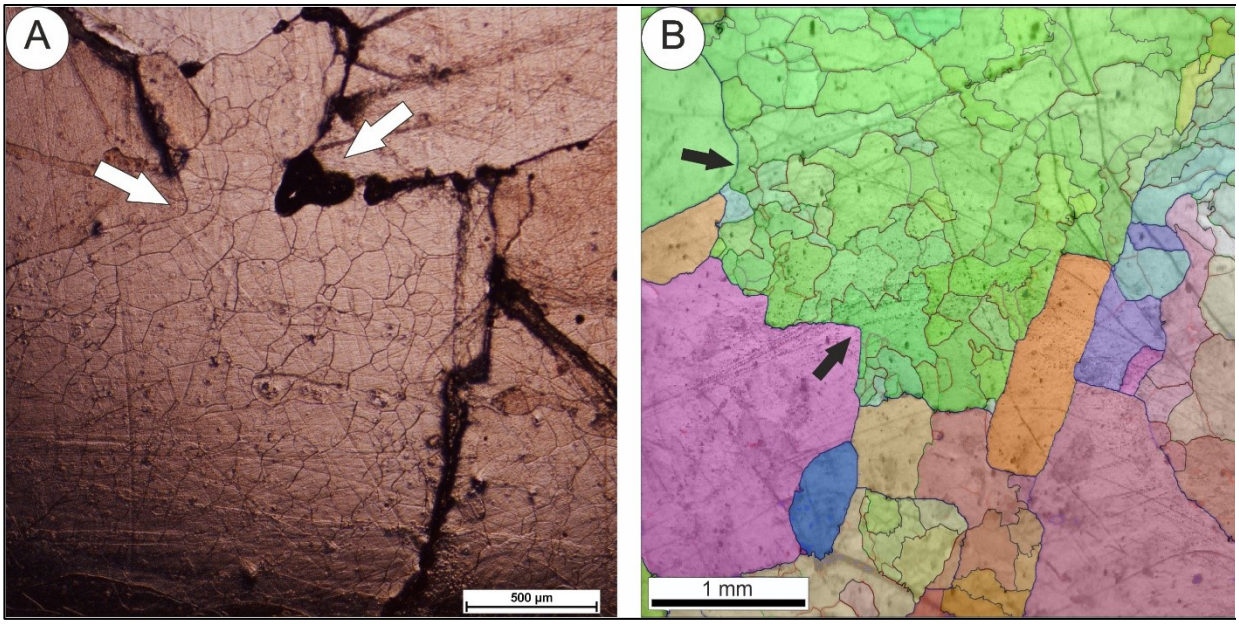

Figure 24. Microstructural observations with reflected light microscope and on an EBSD map. A: Photomicrograph of irradiated, etched thick section under reflected light showing halite grain boundary (black irregular thick lines) and subgrain boundaries (hairlines). White arrows show propagation of grain boundaries towards to the subgrain rich samples, causing concave grain boundaries. Black spots at the grain boundaries and inside of the substructured grain are fluid inclusions, which opened during sample preparation. Sample: PA40-PH, reflected light. B: EBSD map shows grains with different crystallographic orientation. Black arrows show the direction of the growing subgrain free grains consuming the green, subgrain rich crystal. Sample: PAT19-7.

Comparing the calculated subgrain diameter in EBSD mapped samples and gamma irradiated samples, the values are fairly overlapping (Table 11). Both techniques lead to the same result. Microstructural studies made on gamma irradiated samples and EBSD map interpretations proved that both types of halite samples (massive and layered) provide evidences for both dislocation creep and solution precipitation (SP) creep during the deformation of the salt dome at Praid. The observations mentioned above suggest a complex effect of competitive dislocation and SP creep leading to grainsize reduction and activation of the entrapped fluids during deformation.

Table 11. Grain size statistics based on the EBSD and gamma irradiation measurements. The diagram shows that the subgrain size measurements obtained from the two techniques are overlap. The mean subgrain size of layered and massive salt is about 113 µm and 81 µm, respectively.

Rock type	**Subgrain diameter (µm)**	
	EBSD	**Gamma irradiation**
Layered salt	143.21	129.61
	132.64	134.44
	172.77	125.82
	100.14	128.99
	48.26	122.88
	92.09	
	66.95	
Massive salt	99.02	68.34
	67.06	94.40
	81.56	89.28
	83.28	
	76.79	
	93.97	
	70.52	
	77.54	
	70.80	

5.3.3. Differential stress and strain rate estimation

One of the main goals of the deformation experiments is that their results could be applicable in understanding geologic conditions (Jackson and Hudec, 2017). The salt deformation experiments showed that there is a near linear inverse relationship between the deviatoric stress and the resulting subgrain diameter (Carter et al., 1993). Hence, the differential stress responsible for halite the deformation of halite could be estimated (Table 12).

Table 12. Selected rock salt deposits of different geological settings with examined halite grain sizes and differential stress. Salt fountain shows smaller grain size and higher differential stress compared to the domal salt examples, such as Praid.

References	Mean average grain size (mm)	Mean differential stress (MPa)	Locality	Geological setting
This study (massive salt)	1.3-1.5	1.6 - 2.3	Praid	Salt dome
This study (layered salt)	1.1	1.8		
(Thiemeyer et al., 2016)	3.4	1.1-1.3	Gorleben (Germany)	Salt dome
(Kneuker et al., 2014)	<5	1.2-2.9	Morsleben (Germany)	Salt dome
(Mertineit et al., 2014)	0.3-2.5	2.28 - 2.97	Gorleben (Germany)	Salt dome
(Schléder et al., 2007)	3 - 25	0.9 - 3.1	Klodowa (Poland)	Salt dome
(Schoenherr, 2008)	2 - 30	< 2	Birba, Harweel (Oman)	Salt diapir
(Desbois et al., 2010)	< 0.5	3.1 - 4.8	Quom Kuh (Iran)	Salt fountain

Flow laws were constructed based on experiments and theoretical calculations. Based on the detailed microstructural observations, both dislocation creep and pressure solution processes act concurrently in the Praid salt rock. Considering steady state, non-dilatant deformation, the flow law of rock salt deformation by steady state dislocation creep is

$$\dot{e}_{DC} = 8.1 \times 10^{-5} \sigma^{4.5} e^{\left(-\frac{51.6}{RT} * 10^{-3}\right)} \quad \text{(A)},$$

where $\dot{e}_{DC}$ is the strain rate expressed in s^{-1}. The 8.1 is a dimensionless pre-exponential material constant and -51.6 (J/mol) represents the activation energy in the Arrhenius member of the equation, R is the gas constant ($J \cdot K^{-1} \cdot mol^{-1}$) and T is temperature in Kelvin (Wawersik and Zeuch, 1986; Carter et al., 1993). This flow law is a precise formulation, but, for a given differential stress, the rate of dislocation creep can vary by about three orders of magnitude because of differences in impurities and in solid solution (Jackson and Hudec, 2017).

For rock salt deformation by solution–precipitation creep the flow law is

$$\dot{e}_{PS} = 4.7 \times 10^{-4} e^{\left(-\frac{24.5}{RT} * 10^{-3}\right)} \left(\frac{\sigma}{Td^3}\right) \quad \text{(B)},$$

where 4.7 is a material parameter, -24.5 is activation energy (J/mol) for pressure-solution creep, σ is the differential stress (MPa), *d* is the grain diameter (mm). Pressure solution creep is strongly dependent on grain size, while dislocation creep deformation is grain size independent. Since there

is no available data about paleo geothermal temperature values, the present day value was used (~35 °C/ km), T = 323 K in the calculations.

The total strain rate is given by the sum of dislocation creep (DC) and pressure solution (PS) strain rates:

$$\dot{e} = \dot{e}_{DC} + \dot{e}_{PS} \qquad \text{(C).}$$

In the case of the Praid samples, the strain rate of DC creep plays a minor role compared to the SP creep (Table 13).

Table 13. Calculated differential stress and strain rates obtained from A and B equations. The higher strain rate belongs to the solution precipitation creep.

Rock type	**Differential stress (MPa)**	**Flow Laws**	
		Dislocation creep (s^{-1})	**Solution-precipitation creep (s^{-1})**
Layered salt	1.7	$5.1*10^{-12}$	$4.6*10^{-10}$
Massive salt	1.6	$1.9*10^{-11}$	$3.1*10^{-10}$
Porphyroclast rich massive	2.4	$2.5*10^{-12}$	$1.5*10^{-10}$

5.3.4. Interpretation of secondary displacements

Based on the observations presented, a concept is drawn up for the microscale processes by which the Badenian salt of the TB deformed.

The initial burial of the salt induced only slight deformations in the primary fabric. Original chevron-type grains, containing primary fluid inclusions were probably more abundant, with a notable amount of fluids at the early stage of salt deformation.

Subsequently, the organic materials started to decompose and possibly converted into bitumen, as happened in the case of Ara salt (Schoenherr et al., 2007).

Due to the increasing differential stress and temperature, the syndepositional fluid inclusion-rich halite crystals were partially or totally recrystallized and their fluids were added to the pore fluid which is evidenced by grain boundary migration process (Drury and Urai, 1990).

During this process, the grain boundary fluids (including those originating from decomposed organic material) started to form continuous fluid films bordering the grains (Fig. 13/C) and wormlike tubes (Fig. 13/D), respectively.

It is expected that while a grain boundary sweeps through a milky and fluid inclusion-rich area it collects the available fluid inclusions. This process could continue until the driving force is ceased. Although it is possible that the PS creep played significant role in halite alongside dislocation creep process, at least in the early stage of halokinesis.

Because the recent depth of the sampled rocks is shallow (< 200 m from the surface), it is possible that the salt layer was affected by a higher than normal temperature gradient caused by nearby Late Miocene volcanism (Krézsek and Bally, 2006; Szakács and Krézsek, 2006) and along with temperature increase related to the burial depth (800-1000 m). Recently the salt body moved upwards to near-surface position. As differential stress decreased, and the solution precipitation creep process became less pronounced. Fluid films still exist in the samples, so the diffusional processes are still active.

Furthermore, the differential stress calculations on Praid rock salt samples, indicating a maximum differential stress less than 2.4 MPa for massive salt and < 1.8 MPa for layered salt. These values are in accordance with the dataset of diapiric salt related stresses worldwide (Carter et al., 1993; Schoenherr et al., 2007, Table 12). As Fig. 24 shows, at recent differential stress, the dominant deformation mechanism is the SP creep until higher temperature (~100 °C). The strain rate (total strain rate between $2.5*10^{-12}$ s^{-1} and $1.9*10^{-11}$ s^{-1}) calculations are in an agreement with the observed features in the Praid salt mine, where the ~260 year old salt extraction chamber (József shaft) suffered at least 10 % compressional displacement (Deák et al., 2008).

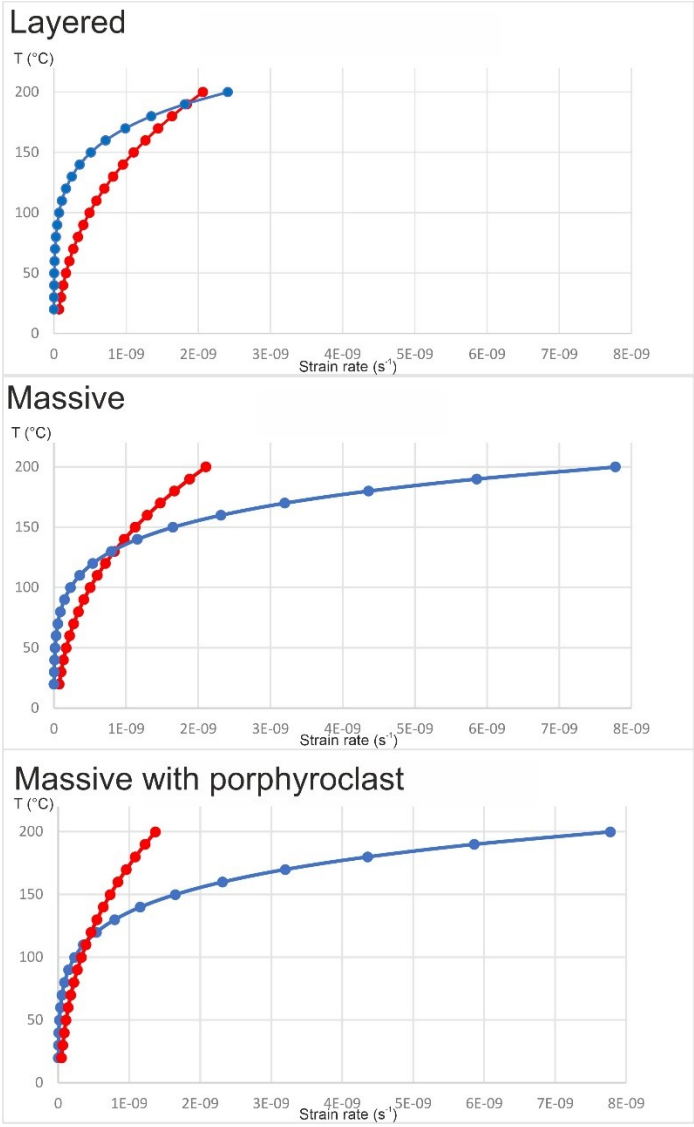

Figure 25. Strain rates – temperature plots at given differential stress calculated from the Praid samples. The strain rate paths depend on the calculated differential stress and grain size. Blue line represents strain rate of dislocation creep whereas red line shows strain rate of solution precipitation creep in the studied samples. Note that at lower temperatures, the predominant strain rate always the solution precipitation creep. The highest impact of dislocation creep manifested in the porphyroclast rich massive salt, where dislocation creep could be dominant until ~ 110 °C.

5.4. Stable isotopic characteristic of minerals and fluid inclusions

The isotopic composition of evaporite minerals depends on composition of salt minerals dissolved in the evaporating water and in particular on the proportions of specific dissolved ions originating from specific sources in the solution/water. There are many natural types of salty waters in the Earth environments; however, the largest reservoir for most evaporites is the world ocean (Bąbel and Schreiber, 2014). Since the ocean is currently mixing its water masses, mainly due to continuing thermohaline circulation, leading to homogeneity of its composition. The isotopic composition of components in the seawater is also fairly constant (Knauth and Beeunas, 1986; Holser, 1992; Lecuyer et al., 1998). This is the basis for the construction of many isotopic curves for the cases of ancient seawater, crucial for interpreting the results of geochemical analysis (Bąbel and Schreiber, 2014).

5.4.1. Isotopic characteristic of sulfates

The most abundant accessory mineral in the studied salt rocks is the anhydrite, which is a common constituent of evaporites. Although, the relative timing of its formation is questionable, anhydrite is typically mentioned as a secondary mineral after gypsum (Warren, 2016). Gypsum converts into anhydrite upon reaching a temperature ($T_{gp\text{-}an}$) which varies according to the physical and geochemical environment (Jowett et al., 1993).

The following equation describes this chemical reaction:

$$CaSO_4 * 2H_2O \rightarrow CaSO_4 + 2H_2O \qquad (D)$$

The activity of water in the solution plays a key role in which a sulfate mineral forming (Hardie, 1967). Normal water activity ($\alpha_{H2O} = 0{,}93$) in the ocean results in gypsum precipitation (Jowett et al., 1993). In turn, formation of syngenetic anhydrite could be expected when halite is precipitated at the same time, since more saline brine has lower water activity ($\alpha_{H2O} = 0.75$), thus the $T_{gp\text{-}an}$ is around 18 °C (Fig. 26). The anhydrites of Praid salt rock are supposed to be syndeposition type in origin for instance, the appearance of euhedral tabular anhydrite trapped as solid inclusion in halite (Fig. 11/A,B). As a consequence, the anhydrite could be formed along with the halite precipitation.

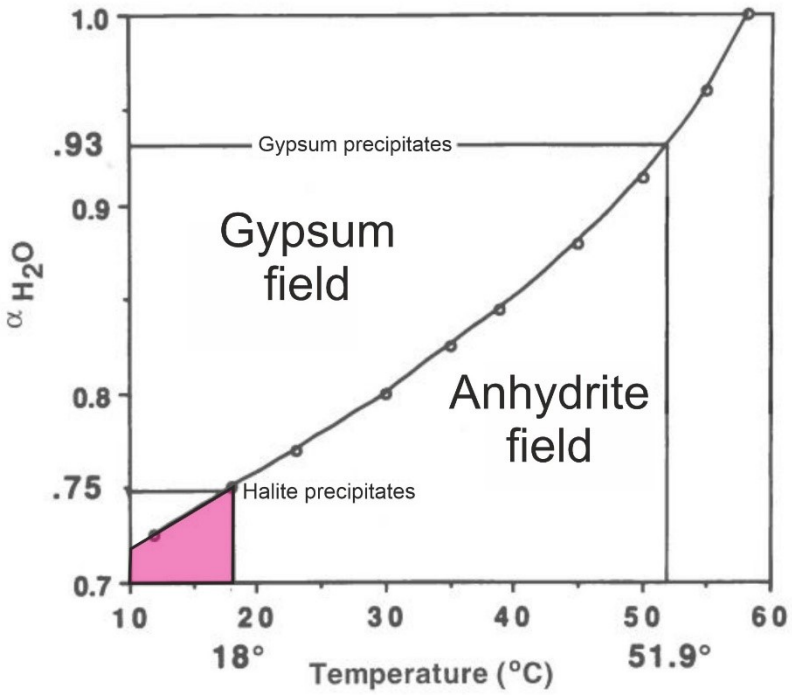

Figure 26. Water activity – temperature plot draws gypsum and anhydrite stability fields. Purple field indicates the temperature and water activity conditions, in saturated water, at which anhydrite crystallization is dominating. Measurements of Hardie (1967) were made under laboratory conditions. Diagram modified after Jowett et al. (1993).

The results of the isotopic study on Praid anhydrite cover a narrow range. Values of the $\delta^{34}S$ are between +20.4 ‰ and +22.4 ‰, the $\delta^{18}O$ between +12.9 ‰ +14.5 ‰ (Table 4, Fig. 27), which clearly demonstrate its seawater origin (Rollinson, 1993). However, the sulfate isotopic composition of ancient seawater was changed through time. As Claypool et al. (1980) summarized in their pioneering work the „age curves" of sulfur and oxygen isotopes in marine sulfates, they pointed out that the mean isotopic composition in the Miocene was around ~+22 ‰ for $\delta^{34}S$ and +13 ‰ for $\delta^{18}O$. Comparing the isotopic result of this study with other Badenian evaporite, sulfate isotope data (Claypool et al., 1980; Halas, 1987; Kasprzyk, 1997), it is obvious that they are in a good agreement to each other (Fig. 27, Table 14). Note, that the sulfur delta values from Praid are a bit lower (with 1 ‰) than the BSC values. The slight difference between values of Praid and the other BSC sulfates (gypsum, anhydrites from the Carpathian Foredeep) are due to the presence of tiny pyrite crystals adhered to anhydrite crystals (Fig. 10/A,B). Sulfides (e.g. pyrite) prefer light isotopes into incorporate (Rollinson, 1993). The sulfate isotope values of the BSC overlap with

the sulfate isotope results measured on Messinian evaporites, but separated from the present-day sulfur isotopic composition (20 ‰) of the oceans (Fig. 27, Table 14).

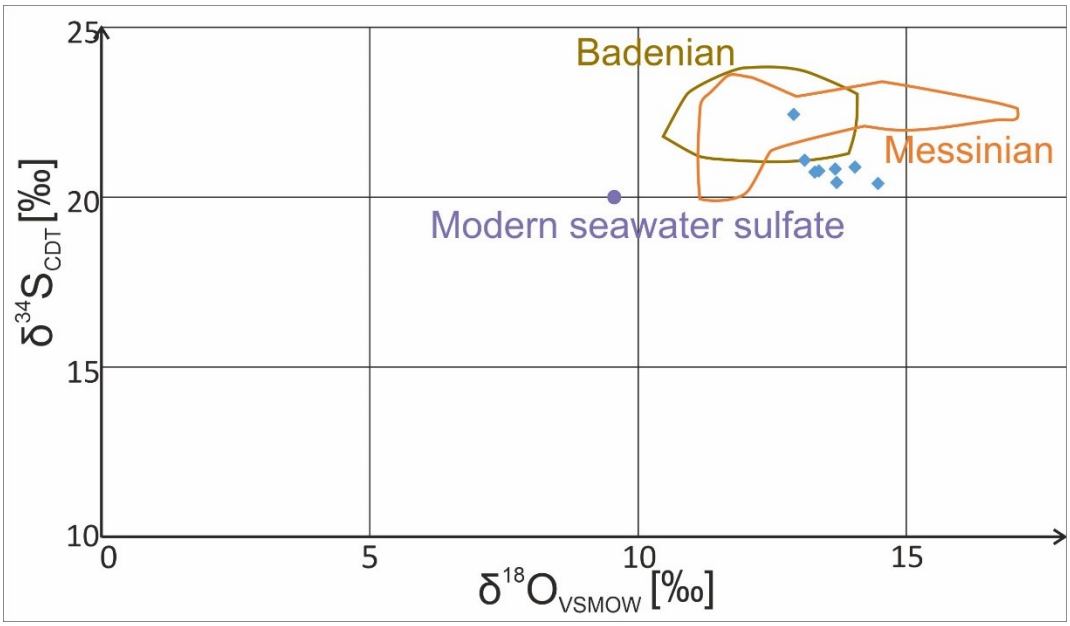

Figure 27. Isotopic variation of S and O of anhydrite from the Badenian Salinity Crisis, Messinian Salinity Crisis and the modern ocean for comparison. Blue diamond indicates data of this study. Badenian Salinity Crisis: Claypool et al. 1980; Halas & Krouse 1982; Kasprzyk 1997; Peryt et al. 2002; Cendón et al. 2004; Messinian Salinity Crisis: Evans et al. 2015; García-Veigas et al. 2018; Longinelli 1979, modern ocean: Claypool et al. 1980.

Table 14. S and O isotopic composition of the Badenian Salinity Crisis evaporite and the two best known (Messinian and Permian Zechstein) salt giants.

Publication	Age	Sample	$\delta^{34}S$ (‰)	$\delta^{18}O$ (‰)
This study	Middle Miocene (Badenian)	Anhydrite	+20.4 - +22.4	+12.9 - +14.5
(Hałas and Krouse, 1982)	Middle Miocene (Badenian)	Gypsum	+22.4 - 23.6	+12.9 - +13.9
(Kasprzyk, 1997)	Middle Miocene (Badenian)	Gypsum	+21.4 - +22.6	+11.3 - +12.6
(Peryt et al., 2002)	Middle Miocene (Badenian)	Gypsum	+ 21.5 - 23	+12.7 - +13.9
(Cendón et al., 2008)	Middle Miocene (Badenian)	Gypsum	+22 - +23.6	+11.3 - +13.4
(Claypool et al., 1980)	Middle Miocene (Badenian)	Gypsum	+ 21.6 - +21.9	+10.8 - +12.9
(García-Veigas et al., 2018)	Late Miocene (Messinian)	Gypsum	+22 - +23	+12 - +17
(Longinelli, 1979)	Late Miocene (Messinian)	Gypsum	+20.1 - +21.2	+12.2 - +14.8
(Evans et al., 2015a)	Late Miocene (Messinian)	Gypsum	+21.9 - +23.3	+11.3 - +14.5
(Claypool et al., 1980)	Permian	Anhydrite	+9.5 - +11.5	+ 9.7 - +11

In addition, the low ratio of $\delta^{34}S/\delta^{18}O$ ratio (1.6-1.8) could be a sign of bacterial sulfate reduction (Longinelli, 1979; Pierre, 1985). The Praid sulfate isotopes ratios are very close or fall in to the sulfate reduction range (1.4-,1.7).

5.4.2. Isotopic characteristic of carbonates

Dolomite**,** frequently called as limpid dolomite is a common constituent of evaporites. However, the relative time of their crystallization is unclear. Dolomites in salt rock euhedral in shape and considered as authigenic minerals. As such, limpid dolomites can form in a wide range of environments ranging from mixing zones to refluxing brines moving through recently deposited halite beds (Warren, 2000). Limpid dolomite in mosaic halite was documented as a late, ordered, stoichiometric, euhedral to subhedral set of dolomite crystals along the contact between bedded

halites and interbedded mudstones in platform evaporites (Naiman et al., 1983; Gao, 1990). In Praid samples, however, dolomite can be found in halite grains as inclusions and along/at grain boundaries both in massive and layered salt samples.

The isotopic analyses of dolomite could provide insights into the origin of the crystal forming carbonate. The results of Praid samples show negative values both for $\delta^{13}C$ (-7.07 - -4.55 ‰) and $\delta^{18}O$ (-9.03 - -8.31 ‰). The reason of such low values can be explained in several ways. The negative $\delta^{18}O$ could be caused by mixing of seawater and meteoric water as Peryt and Peryt (2009) suggested by the case of BSC related carbonates from the Carpathian Foredeep.

Natural variations in the $\delta^{13}C$ of the marine CO_2 can mainly be attributed to the effects of two processes (Vergnaud-Grazzini, 1983):

1) it is linked to the so-called apparent oxygen utilization, which, in turn, is related to the progressive oxidation of organic matter resulted in decreasing of $\delta^{13}C$,

2) the second process concerns change in the volumes of exchangeable CO_2 reservoirs.

Increasing oxidation of organic matter towards deep water causes an elevation of total CO_2, nitrate, phosphate concentration and decrease of dissolved O_2 concentration and $\delta^{13}C$ (Vergnaud-Grazzini, 1983). In deep waters longer residence time favors the addition of light carbon by the oxidation of organic matter and by the dissolution of carbonate. Thus, the grater the residence time, the lower the $\delta^{13}C$ of the total CO_2.

The light carbon could originate from organic material which occurs almost everywhere on the Earth, even in a salinity crisis. Presence of β-carotene (Fig. 16) and black, organic rich primary fluid inclusions (Fig. 12/C,D) suggest the presence of life in the Badenian seawater. Furthermore, particular species of bacteria can enhance the formation of dolomite with light carbon. Sulfate-reducing-bacteria and other microbes oxidize organic matter (e.g. cyanobacteria) to maintain and enhance their metabolism (Wright and Wacey, 2005). The process is expressed as series of chemical reactions, which result in enzymatic breakdown of proteins. This process generates NH_4^+ which could increase the seawater pH and carbonate-related alkalinity (Berner, 1980). Sanz-Montero et al. (2008) pointed out that the isotopic characteristics of dolomites basically reflect the isotopic composition of their close environment. So, the supposed activity of sulfate-reducing bacteria in the BSC sea could led to increase of the dissolved ^{12}C in seawater, thus to negative $\delta^{13}C$ values of dolomite.

Other plausible explanation for the negative $\delta^{13}C$ and $\delta^{18}O$ values could be that the Praid dolomites nucleated on organic particles (Fig. 11/C). This material cannot be extracted from the dolomite, hence all measurements on dolomites were contaminated with the organic material. Nonetheless, the amount of organic matter inside the dolomite are relatively small compared to the full volume of dolomites.

The mixing process of fresh ground water and intruding seawater is well known in modern oceans and led to decrease $\delta^{13}C$ and $\delta^{18}O$ values in dissolved carbonate (Magaritz et al., 1980). Following the rationale described above, one can consider the carbon isotope compositions in terms of a number of distinct CO_2 source reservoirs: Atmospheric ($\delta^{13}C$ =-7 ‰), marine bicarbonate ($\delta^{13}C$ = +2 ‰), organic carbon in (marine and land) sediments ($\delta^{13}C$ = -26 -7 ‰) (Koch et al., 1992), and mantle ($\delta^{13}C$ = -5 ‰) (Craig, 1953) are the main reservoirs. Vergnaud-Grazzini (1983) reported by means of foraminifera isotope geochemistry that there was significant difference in carbon isotopic ratio between the surface (similar to the recent ones) and deep water ($\delta^{13}C$ =-0.6 ‰) (lower than those today).

However, the paleo surface of the continental land at the study area and its surroundings (e.g. uprising Carpathian arc) is not known, therefore it is possible that notable amount of freshwater ended to the Central Paratethys sea (Cendón et al., 2004). Kováčvá et al., (2009) measured $\delta^{13}C$ and $\delta^{18}O$ values between +3 ‰ and -2.3 ‰ and between +0.1 ‰ and -5.1 ‰ for Badenian carbonates located in the Vienna Basin. The negative values are explained by water input of the paleo-Danube river which affected the near-surface waters of the Vienna Basin at the time of carbonate formation (Kováčová et al., 2009).

To summarize the results and viewpoints, the Praid dolomite possibly formed in a sector of the water column where the water composition in favors dolomite precipitation and the CO_3^{2-} ions had negative (C- and O) isotopic compositions, for the following reasons: the evaporation of seawater (retain lighter O isotopes in water), presence and breakdown of organic material (lowered the C-isotopes) and meteoric water (lowered both C- and O-isotopes) input could play significant role in the formation of the dolomite.

5.4.3. Isotope geochemistry of fluid inclusions in halite

The stable isotope geochemistry of fluid inclusions as well as that of solid minerals may provide important geochemical information on the formation environments of the host minerals

(Lazar and Holland, 1988; Horita, 1990; Ayora et al., 1994). Therefore, the stable isotope study should be carried on primary FIs as a possible way to characterize the composition of the paleo seawater, from which the evaporite minerals precipitated (Bąbel and Schreiber, 2014).

Fluid inclusion in ancient halite preserved the highest probability, as compared to other common marine evaporite minerals, such as gypsum, which could be altered by dehydration during burial (Jowett et al., 1993). In traditional stable isotopic studies one can deal with the $^{2}H/^{1}H$ and $^{18}O/^{16}O$ ratios of water molecules (Hoefs, 2009). Expressing how much the heavy isotope is enriched or depleted in a sample relative to the standard is a fundamental step in isotope geochemistry. The global water cycle has regularities in isotopic characteristic of its waters (e.g. atmospheric water, seawater, vapor). The H_2O in seawater precipitating halite represents the largest proportion of terrestrial water found in oceans (Alexandre, 2020).

During evaporation, the isotopically lighter water molecules are selectively transferred into vapor phase, leading to enrichment of the remaining liquid in the heavier isotopes and the moisture in the lighter one (Bąbel and Schreiber, 2014). The precipitated water, i.e. meteoric waters, is plotted on a $\delta^{18}O$ versus $\delta^{2}H$ diagram where the results will fall on the distinct line, called Global Meteoric Water Line (GMWL) defined by Craig (1961)

$$\delta^{2}H = 8\delta^{18}O + 10 \qquad \text{(E)}$$

which describes the mass-dependent fractionation of water. In the Nature the coefficient 8 and the constant (d=10) may vary depending on wide range of processes. For instance the conditions of evaporation (wind direction and intensity), vapor transport (distance from the source), moreover, the crystallization from the solution (Hoefs, 2009; Bąbel and Schreiber, 2014) could change the water isotopic ratio of the solute. During evaporation, kinetic fractionation will occur. Waters undergone evaporation displays systematic enrichment in both ^{2}H and ^{18}O resulting in divergence from the GMWL along evaporation lines having slopes of less than 8 (often in the range 4 to 6) (Gibson et al., 1993).

During seawater evaporation, the solution is getting more concentrated, reaching the saturation value of various minerals. Their crystallization process could considerably disrupt the isotope exchange process. At a certain point, sulfates and chlorides will start to precipitate. Most of the evaporite minerals incorporate hydrogen and oxygen or both. The crystallizes phases prefers the heavier isotopes, because the atoms/ions are bond much stronger in crystals than in water (e.g.

Alexandre (2020)). As this process starts to be dominant, the direction of the evaporation line will tend to curve to opposite direction (Fig. 28).

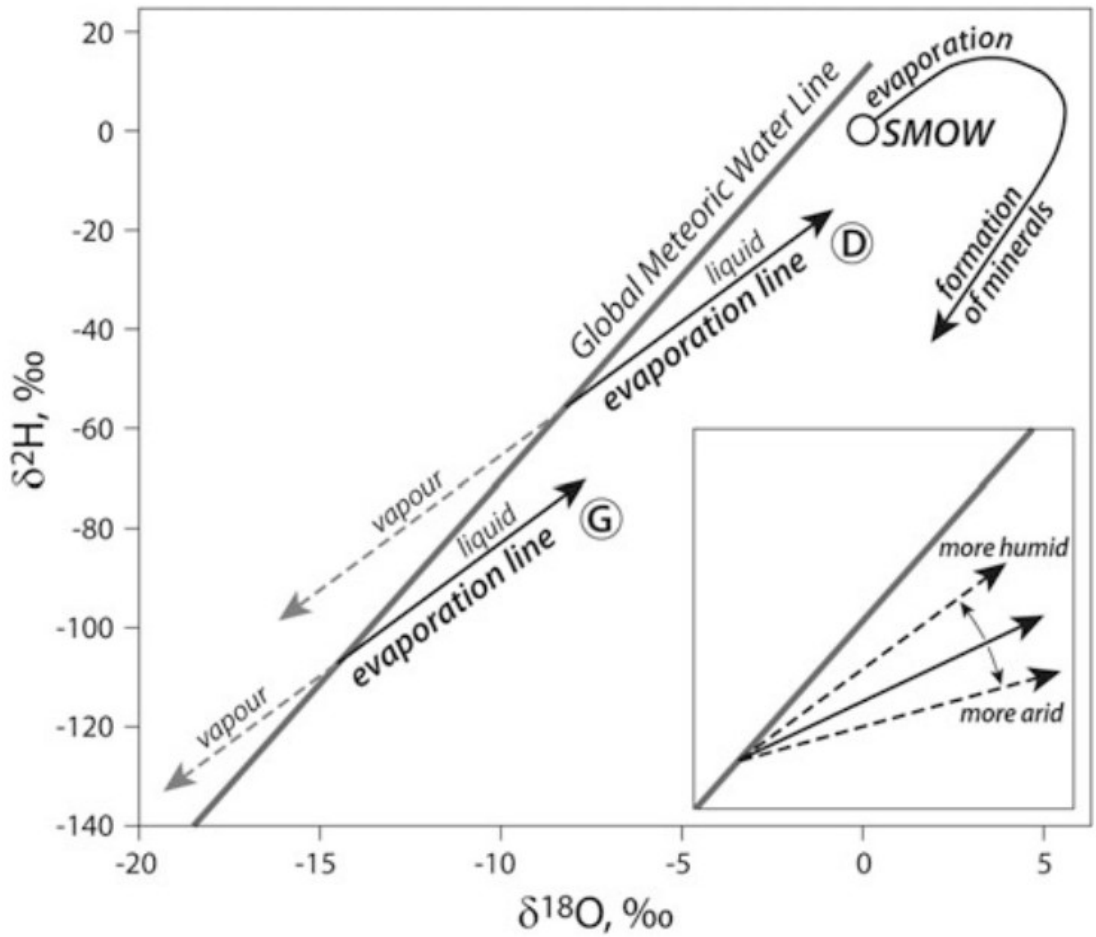

Figure 28. Effects of evaporation from freshwater sources or seawater, using two examples: Rio Grande in the USA and Mexico (G) and the river Darling in Australia (D). As crystallization process accelerates in the saturated seawater, the direction of the evaporation line will tend to curve to opposite direction: this happens when fractionation from precipitation of minerals overtakes fractionation from evaporation.(Alexandre, 2020)

The Praid salt rock samples show larger negative values of the O and H isotope ratios compared to the literature data, which raise some questions (Fig. 29). Considering that only a few studies were performed for halite fluid inclusion isotopes, the protocol of the measurements is not well-developed. Crushing method during sample preparation releases the fluids from the inclusions randomly, which makes difficult to exclude some secondary inclusions from being crushed and their content released for analysis (Blamey and Brand, 2019). Thus, the presence of fluids coming from secondary inclusions cannot be completely avoided from the measurement. However, their

volume is an order of magnitude smaller compared to that of primary FIs. Other source of uncertainty could be the off-line way of inclusion fluid extraction. The vacuum crushing extraction in the stainless steel tube can cause some undesired fractionations prior to the measurements as Knauth and Beeunas (1986) pointed out. Considering that the composition of fluid inclusions is very complex, namely FIs contain several ions, it is possible that the ions with high ionic radii, such as Mg^{2+} attract the heavier ^{18}O isotopes so this reaction can cause even 5 ‰ shift in the water oxygen delta values (Knauth and Beeunas, 1986; Koehler et al., 1991).

In turn, Kovalevych et al. (2009) and Petrychenko et al. (2005) indicated, that the chemical composition of many basinal waters of marginal marine evaporites preserved in primary halite inclusions was indeed different from recent seawater brine. Grothe et al. (2020) studied isotopes of gypsum hydration water and the salinity of fluid inclusions in Late Miocene Messinian-gypsum. Their results indicate large freshwater inputs during gypsum formation. Rigaudier et al. (2011) also obtained negative isotope values from Messinian halite fluid inclusions. The studies mentioned above show negative delta values, suggesting a very complex system in the Central Paratethys realm during Miocene times.

The trend ($D=0{,}92*\delta^{18}O$ -70,68) of Praid fluid inclusion isotope data cross the GMWL at -11 ‰ and -81 ‰ for oxygen and hydrogen respectively, which is assigned to the initial composition of seawater (Gibson et al., 1993). The Local Meteoric Water Line was chosen from the St Anna Lake located in the Harghita Mts. (Túri et al., 2016) (Fig. 27). The results of Praid samples yelded a wide range and they overlap with those obtained by other oxygen and hydrogen isotopic studies (Fig. 29, Table 15) which were measured on the gypsum hydration waters of BSC evaporite from the Carpathian Foredeep (Kasprzyk and Jasińska, 1998). Considering the amount of other evaporite minerals (anhydrite, dolomite), and the paleo geographic position of the Transylvanian Basin (isolated basin), the negative values of water obtained from halite fluid inclusions reveal a restricted basin, where the effect of evaporation was overtaken by the effect of crystallization and/or the meteoric water input could have a notable effect. Rigaudier et al. (2011) calculated, from the isotopic composition of water trapped in fluid inclusions in Messinian halite, that the crystals grew in a mixture of seawater and meteoric waters dominated by the latter (50–75%).

The above discussed (Chapter 5.4.2.) dolomites are also characterized by negative $\delta^{18}O$ values (Table 4) whereas anhydrites have positive δ values, which are typical for marine environment (Rollinson (1993),Table 5, Fig. 27).

The so-called hook appearing the trendlines of particular brine bodies (Alexandre, 2020, Fig. 28) is not observed in the Praid data: the evaporation line is straightforward. The isotopic signals of evaporation pathway in such a strongly deformed salt deposit as that at Praid, cannot be as precise as in a modern evaporite, where one can have better sample from the salt rock and, thus, can reconstruct the evaporation processes more accurately.

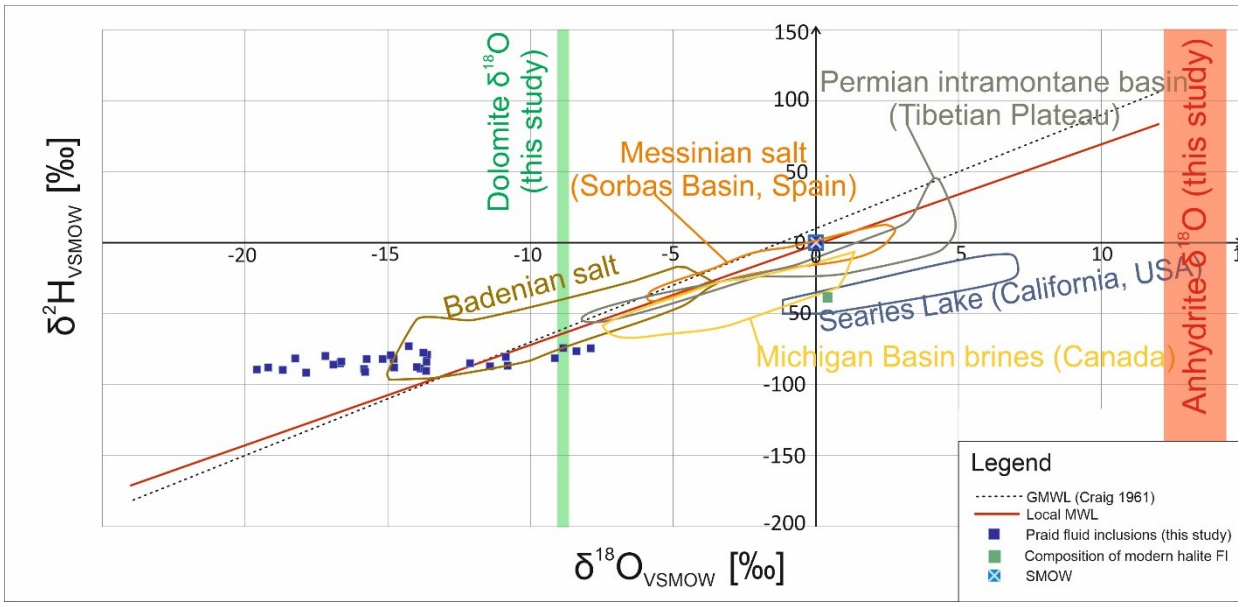

Figure 29. Variation of δ^2H and $\delta^{18}O$ of fluid inclusions, dolomites and anhydrites occurring in massive salt rock type. Data of previous studies are shown for comparison: Badenian Salinity Crisis: Halas and Krouse (1982); Kasprzyk and Jasińska (1998). Messinian Salinity Crisis: Rigaudier et al. (2011); Evans et al. (2015). Michigan Basin brines: Wilson and Long (1993). Permian intramountain basin: Li et al. (2017). Searles Lake: Horita (1990).

Table 15. Results of stable isotopic study on primary fluid inclusion of Praid massive type salt rock. O and H isotopic composition of various evaporites are listed for comparison.

Publication	Age	Geologic settings	Sample	$\delta^{18}O$	$\delta^{2}H$
This study	Middle-Miocene (Badenian)	Badenian halite fluid inclusions Transylvanian Basin	water of fluid inclusion	-7.89 - 17.8	-91.5 - -74.2
(Hałas and Krouse, 1982)	Middle-Miocene (Badenian)	Carpathian Foredeep	gypsum hydration water	-14.9 - - 3.7	- 95 - -19
(Kasprzyk and Jasińska, 1998)	Middle-Miocene (Badenian)	Carpathian Foredeep	gypsum hydration water	-11.2 - - 3.2	-76.4 - -21.6
(Rigaudier et al., 2011)	Late-Miocene (Messinian)	Realmonte Mine	water of fluid inclusion	-2.5 - +14.6	- 39 - +31
(Knauth and Beeunas, 1986)	Permian	Palo Duro Basin (Texas)	water of fluid inclusion	-6.8 - 2.2	-55 - -5
(Evans et al., 2015b)	Late-Miocene (Messinian)	Sorbas Basin, Yesares member	gypsum hydration water	-5.8 - 2.36	-40.18 - +3.44
(Li et al., 2017)	Permian	NE Tibetian Plateau Qaidam Basin	gypsum hydration water	-8.18 - 13.73	-53.85 - 71.16
(Wilson and Long, 1993)	Devonian	Michigan Brines	brine sample	-7.06 - 3.6	-61.2 - -10.7
(Kloppmann et al., 2001)	Permian	Gorleben salt dome Germany	solid salt and brine	-10.2 - - 8.7	-73.1 - -60

To summary the results of the isotopic study on Praid salt rock, halite precipitated with negative $\delta^{18}O$ values, which could be cause by the escalating anhydrite precipitation (contemporaneously with halite) since anhydrite strongly prefers the heavier oxygen isotope. Depending on the degree of isolation of a basin, the seawater of the basin can evolve towards nonmarine composition (Bąbel and Schreiber, 2014), since inflowing freshwater (including land and subsurface water) which can even dominate the system. The results of this study suggest that both dolomite (Fig. 11/C) and the fluid inclusions in halite (Fig. 12/C,D) are influenced by organic material which could lower their delta values.

5.5. Addition to the Badenian Salinity Crisis

The thesis work was carried out in one particular part of the large, basinwide Middle Miocene evaporite body of the Transylvanian Basin, therefore it cannot be drawn large-scale, more regional conclusions. However, there are many connections between this geochemical, microstructural study and the wide Badenian geologic literature. Unfortunately, the micropetrographic investigations are missing from most published studies, the only one similarly detailed work belongs to Kátai (2017) also on the Praid salt rock. Microthermometry provides a much wider opportunity to compare data. As a conclusion, the a FIs in the other BSC deposits (Fig. 20) show the same range of homogenization temperatures (10-35 °C) (Galamay et al., 2004; Pintea, 2008; Kátai, 2017) as that resulted in this study. In the context of anhydrite formation temperature (~ 18 °C in NaCl saturated water) (Jowett et al., 1993), it is possible that the lower T_h values are closer to reality.

Isotopic data are also available for gypsum (both sulfate and hydration water) (Claypool et al., 1980; Hałas and Krouse, 1982; Kasprzyk, 1997; Cendón et al., 2004). Despite the difference in evaporite rock types (gypsum in the Carpathian Foredeep, halite with subordinate amount of anhydrite and dolomite in the TB), the isotopic characteristic of sulfates is in a good agreement with each other. The carbonates from the Carpathian Foredeep (Kudryntsi section) have negative $\delta^{13}C$ and $\delta^{18}O$ (Peryt and Peryt, 2009) similar to the dolomites in the Praid body. A farther located deposit situated in the Vienna Basin has BSC carbonates that fall in the $\delta^{13}C$ = +3 - -2.3 ‰ and $\delta^{18}O$ = +0,1 - -5,1 ‰ ranges, which is slightly shifted towards positive values (compared to Praid carbonates) revealing different water input and evolution. The question is still open, whether the meteoric water or organic compounds in water played a significant role in decreasing the carbon and oxygen delta values (Fig. 30). Water stable isotope data of Messinian evaporites (Rigaudier et al., 2011; Gázquez et al., 2017; Grothe et al., 2020) show negative $\delta^{18}O$ and $\delta^{2}H$ values, which is an unexpected result to our knowledge about isotopic composition of evaporites. The unequivocal negative values could be eventually, considered as a specific isotopic character of the Central-Paratethys, but further investigation is needed in this topic.

The development of BSC in icehouse conditions after the Miocene Climate Optimum (de Leeuw et al., 2018) is controversial to the basinwide evaporite formation, which requires greenhouse climate (Warren, 2016). Therefore, the BSC evaporites are most likely formed as a combination of tectonic and climatic processes that are not presented in the world today.

The total spatial extension of BSC evaporite rocks is matter of debate. Báldi et al. (2017) suggest that the Pannonian Basin was also affected by evaporation processes and related salt formation. Even the Vienna Basin has indications of evaporitic environment in Badenian times (Harzhauser et al., 2018). In the Middle Miocene, a major tectonic event (Adria-derived plate motions) caused a complete reorganization of the paleogeography in the Central Paratethys realm (Potter and Szatmari, 2009; De Leeuw et al., 2013). However, model construction is difficult because there is no functionating isolated marine basin today which is able to produce large amount of marine evaporites (Bąbel and Schreiber, 2014).

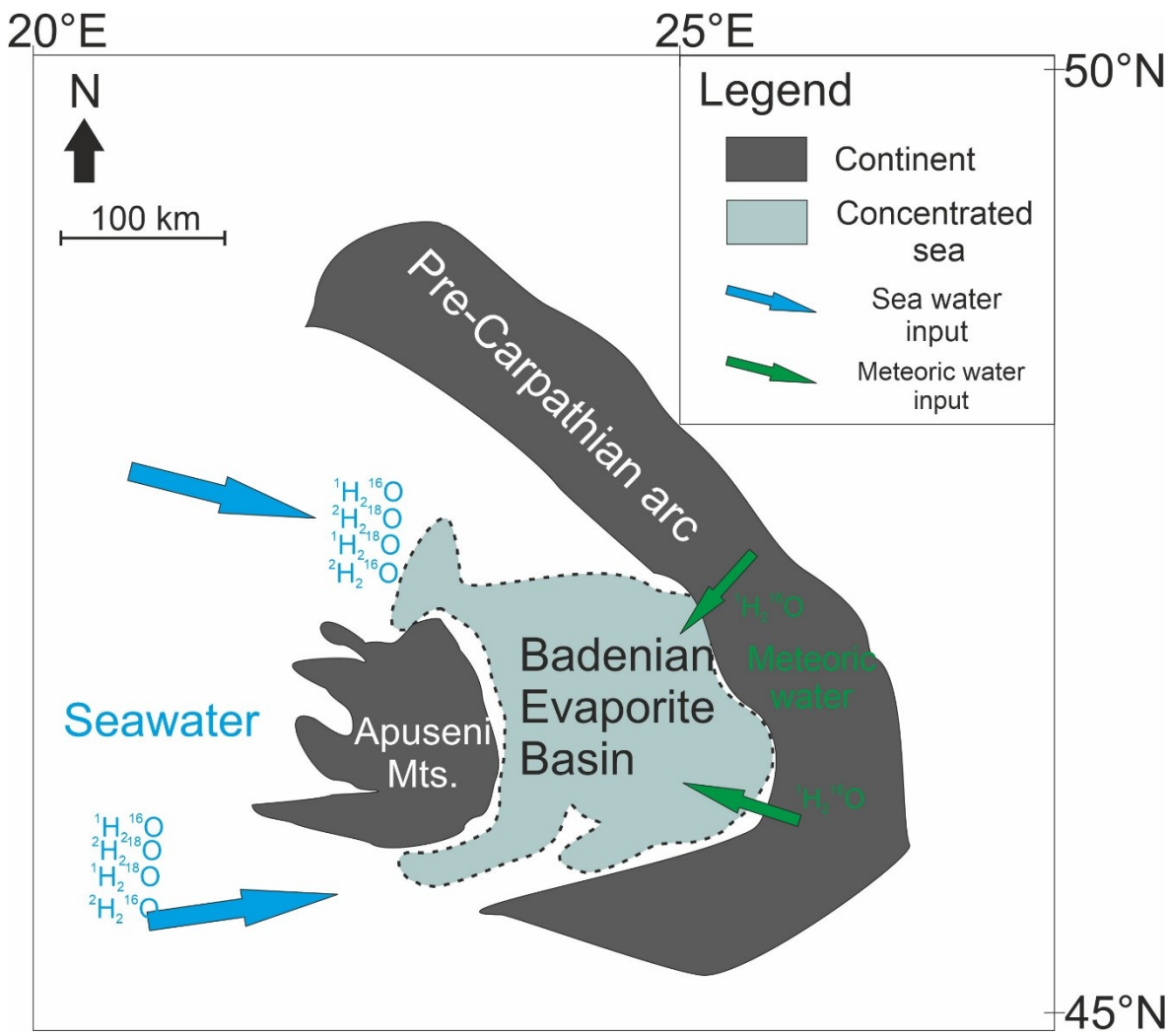

Figure 30. Schematic map of water input and isotopic mixing in the Middle Miocene Transylvanian Basin. The water loss was compensated by western part (Pannonian Basin) seawater inflow and by the meteoric waters at the eastern part, falling and descending from the uprising Carpathian arc.

6. Conclusions

The salt rocks from Praid show a complex petrology and geochemistry thanks to the special formation environment (restricted basin of the Central Paratethys) and the post salt deformation events.

At least two types of salt rocks can be distinguished. The massive type contains primary features (chevron-type halite crystals), which reveal shallow water crystallization. The relatively high abundance of detrital minerals and large (couple of mm) size rock fragments support the shallow, neritic deposition environment. The texture of massive salt is characterized as protomylonitic texture where large porphyroclasts are surrounded by submicron size halite grains.

The layered salt was deposited closer to the basin center, in a higher water depth, where the cyclic alteration of clay rich and clay-poor layers, related to the changes of the detrital input, are visible. The texture of the salt is similar to polygonal mosaic structure, which suggests intense halokinetic movements.

Based on the grain and subgrain size analyses, the differential stress and strain rate correspond to a transition of the salt stem from diapiric to extrusional state. Solution-precipitation creep and dislocation creep deformation mechanisms were and are still operating in the salt body, caused/causing subgrain formation and recrystallization in the Badenian evaporite. The relatively fast strain rates revealed significant deformation of the Praid salt even on human live scale.

Isotopic characteristics of sulfates obtained from anhydrite proved its seawater origin.

Primary fluid inclusions in halite (Fig. 12) are considered to be droplets of paleo seawater. Although, their seawater origin is proved (by Raman spectroscopy and microthermometry), the isotopic composition questions this assumption. Regarding the isotopic characteristics of the examined authigenic evaporite minerals (Table 5,6,7) (dolomite, anhydrite, halite FI), it is possible that besides evaporation of seawater, other processes interplayed, such as crystallization of O-and H-containing minerals, bioactivity and meteoric water input.

The evaporites of the Badenian Salinity Crisis from Praid show similarities to their Carpathian Foredeeps pairs in their S-O-C-H isotopic characteristics.

7. Summary

Detailed petrographic and geochemical study was carried out on the Middle Miocene (Badenian) evaporite from Praid (Transylvanian Basin). The salt rock formed during the so-called Badenian Salinity Crisis is tectonically reworked, however some primary features are preserved. Two types of salt rocks can be distinguished based on macroscopic and microscopic observations. Massive type has a protomylonitic texture with a large amount of detrital compounds, having cm-size elongated chevron halites, which have primary fluid inclusion rich cores. The primary fluid inclusions and presence of cm size detrital rock fragments indicate a shallow crystallization depth. Layered type salt rock has a more consistent grain size distribution as well as smaller average grain size and seldom presence of primary fluid inclusion. The fabric is similar to polygonal mosaic structure. This salt rock type evolved most likely in a larger distance from the seashore.

According to the fluid inclusion petrography, several types of FIs can be distinguished. First group is the primary fluid inclusions which can be found mostly in the massive salt type. The primary FIs offer insight into paleo seawater composition and crystallization temperature of the halite, in other words the formation environment of the evaporite deposit. Cryogenic Raman spectroscopy and microthermometry measurements proved that the salt formed from seawater. The above-mentioned results support that the primary fluid inclusions represent paleo seawater and are not related to diagenetic or hydrothermal processes; thus, the following stable isotopic measurements could be relevant in paleo environment reconstruction.

Secondary fluid inclusions are relevant in post salt evolution because they are the witnesses of the fluid transport events and deformational processes. S-type FIs occur in large variety of shape, phase and composition. Gas-bearing fluid inclusions composed of N_2 and/or CH_4 and/or CO_2 may be related to decomposed organic matter. The solely N_2 rich fluid inclusions probably represent another source such as paleo atmosphere, but more investigation is needed to clarify their origin. Liquid phase fluid inclusions appeared on grain boundaries are the main internal driving force of salt recrystallization processes.

The identification of the various microstructures could help to understand the operating deformation mechanisms in salt rock, which have been and are active during salt diapir emplacement at Praid. Microfabric data obtained from gamma irradiated samples and EBSD measurements are in line with the assumption that halite strain was accommodated by different deformation mechanisms, such as dislocation creep and solution– precipitation creep. The strain

rate (total strain rate between $2.5*10^{-12}$ and $1.9*10^{-11}$) calculations are in agreement with the recently observed motion of Praid salt stem in the salt mine. Hence the microstructural studies could be helpful also for mining maintenance. The calculated strain rates are quite high suggesting recently active halokinesis.

The Badenian Salinity crisis evolved after the change from greenhouse to icehouse climate which contradicts to a main criterion of basinwide salt formation, however the complexity (topographic segmentation, seawater level changes) of the Central-Paratethys realm could lead to evaporite formation. The conducted (and planned) stable isotopic studies draw attention the importance of organic matter and the complexity of the water supply system in the Transylvanian Basin. The results of the MSc thesis might be useful and comparable with paleontologic and stratigraphic knowledge in order to better understand the formation and evolution of this peculiar sediment and geological resource of the Transylvanian Basin.

In all of raw material explorations the knowledge relating to the genesis of the given material is one of the most important conditions to attain successful results. Hopefully, the contribution of my thesis to the understanding the evolution of the Transylvanian salt is bigger than a fluid inclusion or a subgrain.

8. Abstract (in Hungarian)

A diplomamunka mikroszerkezeti és geokémiai vizsgáltokatat foglal magába amelyeknek a regionális jelentőségű Bádeni Sókrízis kősó képződményén a tárgya. A minták az Erdélyi-medencéből, a parajdi sóbányából származnak. A klasszikus petrográfiai módszerek mellett mikrotermometria, Raman spektroszkópia, valamint visszaszórt elektrondiffrakciós, gamma besugárzásos technikákat alkalmaztam a sókőzet szerkezeti vizsgálataihoz. A geokémiai vizsgálatok (mikrotermometria, Raman spektroszkópia, stabil izotóp geokémia) fő célpontja a kősóban található elsődleges fluidumzárványok, amelyek az ős tengervizet zárják magukba, amelyből a kősó kristályosodott.

A kősó változatos textúrájára kétféle magyarázat adható. Az egyik lehetőség szerint a kősó különböző mélységben egyidejűleg képződött ami különböző primer szövetet eredményezett. Az elsődleges fluidumzárványban gazdag szürke tömeges kőzetszövet sekély, partközeli környezetre, a kevés elsődleges fluidumzárványt tartalmazó, réteges szövet, parttól távoli, mélyebb, vízrétegben képződött kősóra utalhat. A sókőzet autigén és detritális járulékos ásványi elegyrészeit azonosítottam petrográfiai vizsgálatokkal amelyek közül az autigén szulfátokkal (anhidrit) és karbonátottal (dolomit) stabilizotóp geokémiai vizsgálatokat is végeztem. E két ásvány jelenléte szulfát- és karbonáttelített oldatok jelenlétére utal. A helyben képződött ásványokon túl azonosítottam detritális alkotókat is: kvarc, csillám, agyagásványok, szemcseaggregátumok. A fluidumzárvány petrográfia segítségével elkülönítettem elsődleges (P-típusú) és másodlagos (S-típusú) fluidumzárványokat és elvégeztem az elsődlegesek részletes petrográfiai leírását. A P-típusú fluidumzráványok vizsgálatának jelentősége, hogy mikrotermometria mérésekkel meghatároztam a minimum képződési hőmérsékletét a befogadó kősónak. A mikrotermometriai módszer igazolta a kősó tengeri eredetét, ezenfelül a diplomamunka bővítette a BSC kőzeteiben a mikrotermometriai eredményeket ezáltal hozzájárult egy adatbázis kialakulásához.

A mikroszerkezet vizsgálatok kétféle deformációs mechanizmus aktivitását igazolták: az oldódás és kicsapódás vezérelte szemcsehatár kúszás (solution-preicipitation creep) és a diszlokációs kúszás (dislocation creep) vezérli a só szerkezetének mikroléptékű változásait. A visszaszórt elektron diffrakció és a gamma besugárzás segítségével azonosíthatóvá vált a sókőzet mikroszerkezete, így az alszemcsehálózat is, amelyből differenciált feszültség és alakváltozási ráta lett számolva. A recens állapotokat tükröző kőzetszövet az olódás és kicsapódás vezérelte

szemcsehatár kúszás a domináns folyamat, amely aránylag gyors deformációhoz, azaz néhány száz év alatt 10 %-os alakváltozáshoz vezet.

A stabilizotópos elemzések elsőként valósultak meg erdélyi sókőzeteken. Az anhidrit tengeri eredetű és izotópos arányai összhangban vannak a bádeni sókrízis más területről származó szulfát ásványainak eredményeivel. A dolomit petrográfiai és geokémiai vizsgálatai megerősítik, hogy térben és/vagy időben eltért a dolomitképződés a kősó és anhidrit keletkezéséről. Izotópos összetétele szerves eredetű szén forrásra utal, ami alapján feltételezhető, hogy képződésében szerepet játszott a szervesanyag bomlása és redox viszonyok változása is. A fluidumzárványok O és H izotópjai eltérő trendet jelölnek ki a korábbi irodalmaktól, ami nem meglepő eredmény egy eddig még nem vizsgált medencéből. Azonban az eredmények nagyobb ívű értékeléséhez további tanulmányok szükségesek.

A bádeni sókrízis az üvegház-jégkorszak váltást követően alakult ki. Ez önmagában ellentmond a „salt giant" képződés egyik alapkritériumának, azonban a lokálisan ható tényezőkkel magyarázható a kősó képződés. A megvalósult és folyamatban lévő stabilizotópos mérések sejtetik a szervesanyag bomlásának kiemelt szerepét és a redox viszonyok egész Paratethys-szintű változását. A vizsgálati eredmények hozzájárulnak válnak a paleontológiai, rétegtani ismeretanyaggal a 14 millió év őskörnyezeti és geodinamikai bélyegeit magán viselő kőzetösszlet jobb megértése érdekébe.

9. Acknowledgement

I am very glad to be a protagonist in such a fantastic research. This work would have never been carried out without the help and contribution of the followings as given here:

Dr. Csaba Szabó is sincerely thanked for giving me the opportunity to work on Transylvanian salt rock. I am really thankful for all his support in wide sense.

I am thankful to my co-supervisor, **Dr. György Falus**, for his contribution, especially in the microstructural studies. His personal interest and open-minded attitude for the material and the new methods and techniques has significantly increased my enthusiasm and the meaning of this work. I benefited a lot with my consultant **Dr. Márta Berkesi**'s advices in fluid inclusion petrography and in evaluation of Raman data.

Thanks to the instrument operators, **Dr. László Aradi** for Raman spectroscopic and to **Ábel Szabó** for electron microscopic work, furthermore to **Dr. Tünde Tóth** for carrying out the gamma irradiation. Thanks for **Dr. Palcsu László** who introduced me into the isotopic measurements as an excellent organizer. I am thankful to the staff at ATOMKI for hospitality during my outsourced work. I am thankful to the **geologist and miners of Praid Salt Mine** for their help.

I acknowledge the contribution of two outstanding computer scientist **Levente Kováts** and **Barnabás Bágyi** in softver and script developments.

For help in sample preparation special thanks are given **Levente Patkó**, **Ákos Kővágó, Márk Kozár**, **Judit Orsovszki**, **Ágoston Tóth** and **Jolien Linckens**.

I am very grateful to **Dr. Ágnes Gál** for hosting me in Kolozsvár and treating me as her family member. I am also very grateful to **Dr. Sándor Szakács** for his fantastic geologic interpretations during field work and his useful comments to the thesis. I would like to thank to **György Komlóssy** for his patient during thesis writing. He was always generous in sharing his enormous knowledge. Thanks to **Dr. Zoltán Unger** and the Oil & Gas Development for supporting me in my research.

Thanks for **Ferenc Wanek** and **Tibor Németh** for their advices and guidance, because they are not only outstanding geologist with tremendous knowledge but honest person also. I am glad to have exciting discussions with **Thomas Lange and Zsófia Pálos**. Special thanks to **Blanka**, **Eszter**, **Nikolett** and **Balázs** for their all-round support.

Credit goes to my Family, who have been very patient and helpful during my MSc carreer.

This work was supported European Union and the State of Hungary, co-financed by the European Regional Development Fund in the project of GINOP-2.3.2-15-2016-00009 'ICER' and by the ÚNKP-19-2 New National Excellence Program of the Ministry for Innovation and Technology.

10. Bibliography

Alexandre P. (2020) *Isotopes and the Natural Environment*., Springer Nature Switzerland.

Anderson R. Y. and Dean W. E. (1995) Filling the Delaware Basin: Hydrologic and climatic controls on the Upper Permian Castile Formation varved evaporite. In *The Permian of Northern Pangea* Springer. pp. 61–78.

Aquilano D., Otálora F., Pastero L. and García-Ruiz J. M. (2016) Three study cases of growth morphology in minerals: Halite, calcite and gypsum. *Prog. Cryst. Growth Charact. Mater.* **62**, 227–251. Available at: http://dx.doi.org/10.1016/j.pcrysgrow.2016.04.012.

Ayora C., Garcia-Veigas J. and Pueyo J. J. (1994) The chemical and hydrological evolution of an ancient potash-forming evaporite basin as constrained by mineral sequence, fluid inclusion composition, and numerical simulation. *Geochim. Cosmochim. Acta* **58**, 3379–3394.

Bąbel M. and Schreiber B. C. (2014) *Geochemistry of Evaporites and Evolution of Seawater*.,

Báldi K., Velledits F., Corić S., Lemberkovics V., Lorincz K. and Shevelev M. (2017) Discovery of the Badenian evaporites inside the Carpathian Arc: Implications for global climate change and Paratethys salinity. *Geol. Carpathica* **68**, 193–206.

Báldi T. (1980) A korai Paratethys története. *Földtani Közlöny* **110**, 456–472.

Balintoni I., Seghedi I. and Szakács A. (1997) Review of the Neogene post-collisional magmatism tectonics interplay in the intracarpathian region. *Stud. Univ. Babes-Bolyai, Ser. Geol. Cluj-Napoca* **42**, 33–49.

Baumgartner M. and Bakker R. J. (2009) CaCl2 -hydrate nucleation in synthetic fluid inclusions. *Chem. Geol.* **265**, 335–344. Available at: http://dx.doi.org/10.1016/j.chemgeo.2009.04.012.

Baumgartner M. and Bakker R. J. (2010) Raman spectra of ice and salt hydrates in synthetic fluid inclusions. *Chem. Geol.* **275**, 58–66. Available at: http://dx.doi.org/10.1016/j.chemgeo.2010.04.014.

Berner R. A. (1980) *Early diagenesis: a theoretical approach*., Princeton University Press.

Blamey N. J. F. and Brand U. (2019) Atmospheric gas in modern and ancient halite fluid inclusions : A screening protocol Gondwana Research Atmospheric gas in modern and ancient halite fl uid inclusions : A screening protocol. *Gondwana Res.* **69**, 163–176. Available at: https://doi.org/10.1016/j.gr.2018.12.004.

Brocks J. J., Love G. D., Summons R. E., Knoll A. H., Logan G. A. and Bowden S. A. (2005) Biomarker evidence for green and purple sulphur bacteria in a stratified Palaeoproterozoic

sea. *Nature* **437**, 866–870.

Carter N. L., Horseman S. T., Russell J. E. and Handin J. (1993) Rheology of rocksalt. *J. Struct. Geol.* **15**, 1257–1271.

Cendón D. I., Ayora C., Pueyo J. J., Taberner C. and Blanc-valleron M. (2008) The chemical and hydrological evolution of the Mulhouse potash basin (France): Are " marine " ancient evaporites always representative of synchronous seawater chemistry ? ☆. **252**, 109–124.

Cendón D. I., Peryt T. M., Ayora C., Pueyo J. J. and Taberner C. (2004) The importance of recycling processes in the Middle Miocene Badenian evaporite basin (Carpathian foredeep): Palaeoenvironmental implications. *Palaeogeogr. Palaeoclimatol. Palaeoecol.* **212**, 141–158.

Ciupagea D., Pauca M. and Ichim T. (1970) Geology of the Transylvanian depression. *Ed. Acad. Republici Social. Rom. Bucharest*.

Claypool G. E., Holser W. T., Kaplan I. R., Sakai H. and Zak I. (1980) The age curves of sulfur and oxygen isotopes in marine sulfate and their mutual interpretation. *Chem. Geol.* **28**, 199–260.

Cody R. D. and Cody A. M. (1988) Gypsum Nucleation and Crystal Morphology in Analog Saline Terrestrial Environments. *J. Sediment. Petrol.* **58**, 247–255.

Craig H. (1961) Isotopic variations in meteoric waters. *Science (80-.).* **133**, 1702–1703.

Craig H. (1953) The geochemistry of the stable carbon isotopes. *Geochim. Cosmochim. Acta* **3**, 53–92.

Csontos L. and Nagymarosy A. (1998) The Mid-Hungarian line: A zone of repeated tectonic inversions. *Tectonophysics* **297**, 51–71.

Csontos L., Nagymarosy A., Horvath F., Kovac M. and Tari G. (1992) Tertiary Kinematics of the Intra-Carpathian Area.

Deák G., Deák S. E. and Mihai S. O. (2008) 3D stability computation of the praid salt mines complex using DKR control method. *12th Int. Conf. Comput. Methods Adv. Geomech. 2008* **1**, 8–15.

Desbois G., Závada P., Schléder Z. and Urai J. L. (2010) Deformation and recrystallization mechanisms in actively extruding salt fountain: Microstructural evidence for a switch in deformation mechanisms with increased availability of meteoric water and decreased grain size (Qum Kuh, central Iran). *J. Struct. Geol.* **32**, 580–594.

Draskóczy I. (2014) A kősó bányászat átalakulása Erdélyben az Árpád-korban. In *Arcana tabularii: Tanulmányok Solymosi László tiszteletére I-II* (eds. A. Bárány, G. Dreska, and K. Szovák). ELTE BTK, Budapest. pp. 825–835.

Drury R. M. and Urai J. L. (1990) Deformation-related recrystallization processes. *Tectonophysics* **172**, 235–253.

Dubessy J., Audeoud D., Wilkins R. and Kosztolanyi C. (1982) The use of the Raman microprobe MOLE in the determination of the electrolytes dissolved in the aqueous phase of fluid inclusions. *Chem. Geol.* **37**, 137–150.

Dubessy J., Poty B. and Ramboz C. (1989) Advances in C-O-H-N-S fluid geochemistry based on micro-Raman spectrometric analysis of fluid inclusions. *Eur. J. Mineral.* **1**, 517–534.

Dumitrescu I., Săndulescu M., Bandrabur T. and Săndulescu J. (1970) *Harta geologică a României, Scara 1: 200.000*., Bucharest. Available at: http://geoportal.gov.ro/.

Evans N. P., Turchyn A. V., Gázquez F., Bontognali T. R. R., Chapman H. J. and Hodell D. A. (2015a) Coupled measurements of δ18O and δD of hydration water and salinity of fluid inclusions in gypsum from the Messinian Yesares Member, Sorbas Basin (SE Spain). *Earth Planet. Sci. Lett.* **430**, 499–510.

Evans N. P., Turchyn A. V., Gázquez F., Bontognali T. R. R., Chapman H. J. and Hodell D. A. (2015b) Coupled measurements of δ18O and δD of hydration water and salinity of fluid inclusions in gypsum from the Messinian Yesares Member, Sorbas Basin (SE Spain). *Earth Planet. Sci. Lett.* **430**, 499–510. Available at: http://dx.doi.org/10.1016/j.epsl.2015.07.071.

Filipescu S. and Gîrbacea R. (1997) Lower Badenian sea-level drop on the western border of the Transylvanian Basin: Foraminiferal paleobathymetry and stratigraphy. *Geol. Carpathica* **48**, 325–334.

Fodor L., Csontos L., Bada G., Györfi I. and Benkovics L. (1999) Tertiary tectonic evolution of the Pannonian Basin system and neighbouring orogens: a new synthesis of palaeostress data. *Geol. Soc. Spec. Publ.* **156**, 295–334.

Frezzotti M. L., Tecce F. and Casagli A. (2012) Raman spectroscopy for fluid inclusion analysis. *J. Geochemical Explor.* **112**, 1–20. Available at: http://dx.doi.org/10.1016/j.gexplo.2011.09.009.

Frezzotti M. L. and Touret J. L. R. (2014) CO2, carbonate-rich melts, and brines in the mantle. *Geosci. Front.* **5**, 697–710. Available at: http://dx.doi.org/10.1016/j.gsf.2014.03.014.

Galamay A. R., Bukowski K., Poberezhskyy A. V., Karoli S. and Kovalevych V. M. (2004) Origin of the Badenian salts from East Slovakian basin by the analysis of fluid inclusions. *Ann. Soc. Geol. Pol.* **74**, 267–276.

Gao G. (1990) Geochemical and isotopic constraints on the diagenetic history of a massive stratal, late Cambrian (Royer) dolomite, Lower Arbuckle Group, Slick Hills, SW Oklahoma, USA. *Geochim. Cosmochim. Acta* **54**, 1979–1989.

García-Veigas J., Cendón D. I., Gibert L., Lowenstein T. K. and Artiaga D. (2018) Geochemical indicators in Western Mediterranean Messinian evaporites: Implications for the salinity crisis. *Mar. Geol.* **403**, 197–214. Available at: https://doi.org/10.1016/j.margeo.2018.06.005.

Gázquez F., Calaforra J. M., Evans N. P. and Hodell D. A. (2017) Using stable isotopes (δ17O, δ18O and δD) of gypsum hydration water to ascertain the role of water condensation in the formation of subaerial gypsum speleothems. *Chem. Geol.* **452**, 34–46. Available at: http://dx.doi.org/10.1016/j.chemgeo.2017.01.021.

Gerdes G., Klenke T. and Noffke N. (2000) Microbial signatures in peritidal siliciclastic sediments: A catalogue. *Sedimentology* **47**, 279–308.

Ghergari L., Mészáros N., Hosu A., Filipescu S. and Chira C. (1991) The gypsiferous formation at Cheia (Cluj County). *Stud. Univ. Babes-Bolyai. Ser. Geol.* **36**, 13–28.

Gibson J. J., Edwards T. W. D., Bursey G. G. and Prowse T. D. (1993) Estimating Evaporation Using Stable Isotopes : Two catchments in Northern Canada. *Nord. Hydrol.* **24**, 79–94.

Goldstein H. R. and Reynolds T. J. (1994) Systematics of fluid inclusions in diagenetic minerals. *SEPM short course* **31**, 199.

Goldstein R. H. (2001) Fluid inclusions in sedimentary and diagenetic systems. *Lithos* **55**, 159–193.

Grothe A., Andreetto F., Reichart G. J., Wolthers M., Van Baak C. G. C., Vasiliev I., Stoica M., Sangiorgi F., Middelburg J. J., Davies G. R. and Krijgsman W. (2020) Paratethys pacing of the Messinian Salinity Crisis: Low salinity waters contributing to gypsum precipitation? *Earth Planet. Sci. Lett.* **532**, 116029. Available at: https://doi.org/10.1016/j.epsl.2019.116029.

Guillope M. and Poirier J. P. (1979) Dynamic recrystallization during creep of single-crystalline halite: an experimental study. *J. Geophys. Res.* **84**, 5557–5567.

Halas S. (1987) Oxygen and Sulphur Isotope Ratios of Sulphate Minerals in Native Sulphur Deposits. *Isot. Isot. Environ. Heal. Stud.* **23**, 282–283.

Hałas S. and Krouse H. R. (1982) Isotopic abundances of water of crystallization of gypsum from the Miocene evaporite formation, Carpathian Foredeep, Poland. *Geochim. Cosmochim. Acta* **46**, 293–296.

Hardie L. A. (1967) The Gypsum—anhydrite Equilibrium at One Atmosphere Pressure1. *Am. Mineral.* **52**, 171–200.

Hardie L. A., Lowenstein T. K. and Spencer R. J. (1985) The problem of distinguishing between primary and secondary features in evaporites. *Sixth Int. Symp. salt* **1**, 173–195.

Harzhauser M., Grunert P., Mandic O., Lukeneder P., Gallardo Á. G., Neubauer T. A., Carnevale G., Landau B. M., Sauer R. and Strauss P. (2018) Middle and late Badenian palaeoenvironments in the northern Vienna Basin and their potential link to the Badenian Salinity Crisis. *Geol. Carpathica* **69**, 149–168.

Hay W. W., Migdisov A., Balukhovsky A. N., Wold C. N., Flögel S. and Söding E. (2006) Evaporites and the salinity of the ocean during the Phanerozoic: Implications for climate, ocean circulation and life. *Palaeogeogr., Palaeoclim. Palaeoecol.* **240**, 3–46.

Hoefs J. (2009) *Stable Isotope Geochemistry*. 6th ed., Springer-Verlag Berlin Heidelberg, Göttingen.

Holser W. T. (1992) Stable isotope geochemistry of sulfate and chloride rocks. In *Isotopic Signatures and Sedimentary Records* Springer. pp. 153–176.

Horita J. (1990) Stable isotope paleoclimatology of brine inclusions in halite: Modeling and application to Searles Lake, California. *Geochim. Cosmochim. Acta* **54**, 2059–2073.

Horváth F. (1993) Towards a mechanical model for the formation of the Pannonian basin. *Tectonophysics* **226**, 333–357.

Horváth F., Bada G., Windhoffer G. ., Csontos L., Dombrádi E., Dövényi P., Fodor L., Grenerczy G., Síkhegyi F., Szafián P., Székely B., Timár G., Tóth L. and Tóth T. (2006) Atlas of the present-day geodynamics of the Pannonian basin: Euroconform maps with explanatory text. *Magy. Geofiz.* **47**, 133–137. Available at: https://hungary.pure.elsevier.com/hu/publications/atlas-of-the-present-day-geodynamics-of-the-pannonian-basin-euroc [Accessed May 18, 2020].

Horváth I. (2019) A parajdi sóbánya titkai. , 1. Available at:

http://www.salinapraid.ro/tortenelem-kitermeles [Accessed May 5, 2020].

Huismans R. S., Bertotti G., Ciulavu D., Sanders C. A. E., Cloetingh S. and Dinu C. (1997) Structural evolution of the Transylvanian Basin (Romania): A sedimentary basin in the bend zone of the Carpathians. *Tectonophysics* **272**, 249–268.

Jackson M. P. A. and Hudec M. R. (2017) *Salt tectonics: Principles and practice*., Cambridge University Press.

Jackson M. P. A. and Talbot C. J. (1986) External shapes, strain rates, and dynamics of salt structures. *Geol. Soc. Am. Bull.* **97**, 305–323.

Jowett C. E., Cathles L. . and Davis W. B. (1993) Jowett et al 1998.pdf. *Am. Assoc. Pet. Geol. Bull.*, 402–413.

Kasprzyk A. (1997) Oxygen and sulphur isotope composition of Badenian (Middle Miocene) gypsum deposits in southern Poland: A preliminary study. *Kwart. Geol.* **41**, 53–59.

Kasprzyk A. and Jasińska B. (1998) Isotopic composition of the crystallization water of gypsum in the Badenian of the northern Carpathian Foredeep: A case study from the cores Przyborow 1 and Strzegom 143. *Geol. Q.* **42**, 301–309.

Kátai O. (2017) Komplex szöveti és fluidumzárvány vizsgálat a parajdi sódómban (Erdélyi-medence). Eötvös University.

Kercsmár Z., Fodor L. and Pálfalvi S. (2006) Tectonic Control and Basin Evolution of the Northern Transdanubian Eocene Basins (Vértes Hills , Central Hungary). , 64–66.

Kerkhof A. M. and Hein U. F. (2001) Fluid inclusion petrography. *Lithos* **55**, 27–47.

Kloppmann W., Négrel P., Casanova J., Klinge H., Schelkes K. and Guerrot C. (2001) Halite dissolution derived brines in the vicinity of a permian salt dome (N German Basin). Evidence from boron, strontium, oxygen, and hydrogen isotopes. *Geochim. Cosmochim. Acta* **65**, 4087–4101.

Knauth L. P. and Beeunas M. A. (1986) Isotope geochemistry of fluid inclusions in Permian halite with implications for the isotopic history of ocean water and the origin of saline formation waters. *Geochim. Cosmochim. Acta* **50**, 419–433.

Kneuker T., Zulauf G., Mertineit M., Behlau J. and Hammer J. (2014) Deformationsverhalten von permischem Staßfurt-Steinsalz aus Morsleben (Deutschland) bei unterschiedlichem finitem strain: Abschätzungen aus mikrogefüge-studien und EBSD-analysen. *Zeitschrift der Dtsch. Gesellschaft fur Geowissenschaften* **165**, 91–106.

Koch P. L., Zachos, James C. and Gingerich P. . (1992) Correlation between isotope records in marine and continental reservoirs near the Paleocene/Eocene boundary. *Nature* **358**, 319–322.

Koehler G. D., Chipley D. and Kyser T. K. (1991) Measurement of the hydrogen and oxygen isotopic compositions of concentrated chloride brines and brines from fluid inclusions in halite. *Chem. Geol.* **94**, 45–54.

Kováčová P., Emmanuel L., Hudáčková N. and Renard M. (2009) Central paratethys paleoenvironment during the Badenian (Middle Miocene): Evidence from foraminifera and stable isotope (δ13C and δ18O) study in the Vienna Basin (Slovakia). *Int. J. Earth Sci.* **98**, 1109–1127.

Kovalevych V., Paul J. and Peryt T. M. (2009) Fluid inclusions in halite from the röt (Lower Triassic) salt deposit in central Germany: Evidence for seawater chemistry and conditions of salt deposition and recrystallization. *Carbonates and Evaporites* **24**, 45–57.

Krézsek C. and Bally A. W. (2006) The Transylvanian Basin (Romania) and its relation to the Carpathian fold and thrust belt: Insights in gravitational salt tectonics. *Mar. Pet. Geol.* **23**, 405–442.

Krézsek C. and Filipescu S. (2005) Middle to late Miocene sequence stratigraphy of the Transylvanian Basin (Romania). *Tectonophysics* **410**, 437–463.

Krézsek C., Filipescu S., Silye L., Maţenco L. and Doust H. (2010) Miocene facies associations and sedimentary evolution of the Southern Transylvanian Basin (Romania): Implications for hydrocarbon exploration. *Mar. Pet. Geol.* **27**, 191–214.

Lazar B. and Holland H. D. (1988) The analysis of fluid inclusions in halite. *Geochim. Cosmochim. Acta* **52**, 485–490.

Lecuyer C., Gillet P. and Robert F. (1998) The hydrogen isotope composition of seawater and the global water cycle. *Chem. Geol.* **145**, 249–261.

De Leeuw A., Bukowski K., Krijgsman W. and Kuiper K. F. (2010) Age of the Badenian salinity crisis; Impact of Miocene climate variability on the circum-mediterranean region. *Geology* **38**, 715–718.

De Leeuw A., Filipescu S., Maţenco L., Krijgsman W., Kuiper K. and Stoica M. (2013) Paleomagnetic and chronostratigraphic constraints on the middle to late miocene evolution of the transylvanian basin (Romania): Implications for central paratethys stratigraphy and

emplacement of the tisza-dacia plate. *Glob. Planet. Change* **103**, 82–98.

de Leeuw A., Tulbure M., Kuiper K. F., Melinte-Dobrinescu M. C., Stoica M. and Krijgsman W. (2018) New 40Ar/39Ar, magnetostratigraphic and biostratigraphic constraints on the termination of the Badenian Salinity Crisis: Indications for tectonic improvement of basin interconnectivity in Southern Europe. *Glob. Planet. Change* **169**, 1–15. Available at: https://doi.org/10.1016/j.gloplacha.2018.07.001.

Lenkey L., Dövényi P., Horváth F. and Cloetingh S. A. P. L. (2001) Geothermics of the Pannonian basin and its bearing on the neotectonics. *Stephan Mueller Spec. Publ. Ser.* **3**, 29–40.

Li J., Li M., Fang X., Zhang G., Zhang W. and Liu X. (2017) Isotopic composition of gypsum hydration water in deep Core SG-1, western Qaidam basin (NE Tibetan Plateau), implications for paleoclimatic evolution. *Glob. Planet. Change* **155**, 70–77. Available at: http://dx.doi.org/10.1016/j.gloplacha.2017.06.006.

Longinelli A. (1979) Isotope geochemistry of some Messinian evaporates: Paleoenvironmental implications. *Palaeogeogr. Palaeoclimatol. Palaeoecol.* **29**, 95–123.

Lowenstein T. K. and Hardie L. A. (1985) Criteria for the recognition of salt-pan evaporites. *Sedimentology* **32**, 627–644.

Lowenstein T. K., Schubert B. A. and Timofeeff M. N. (2011) Microbial communities in fluid inclusions and long-term survival in halite. *GSA Today* **21**, 4–9.

Magaritz M., Goldenberg L., Kafri U. and Arad A. (1980) Dolomite formation in the seawater-freshwater interface. *Nature* **287**, 622–624.

Magyar I., Geary D. H., Lantos M., Müller P. and Süto-Szentai M. (1999) Integrated biostratigraphic, magnetostratigraphic and chronostratigraphic correlations of the Late Miocene Lake Pannon deposits. *Acta Geol. Hungarica* **42**, 5–31.

Mandic O., Sant K., Kallanxhi M. E., Ćorić S., Theobalt D., Grunert P., de Leeuw A. and Krijgsman W. (2019) Integrated bio-magnetostratigraphy of the Badenian reference section Ugljevik in southern Pannonian Basin - implications for the Paratethys history (middle Miocene, Central Europe). *Glob. Planet. Change* **172**, 374–395. Available at: https://doi.org/10.1016/j.gloplacha.2018.10.010.

Mertineit M., Schramm M., Hammer J. and Zulauf G. (2014) Deformation of anhydrite rocks (Gorleben-Bank, z3OSM) in a high-strain domain of the Gorleben salt dome, Germany.

Zeitschrift der Dtsch. Gesellschaft für Geowissenschaften **165**, 49–62.

Naiman E. R., Bein A. and Robert F. (1983) Complex polyhedral crystals of limpid dolomite associated with halite, Permian Upper Clear Fork and Glorieta Formations, Texas. *J. Sediment. Petrol.* **53**, 549–555.

Ni P., Ding J. and Rao B. (2006) In situ cryogenic Raman spectroscopic studies on the synthetic fluid inclusions in the systems H2O and NaCl-H2O. *Chinese Sci. Bull.* **51**, 108–114.

Oren A. and Rodríguez-Valera F. (2001) The contribution of halophilic Bacteria to the red coloration of saltern crystallizer ponds. *FEMS Microbiol. Ecol.* **36**, 123–130.

Palcu D. V., Golovina L. A., Vernyhorova Y. V., Popov S. V. and Krijgsman W. (2017) Middle Miocene paleoenvironmental crises in Central Eurasia caused by changes in marine gateway configuration. *Glob. Planet. Change* **158**, 57–71.

Palotai M. and Csontos L. (2012) Flexural basin reworked by salt-related pull-apart structures: The Adony Basin. *Cent. Eur. Geol.* **55**, 147–180.

Paraschiv D. (1979) *Romanian oil and gas fields*., Institute of Geology and Geophysics, Bucharest.

Paraschiv D. (1997) The pre-Paratethys buried denudational surface in Romanian territory. *Rev. Roum. Géographie* **41**, 21–32.

Pécskay Z., Lexa J., Szakács A., Seghedi I., Balogh K., Konečný V., Zelenka T., Kovacs M., Póka T., Fülöp A., Márton E., Panaiotu C. and Cvetković V. (2006) Geochronology of Neogene magmatism in the Carpathian arc and intra-Carpathian area. *Geol. Carpathica* **57**, 511–530.

Pedrós-Alió C., Calderón-Paz J. I., MacLean M. H., Marrasé C. G. M., Gasol J. M. and Guixa-Boixereu N. (2000) The microbial food web along salinity gradients. *FEMS Microbiol. Ecol.* **32**, 143–155.

Pennock G. M., Drury M. R. and Spiers C. J. (2005) The development of subgrain misorientations with strain in dry synthetic NaCl measured using EBSD. *J. Struct. Geol.* **27**, 2159–2170.

Peryt D. and Peryt T. (2009) Environmental changes in the declining Middle Miocene Badenian evaporite basin of the Ukrainian Carpathian Foredeep (Kudryntsi section). *Geol. Carpathica* **60**, 505–517.

Peryt T. M. (2006) The beginning, development and termination of the Middle Miocene

Badenian salinity crisis in Central Paratethys. *Sediment. Geol.* **188–189**, 379–396.

Peryt T., Szaran J., Jasionowski M., Halas S., Peryt D., Poberezhskyy A. V., Karoli S. and Wojtowicz A. (2002) S and O isotope composition of the Badenian (Middle Miocene) sulphates in the Carpathian Foredeep. *Geol. Carpathica* **53**, 391–398.

Petrychenko O. Y., Marek T. and F E. I. C. (2005) Early Cambrian seawater chemistry from fluid inclusions in halite from Siberian evaporites. *Chem. Geol.* **219**, 149–161.

Pierre C. (1985) Isotopic evidence for the dynamic redox cycle of dissolved sulphur compounds between free and interstitial solutions in marine salt pans. *Chem. Geol.* **53**, 191–196.

Pintea I. (2008) Liquid inclusions microthermometry in the Badenian halite and actual evaporite salt crust from Romania. *Rom. J. Miner. Depos.* **83**, 115–118.

Popov S. V., Rögl F., Rozanov A. Y., Steininger F. F., Shcherba I. G. and Kovac M. (2004) *Lithological-Paleogographic maps of Paratethys*., E. Schweizerbart'sche Verlagbuchhandlung, Stuttgart.

Potter P. E. and Szatmari P. (2009) Global Miocene tectonics and the modern world. *Earth-Science Rev.* **96**, 279–295. Available at: http://dx.doi.org/10.1016/j.earscirev.2009.07.003.

Proust J. N. and Hosu A. (1996) Sequence stratigraphy and Paleogene tectonic evolution of the Transylvanian Basin (Romania, eastern Europe). *Sediment. Geol.* **105**, 117–140.

Reading H. G. and Collinson J. D. (1996) *Clastic coasts*.,

Rigaudier T., Lécuyer C., Gardien V., Suc J. P. and Martineau F. (2011) The record of temperature, wind velocity and air humidity in the δD and δ18O of water inclusions in synthetic and Messinian halites. *Geochim. Cosmochim. Acta* **75**, 4637–4652.

Roedder E (1984) *Fluid Inclusions*., Mineralogical Society of America. Available at: https://books.google.hu/books?id=tk4SAQAAIAAJ.

Roedder Edwin (1984) The fluids in salt. *Am. Mineral.* **69**, 413–439.

Rögl F. (1998) Palaeogeographic Considerations for Mediterranean and Paratethys Seaways (Oligocene to Miocene). *Ann. des Naturhistorischen Museums Wien* **99A**, 279–310.

Rollinson H. R. (1993) *Using geochemical data: evaluation, presentation, interpretation.*, Longman Group, New York.

Samson I. M. and Walker R. T. (2000) Cryogenic raman spectroscopic studies in the system NaCl-CaCl2-H2O and implications for low-temperature phase behavior in aqueous fluid inclusions. *Can. Mineral.* **38**, 35–43.

Sanders C., Huismans R., van Wees J. D. and Andriessen P. (2001) The Neogene history of the Transylvanian basin in relation to its surrounding mountains. *Stephan Mueller Spec. Publ. Ser.* **3**, 121–133. Available at: http://www.stephan-mueller-spec-publ-ser.net/3/121/2002/.

Sanz-Montero M. E., Rodríguez-Aranda J. P. and García Del Cura M. A. A. (2008) Dolomite-silica stromatolites in miocene lacustrine deposits from the duero basin, spain: The role of organotemplates in the precipitation of dolomite. *Sedimentology* **55**, 729–750.

Schléder Z., Burliga S. and Urai J. L. (2007) Dynamic and static recrystallization-related microstructures in halite samples from the Kłodawa salt wall (central Poland) as revealed by gamma-irradiation. *Neues Jahrb. fur Mineral. Abhandlungen* **184**, 17–28.

Schléder Z. and Urai J. L. (2007) Deformation and recrystallization mechanisms in mylonitic shear zones in naturally deformed extrusive Eocene-Oligocene rocksalt from Eyvanekey plateau and Garmsar hills (central Iran). *J. Struct. Geol.* **29**, 241–255.

Schléder Z. and Urai J. L. (2005) Microstructural evolution of deformation-modified primary halite from the Middle Triassic Röt Formation at Hengelo, The Netherlands. *Int. J. Earth Sci.* **94**, 941–955.

Schmid S. M., Bernoulli D., Fügenschuh B., Matenco L., Schefer S., Schuster R., Tischler M. and Ustaszewski K. (2008) The Alpine-Carpathian-Dinaridic orogenic system: Correlation and evolution of tectonic units. *Swiss J. Geosci.* **101**, 139–183.

Schoenherr J. (2008) The Evolution of Halite and Solid Bitumen in the Petroleum System of the South Oman Salt Basin . *Geol. Endog. Dynamik* **PhD**. Available at: http://darwin.bth.rwth-aachen.de/opus3/frontdoor.php?source_opus=2131&la=de.

Schoenherr J., Urai J. L., Kukla P. A., Littke R., Schléder Z., Larroque J. M., Newall M. J., Al-Abry N., Al-Siyabi H. A. and Rawahi Z. (2007) Limits to the sealing capacity of rock salt: A case study of the infra-Cambrian Ara Salt from the South Oman salt basin. *Am. Assoc. Pet. Geol. Bull.* **91**, 1541–1557.

Schuller V. (2004) Evolution and geodynamic significance of the Upper Cretaceous Gosau basin in the Apuseni Mountains (Romania). University of Tübingen.

Senseny P. E., Hansen F. D., Russell J. E., Carter N. L. and Handin J. W. (1992) Mechanical behaviour of rock salt: phenomenology and micromechanisms. In *International journal of rock mechanics and mining sciences & geomechanics abstracts* Elsevier. pp. 363–378.

Speranza G., Cosentino D., Tecce F. and Faccenna C. (2013) Paleoclimate reconstruction during

the Messinian evaporative drawdown of the Mediterranean Basin: Insights from microthermometry on halite fluid inclusions. *Geochemistry, Geophys. Geosystems* **14**, 5054–5077.

Sperner B., Ioane D. and Lillie R. J. (2004) Slab behaviour and its surface expression: New insights from gravity modelling in the SE-Carpathians. *Tectonophysics* **382**, 51–84.

Spiers C. J., Schutjens P. M. T. M., Brzesowsky R. H., Peach C. J., Liezenberg J. L. and Zwart H. J. (1990) Experimental determination of constitutive parameters governing creep of rocksalt by pressure solution. *Geol. Soc. Spec. Publ.* **54**, 215–227.

Szafián P., Tari G., Horváth F. and Cloetingh S. (1999) Crustal structure of the Alpine-Pannonian transition zone: A combined seismic and gravity study. *Int. J. Earth Sci.* **88**, 98–110.

Szakács A. and Krézsek C. (2006) Volcano-basement interaction in the Eastern Carpathians: Explaining unusual tectonic features in the Eastern Transylvanian Basin, Romania. *J. Volcanol. Geotherm. Res.* **158**, 6–20.

Szakács A., Pécskay Z., Silye L., Balogh K., Vlad D. and Fülöp A. (2012) On the age of the Dej Tuff, Transylvanian Basin (Romania). *Geol. Carpathica* **63**, 139–148.

Szakács A. and Seghedi I. (1995) The Calimani-Gurghiu-Harghita volcanic chain, East Carpathians, Romania: Volcanological features. *Acta Vulcanol.* **7**, 145–153.

Sztanó O., Krézsek C., Magyar I., Wanek F. and Juhász G. (2005) Sedimentary cycles and rhythms in a Sarmatian to Pannonian (Late Miocene) transitional section at Oarba de Mures/Marosorbó, Transylvanian Basin. *Acta Geol. Hungarica* **48**, 235–257.

Tarkowski R. (2017) Perspectives of using the geological subsurface for hydrogen storage in Poland. *Int. J. Hydrogen Energy* **42**, 347–355. Available at: http://dx.doi.org/10.1016/j.ijhydene.2016.10.136.

Teller J. T. (1987) The pink colour of lakes , with an example from Australia. *J. Arid Environ.* **12**, 101–103. Available at: http://dx.doi.org/10.1016/S0140-1963(18)31179-0.

Thiemeyer N., Zulauf G., Mertineit M., Linckens J., Pusch M. and Hammer J. (2016) Microfabrics and 3D grain shape of Gorleben rock salt: Constraints on deformation mechanisms and paleodifferential stress. *Tectonophysics* **676**, 1–19. Available at: http://dx.doi.org/10.1016/j.tecto.2016.02.046.

Tiliță M., Lenkey L., Maţenco L., Horváth F., Surányi G. and Cloetingh S. (2018) Heat flow

modelling in the Transylvanian basin: Implications for the evolution of the intra-Carpathians area. *Glob. Planet. Change* **171**, 148–166.

Tilita M., Scheck-Wenderoth M., Matenco L. and Cloetingh S. (2015) Modelling the coupling between salt kinematics and subsidence evolution: Inferences for the Miocene evolution of the Transylvanian Basin. *Tectonophysics* **658**, 169–185. Available at: http://dx.doi.org/10.1016/j.tecto.2015.07.021.

Trouw R. A. J. and Passchier C. W. (2005) *Microtectonics*. 2nd ed., Springer-Verlag Berlin Heidelberg.

Túri M., Palcsu L., Papp L., Futó I., Molnár M., Rinyu L., Janovics R., Braun M., Hubay K., Kis M. and Koltai G. (2016) Isotope Characteristics of the water and sediment in volcanic Lake Saint Ana, East-Carpathians, Romania. *Carpathian J. Earth Environ. Sci.* **11**, 475–484.

Unger Z. and Leclair D. (2018) Salt and Methane Generation Initiated by Membrane Polarisation. *Earth Sci.* **7**, 53–57.

Urai J. L., Schléder Z., Spiers C. J. and Kukla P. A. (2008) Flow and transport properties of salt rocks. *Dyn. complex Intracont. basins Cent. Eur. basin Syst.*, 277–290.

Urai J. L., Spiers C. J., Zwart H. J. and Lister G. S. (1986) Weakening of rock salt by water during long-term creep. *Nature* **324**, 554–557.

Uriarte L. M., Dubessy J., Boulet P., Baonza V. G., Bihannic I. and Robert P. (2015) Reference Raman spectra of synthesized CaCl2·nH2O solids (n=0, 2, 4, 6). *J. Raman Spectrosc.* **46**, 822–828.

Vergnaud-Grazzini C. (1983) Reconstruction of Mediterranean Late Cenozoic hydrography by means of carbon isotope analyses. *Utr. Micropaleontol. Bull.* **30**, 25–49.

Vítek P., Jehlička J., Edwards H. G. M. and Osterrothová K. (2009) Identification of β-carotene in an evaporitic matrix-evaluation of Raman spectroscopic analysis for astrobiological research on Mars. *Anal. Bioanal. Chem.* **393**, 1967–1975.

Warren J. (2000) Dolomite: occurrence, evolution and economically important associations. *Earth-Science Rev.* **52**, 1–81.

Warren J. K. (2006a) Ancient basins and stratigraphic evolution. *Evaporites - Sediments, Resour. Hydrocarb.* **17**, 287–374.

Warren J. K. (2016) *Evaporites - A Geological Compedium*. 2nd ed., Springer International Publishing.

Warren J. K. (2010) Evaporites through time: Tectonic, climatic and eustatic controls in marine and nonmarine deposits. *Earth-Science Rev.* **98**, 217–268. Available at: http://dx.doi.org/10.1016/j.earscirev.2009.11.004.

Warren J. K. (2013) *Geochemistry of Evaporite Ores in an Earth-Scale Climatic and Tectonic Framework*. 2nd ed., Elsevier Ltd. Available at: http://dx.doi.org/10.1016/B978-0-08-095975-7.01125-6.

Warren J. K. (2006b) Interpreting evaporite texture. *Evaporites - Sediments, Resour. Hydrocarb.* **17**, 2–58.

Wawersik W. R. and Zeuch D. H. (1986) Modeling and mechanistic interpretation of creep of rock salt below 200°C. *Tectonophysics* **121**, 125–152. Available at: http://www.sciencedirect.com/science/article/pii/0040195186900405.

Willingshofer E., Neubauer F. and Cloetingh S. (1999) The significance of Gosau-type basins for the Late Cretaceous tectonic history of the Alpine-Carpathian belt. *Phys. Chem. Earth, Part A Solid Earth Geod.* **24**, 687–695.

Wilson T. P. and Long D. T. (1993) Geochemistry and isotope chemistry of CaNaCl brines in Silurian strata, Michigan Basin, U.S.A. *Appl. Geochemistry* **8**, 507–524.

Wright D. T. and Wacey D. (2005) Precipitation of dolomite using sulphate-reducing bacteria from the Coorong Region, South Australia: Significance and implications. *Sedimentology* **52**, 987–1008.

Zimmermann J. L. and Moretto R. (1996) Release of water and gases from halite crystals. *Eur. J. Mineral.* **8**, 413–422.

Zulauf G., Zulauf J., Bornemann O., Brenker F. E., Höfer H. E., Peinl M. and Woodland A. B. (2010) Experimental deformation of a single-layer anhydrite in halite matrix under bulk constriction. Part 2: Deformation mechanisms and the role of fluids. *J. Struct. Geol.* **32**, 264–277.